THE DEVELOPMENT OF A CT-BASED FRAMEWORK FOR RADIATION DOSIMETRY IN YTTRIUM-90 RADIOEMBOLIZATION

by

E. Courtney Henry III

Submitted in partial fulfilment of the requirements
for the degree of Doctor of Philosophy

at

Dalhousie University
Halifax, Nova Scotia
November 2021

Table of Contents

List of Tables

List of Figures

Abstract

Transarterial radioembolization (TARE) is a radiation-based embolic therapy for the treatment of liver cancer. In TARE, yttrium-90 (^{90}Y)-infused microspheres are administered via the hepatic arterial vasculature to facilitate the delivery of radiation to a target volume. Positron emission tomography (PET) imaging can provide estimates of the absorbed radiation dose following ^{90}Y TARE. However, these estimates are often associated with substantial uncertainty due in part to the inadequate spatial resolution of PET imaging. Computed tomography (CT) has the potential to provide superior spatial resolution imaging of microsphere distributions, which could improve absorbed dose estimates and refine our understanding of the dose-response relationship. This thesis presents the development, implementation, and validation of a CT-based framework for post-treatment dosimetry in ^{90}Y TARE.

Three manuscripts form the foundation of this thesis. The first manuscript, titled "*Quantification of the Inherent Radiopacity of Glass Microspheres for Precision Dosimetry in Yttrium-90 Radioembolization*," describes the development and analysis of a calibration phantom to relate radiopaque microsphere concentration to CT voxel intensity. Based on the findings of this first study, the construction and optimization of a clinical calibration phantom was ongoing throughout the remainder of the project. Preliminary results suggest the clinical phantom is well-suited to the needs of CT-based dosimetry in ^{90}Y TARE. The second manuscript, titled "*Post-Administration Dosimetry in Yttrium-90 Radioembolization through Micro-CT Imaging of Radiopaque Microspheres in a Porcine Renal Model*," analyzes micro-CT image data of radiopaque microsphere distributions to demonstrate the increased confidence provided by CT-based dosimetry in characterizing the absorbed dose heterogeneity in ^{90}Y TARE. The third manuscript, titled "*Precision Dosimetry in Yttrium-90 Radioembolization through CT Imaging of Radiopaque Microspheres in a Rabbit Liver Model*," validates CT-based dosimetry in ^{90}Y TARE through a comparison to conventional PET-based dosimetry, while also revealing benefits of improved dose distribution visualization, reduced partial volume effects, and the mitigation of respiratory motion effects.

Together, these works demonstrate that post-treatment CT imaging of *in vivo* radiopaque microsphere distributions provides the means to perform accurate and precise dosimetry in ^{90}Y TARE. This novel approach to radiation dosimetry will permit individualized treatment planning that should translate into improved patient outcomes.

List of Abbreviations Used

^{18}F	Flourine-18
^{176}Lu	Lutetium-176
^{89}Y	Yttrium-89
^{90}Y	Yttrium-90
^{90}Zr	Zirconium-90
^{99m}Tc-MAA	Technetium-99m-Labelled Macro-Aggregated Albumin
AAPM	American Association of Physicists in Medicine
BCLC	Barcelona Clinic for Liver Cancer
BGO	Bismuth Germanate
BSA	Body-Surface Area
CBCT	Cone Beam Computed Tomography
CE	*Conformité Européene*, European Conformity
CI	Confidence Intervals
CRC	Contrast Recovery Coefficient
COV	Coefficient of Variation
CT	Computed Tomography
CTCAE	Common Terminology Criteria for Adverse Events
DDR	Digitally Reconstructed Radiograph
DEB-TACE	Drug-Eluting Bead Transarterial Chemoembolization
DPK	Dose-Point Kernel
DSA	Digital Subtraction Angiography
cDVH	Cumulative Dose-Volume Histogram
DVK	Dose-Voxel Kernel
EASL	European Association for the Study of Liver
EBRT	External Beam Radiotherapy
EM	Expectation Maximization
FBP	Filtered Backprojection

FDA	Food and Drug Administration
FOV	Field of View
FWHM	Full Width at Half-Maximum
HCC	Hepatocellular Carcinoma
LOB	Limit of Blank
LOD	Limit of Detection
LOR	Line of Response
LSO[Ce]	Cerium-Doped Lutetium Oxyorthosilicate
LYSO	Lutetium-Yttrium Oxyorthosilicate
MC	Monte Carlo
MIRD	Medical Internal Radiation Dose
ML	Maximum Likelihood
MRI	Magnetic Resonance Imaging
NaI[Tl]	Thallium-Doped Sodium Iodide
NTCP	Normal Tissue Complication Probability
OS	Ordered Subsets
PET	Positron Emission Tomography
PMT	Photo Multiplier Tube
PSF	Point Spread Function
REBOC	Radioembolization Brachytherapy Oncology Consortium
RECIST	Response Evaluation Criteria in Solid Tumours
RILD	Radiation-Induced Liver Disease
SBRT	Stereotactic Body Radiation Therapy
SIRT	Selective Internal Radiation Therapy
SNR	Signal-to-Noise Ratio
SPECT	Single Photon Emission Computed Tomography
SSP	Slice Sensitivity Profile
TARE	Transarterial Radioembolization
cTACE	Conventional Transarterial Chemoembolization

TACE	Transarterial Chemoembolization
TCP	Tumour Control Probability
T:N	Tumour-to-Normal
TOF	Time of Flight
VOI	Volume of Interest
WHO	World Health Organization

Statement

E. Courtney Henry III provided consultation services to ABK Biomedical Inc. between January 2021 and March 2021. The nature of this work is unrelated to the research presented in this thesis.

Acknowledgements

The research project summarized in this thesis would not have been possible without the contributions of countless individuals. Although I cannot name them all, I would like to highlight several noteworthy contributors who proved to be vital to this success of this project.

First and foremost, I would thank my co-supervisors, Dr. Alasdair Syme and Dr. George Mawko, for their continuous patience, guidance, and mentorship. I'm grateful to have learned so much from these high-quality role models.

I'd also thank my committee members, Dr. Krista Chytyk-Praznik and Dr. James Clarke, for their invaluable input throughout the lengthy duration of this project. Following our meetings, your feedback always provided me with motivation and optimism.

This project was multidisciplinary in nature and required expert advice from several fields of research. Thank you to our research collaborators, including ABK Biomedical, BIOTIC Imaging, and Dr. John Frampton from the Biomedical Engineering Department of Dalhousie University.

Of course, this project could not have been undertaken without the financial support of the Beatrice Hunter Cancer Research Institute and the Nova Scotia Health Authority. Thank you both for your investment.

Thank you to my medical physics colleagues who were always available and willing to exchange research ideas and provide fresh insight. It has truly been a pleasure to work with each and every one of you.

Finally, a special thanks to my closest friends and loving family. Your consistent, overwhelming support helped me through the most challenging phases of this project. I could not have come this far without you all.

Chapter 1 Introduction

1.1 Preamble

It is estimated that approximately 50% of all cancer patients should receive external beam radiotherapy (EBRT) in the management of their disease.[1] As an essential cornerstone in the treatment of cancer, EBRT technology continues to grow in sophistication and complexity.[2] To produce accurate estimates of a patient's 3D dose distribution in EBRT, high-resolution computed tomography (CT) imaging is combined with sophisticated dose calculation algorithms.[3,4] This approach to radiation dosimetry facilitates an excellent understanding of the dose-response relationship.[5–7] Still, EBRT suffers from fundamental limitations. Healthy tissue, both proximal and distal to the target, is unavoidably irradiated during treatment. Furthermore, the tolerance of healthy tissue to radiation necessitates fractionation in the delivery, which requires multiple treatments and inconvenience to the patient. Alternative forms of radiation therapy, such as brachytherapy, offer solutions to overcome the limitations of EBRT. In brachytherapy, radiation is administered internally through implanted radioactive seeds to minimize the irradiation of surrounding healthy tissue and increase the maximum deliverable dose to the target volume.[8]

In transarterial radioembolization (TARE) – the focus of this thesis – radioactive microspheres are administered through the liver's arterial vasculature to selectively target and treat liver cancer. In TARE, the dose-response relationship is poorly understood. The absorbed dose can be estimated through single photon emission computed tomography (SPECT) or positron emission tomography (PET) imaging, but in many cases, post-treatment dosimetry is not performed. Moreover, PET and SPECT imaging suffer from poor spatial resolution.[9–11] This deficiency highlights an unmet clinical need for improved spatial resolution imaging of the microsphere distribution. Fortunately, a radiopaque microsphere has recently been developed that is readily visible through high-resolution CT imaging, allowing for a significant increase in spatial resolution and improved dose estimates relative to those derived from SPECT and PET imaging.

In TARE, technical success can be determined by accurately assessing the dose distribution and its relationship to the initial treatment plan. This is in contrast with clinical success, which is quantitatively related to dose-response and radiobiological concepts. The research presented in this thesis pertains to technical success in TARE. Specifically, the global objective of this thesis is to address the unmet clinical need to provide substantially higher spatial resolution imaging of microsphere distributions to facilitate more accurate dosimetry. To that end, this thesis describes the development, implementation, and validation of a CT-based framework for post-treatment dosimetry in TARE.

1.2 Liver Cancer

Primary liver cancer comes in many forms. The most common type is hepatocellular carcinoma (HCC), which comprises between 75% and 85% of all cases.[12] HCC constitutes 4.7% of world-wide cancer incidence with ~906,000 cases diagnosed each year, making it the sixth most common form of cancer.[12] Its poor prognosis makes it the third leading cause of cancer mortality representing 8.3% of all cancer deaths, corresponding to ~830,000 deaths each year.[12] Unlike most common cancers, HCC incidence and mortality rates are increasing, particularly in Europe and North America where incidence has been historically low.[12] These somber statistics motivate research into improving the quality of the treatment for HCC patients.

1.2.1 Staging and Treatment

The approach to treating HCC is complex due a variety of patient considerations. These include, but are not limited to, tumour burden, preserved liver function, previous and concomitant therapy, treatment goals, and quality of life. The Barcelona Clinic Liver Cancer (BCLC) classification is widely accepted in clinical practice as the *de facto* staging system for the treatment of HCC.[13] This system classifies the disease into five stages which integrate tumor burden, liver function, and patient performance status. These factors determine the stage of the cancer, which then links to prognosis and a systematic framework to guide HCC patients to the most effective treatment option. A diagram outlining the BCLC classification system is provided in

Figure 1.1.

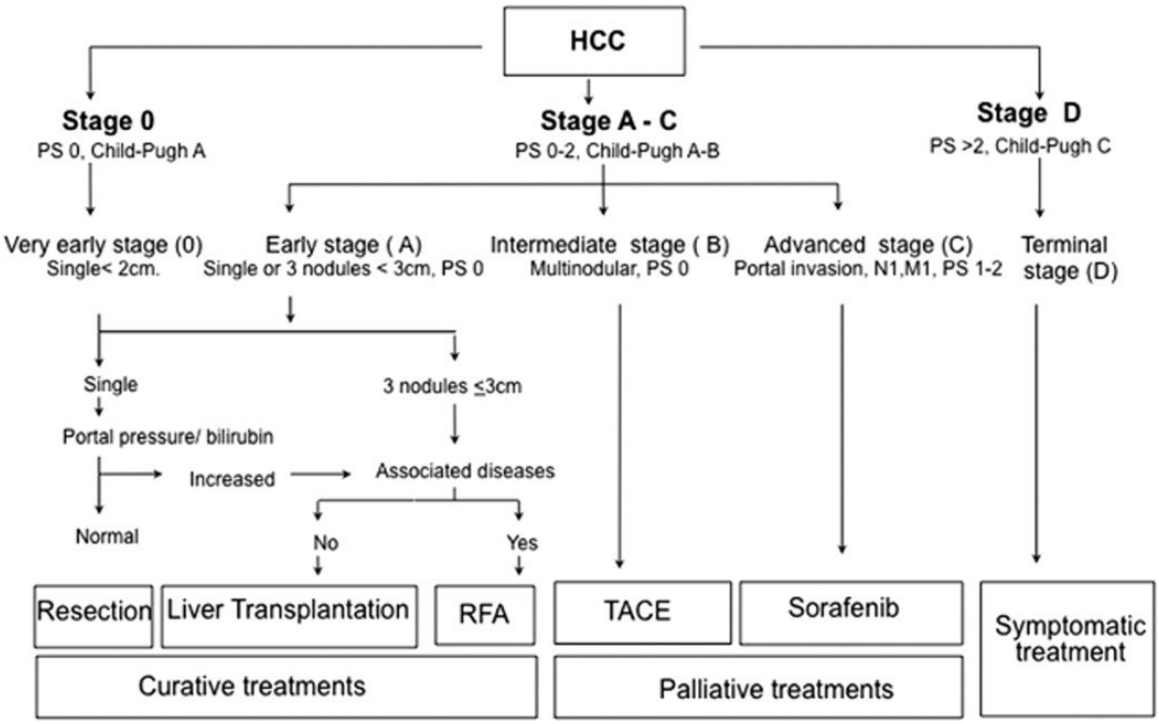

Figure 1.1: BCLC staging system to link HCC prognosis with viable treatment options. Reprinted from Bruix et al., Management of Hepatocellular Carcinoma: An Update.[14] Abbreviations: M, metastasis; N, node; PS, performance status; RFA, radiofrequency ablation; TACE, transarterial chemoembolization.

Therapeutic approaches in the treatment of HCC are classified into three categories: curative, palliative, and symptomatic. For palliative treatment, the three-year survival rate is typically between 10% and 40%, while patients receiving symptomatic treatment have an estimated survival time of less than three months.[15] All treatments listed in

Figure 1.1 are available within Nova Scotia, Canada. In fact, in 2019 (the most recent year with both provincial and national statistics), there were 53 liver transplantations in Nova Scotia out of the 610 within Canada (~10%).[16,17]

Surgical resection of the tumour remains a curative option for very early-stage HCC. A study surveying ~4,000 HCC patients demonstrated the utility of a resection-first strategy in non-cirrhotic patients with 50% of patients surviving after three years.[18] Liver transplantation is preferred for the treatment of early-stage HCC, particularly in patients with cirrhosis as it simultaneously removes hepatic tumours and the underlying disease.[19] Regrettably, the majority of patients (~95%) are ineligible for this procedure because they

don't meet transplantation criteria, have access to a transplant center, or face a shortage in organ availability.[20]

Tumor ablation is recommended for patients with very early- or early-stage HCC who are not candidates for surgical resection. Ablative treatments cause cell death through extreme temperature changes in the tumour microenvironment, as in radiofrequency ablation, microwave ablation, and cryoablation.[21] Ablation can also be achieved through chemical means by the percutaneous injection of ethanol and concentrated acetic acid into the tumour volume, which has been shown to be effective in treating small, solitary HCC.[22] Irreversible electroporation, another ablative technique, can induce cell death by rupturing cell membranes through the application of a high voltage across the target tissue.[23]

The BCLC staging system recommends treating advanced-stage HCC with sorafenib, an inhibitor that blocks the action of a group of enzymes known as tyrosine kinases. These enzymes play a role in cell signaling, division, and growth, and are found in high concentrations in HCC.[24] Despite the established chemoresistance of HCC,[25] results from a phase III clinical trial suggest a significant increase in median overall survival and time to progression in patients with advanced-stage HCC when compared with best supportive care.[26]

EBRT has played a limited role in the treatment of HCC due to the radiation exposure of large volumes of healthy liver tissue, which is highly radiosensitive.[27] In conventionally fractionated EBRT, accumulated data suggest a whole-liver normal tissue complication probability (NTCP) of 5% at 5 years for a mean absorbed dose of approximately 30 Gy.[5] This is a major limitation in dose escalation and the re-irradiation of the liver. Furthermore, excessive healthy liver tissue irradiation may cause radiation-induced liver disease (RILD), a form of liver injury due to radiation which presents as classical (absence of underlying liver disease) and non-classical (presence of underlying liver disease). RILD may result in serious chronic side effects and has no specific treatment guidelines.[28] Fortunately, recent technological developments have broadened the applicability of EBRT in treating HCC. Stereotactic body radiation therapy (SBRT) is capable of delivering a highly conformal dose in the tumoricidal range while simultaneously minimizing the dose to surrounding healthy liver tissue.[29] Results of a

Phase I/II trial of SBRT for HCC patients unsuitable for standard locoregional therapies demonstrated that SBRT can lead to sustained local control (87% at one year) with a low risk of serious toxicity.[30]

Healthy liver tissue receives approximately 80% of its blood supply from the portal venous system while the hepatic artery supplies liver tumours with 80-100% of its blood supply.[31] Embolic therapies, such as bland embolization or transarterial chemoembolization (TACE), exploit this unique differential perfusion of the liver to target hepatic tumors.[32] Bland embolization relies on small particles (40-120 μm) to occlude the tumor's arterial blood supply resulting in ischemic necrosis of the tumour. It has been shown to be effective in treating HCC with a median survival time of 21 months and 1-, 2-, and 3-year overall survival rates of 66%, 46%, and 33%, respectively.[33] TACE is the current standard of care in patients with intermediate-stage HCC, and can be categorized as either conventional TACE (cTACE) or TACE with drug-eluting beads (DEB-TACE). In cTACE, a tumour's arterial blood supply is selectively occluded of a by the injection of chemotherapeutic agents, typically doxorubicin. A large randomized study showed that cTACE is superior to bland embolization with survival probabilities of 82% and 63% at 1 and 2 years, respectively.[34] To allow for higher chemotherapeutic drug concentrations, DEB-TACE employs drug-loaded microspheres as a delivery mechanism, and has been shown to have a higher complete response rate, a higher overall survival rate, and fewer adverse events than cTACE.[35]

1.3 Transarterial Radioembolization

The majority of HCC patients (60-70%) present at the advanced stage of disease.[36] If they cannot tolerate the toxicity associated with chemotherapy, TARE is an alternative treatment option. TARE, also known as selective internal radiation therapy (SIRT), is a radiation-based embolic therapy in which radiolabeled microspheres are administered within the hepatic arterial vasculature via a microcatheter to facilitate the delivery of radiation to a target volume. As is the case with the other embolic therapies, TARE relies on the preferential blood supply of HCC.

TARE provides clear benefits relative to TACE. For example, TARE offers the significant clinical advantage of being an outpatient treatment in most cases.[32] It has also

been shown to slow tumour progression, have similar overall survival outcomes, and produce fewer post-embolization syndromes relative to TACE.[32,37] An explanation for this lies in the fact that TARE utilizes smaller microspheres (20-30 μm) and their efficacy is believed to derive more from the prolonged emission of high-energy beta (β^-) particles than from an embolic effect.[32,38]

Recent studies have compared TARE and SBRT in terms of safety and efficacy and found them to be roughly equivalent. Results from a retrospective review of a large cohort of unresectable HCC patients showed no significant differences in overall survival when treated with TARE relative to SBRT (hazard ratio = 0.72, p = 0.108).[39] Another study demonstrated that a patient cohort, treated with either TARE or SBRT, did not present any grade 3 liver toxicities based on the common terminology criteria for adverse events 4.0 (CTCAE).[40] Despite these conclusions, a study designed to quantify the prevalence of EBRT (inclusive of SBRT) in HCC patients (n = 18,477) waitlisted for liver transplantation found that 85.% of patients received ablative or embolic therapies, while just 3.6% were treated with EBRT.[41]

Although TARE is not a recommended treatment for HCC in the BCLC system, there is abundant data suggesting its efficacy across all stages of disease. For patients in the early-stage, multiple studies have reported consistent median overall survival times of ~26 months following TARE.[42–44] TACE is the standard of care for HCC patients at the intermediate stage. However, as previously mentioned, TARE has similar overall survival outcomes and produce fewer post-embolization syndromes relative to TACE.[32,37] Although sorafenib is recommended for advanced-stage HCC, accumulating evidence suggest TARE can offer a similar survival benefit.[44,45]

TARE has now been integrated into clinical practice for more than 20 years, yet the indications for TARE continue to grow.[46] It is no longer limited to palliative indications, but rather as a bridge therapy to reduce tumour burden and potentially render a patient eligible for transplant.[47] TARE has also been applied in the treatment of metastatic liver disease.[48] Ultimately, all patients who are ineligible to receive surgery may eventually be considered eligible for TARE. Over the past decade, national and international organizations, including the American Association of Physicists in Medicine (AAPM) and

Radioembolization Brachytherapy Oncology Consortium (REBOC), have established interdisciplinary working groups to develop recommendations for the standardization of indications, techniques, treatment approaches, and dosimetry in TARE.[49–51]

1.3.1 Microspheres

Two types of yttrium-90-labelled (^{90}Y) microspheres for TARE have achieved global commercial availability. In 2002, SIR-Spheres® (Sirtex Medical Inc., Woburn, MA, USA) received FDA approval for the treatment of metastatic colorectal cancer and received the CE mark of approval for the treatment of inoperable hepatic tumours, although they are not yet licensed for use in Canada. TheraSphere® microspheres (Boston Scientific Corp., Marlborough, MA, USA) received FDA approval in 1999 for the treatment of HCC, as well as Health Canada the CE approval in 2005 for the treatment of inoperable hepatic tumours. Although both types of microspheres are biocompatible, neither are biodegradable nor metabolized. Characteristics of both microsphere products are provided in Table 1.1.[52,53]

Commercial Name	**TheraSphere**	**SIR-Spheres**
Microsphere Composition	Glass	Resin
Diameter [μm]	32 ± 10	25 ± 10
Specific Activity [Bq/MS]	2500	50
Activity per Vial [GBq]	3, 5, 7, 10, 15, 20	3
Microspheres per Vial	3 - 8 x 10^6	30 - 60 x 10^6
Density [g/mL]	3.2	1.6

Table 1.1: Characteristics of commercially available ^{90}Y-labelled microspheres.

A stark difference in the characteristics reported in Table 1.1 lies in the specific activity of the microspheres (at the time of calibration), which differs by a factor of 50 between resin and glass microspheres. As a result, fewer glass microspheres are delivered compared to resin microspheres (for the same administered ^{90}Y activity), which produces subtle differences in the microscopic distribution of the microspheres.[54] This may explain the significant difference between the absorbed dose required to reach a tumour control probability (TCP) of 50% for glass and resin microspheres.[55,56] Furthermore, a microsphere transport simulation performed by Walrand *et al.* found that the relatively low number of

administered glass microspheres results in non-uniform trapping of microspheres in the portal tract, which caused healthy liver tissue volumes to receive sub-lethal doses. This effect may explain the reduced toxicity of glass microspheres compared to resin microspheres.[57]

As the therapeutic agent, the radioisotope ^{90}Y is considered a pure β^- emitter that decays to stable zirconium-90 (^{90}Zr) with a physical half-life of 64.24 ± 0.30 hours (2.68 days), achieving 95% decay of the radioactivity within 11.5 days.[58] The maximum and mean β^- energies are 2.2787 ± 0.0013 MeV and 0.9267 ± 0.0008 MeV, respectively, corresponding to a range in water of 11.0 mm and 2.4 mm.[59,60] The therapeutic range X_{90} in water is 5.4 mm, where X_{90} is defined as the radius of a sphere containing 90% of the absorbed dose.[61] These properties make ^{90}Y the radioisotope of choice for TARE due to the continuous dose delivery over a prolonged period of time, while still restricting the dose deposition to the immediate vicinity of the microspheres.

1.3.2 Pretreatment Workup

Patients undergo a thorough pre-treatment workup to determine eligibility for TARE. This workup includes laboratory and clinical investigations, anatomical imaging, angiographic mapping, and a simulation scan to estimate the *in vivo* microsphere distribution. The various stages of the pre-treatment workup are shown in Figure 1.2.

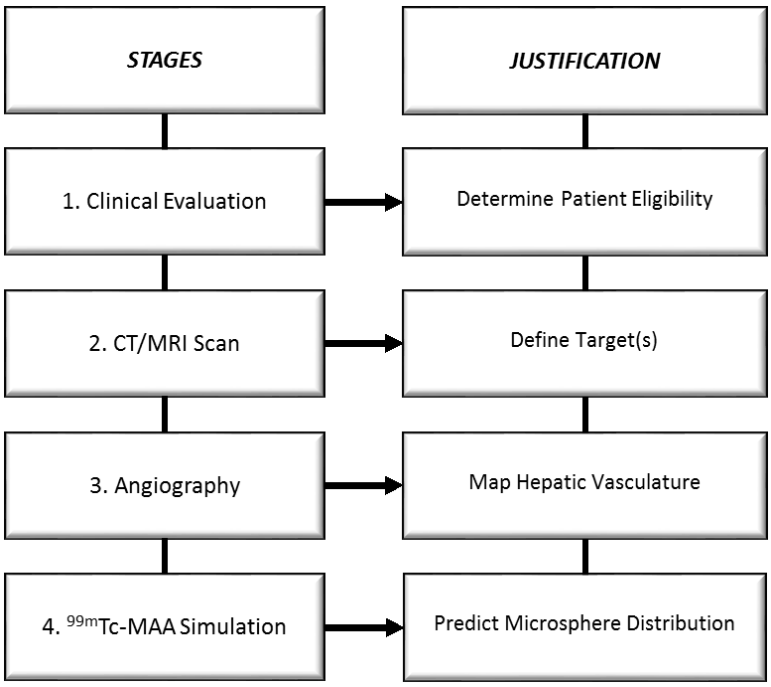

Figure 1.2: Clinical stages and associated justifications for the pre-treatment workup in ^{90}Y TARE. Figure adapted from Kim *et al.*, A Guide to ^{90}Y Radioembolization and its Dosimetry.[62]

To begin, the laboratory and clinical investigations assess the patient's general clinical status, vital functions, and baseline values as a reference for subsequent toxicity assessments. Liver function is assessed through an analysis of the concentration of liver-specific compounds within the blood stream, such as albumin and bilirubin.[63] During this preliminary stage, patients are also examined for relative and absolute contraindications to determine eligibility for TARE, including portal vein thrombosis and portal hypertension.[64]

Following the laboratory and clinical investigations, patients undergo anatomical imaging through either a multi-phase CT scan or magnetic resonance imaging (MRI) to determine tumoural and non-tumoural volumes, as well as potential extrahepatic disease. Next, baseline angiography is performed using high-resolution digital subtraction angiography (DSA) and contrast-enhanced CT to map the hepatic arterial anatomy.[50] The classic hepatic arterial supply arises from the celiac artery with a bifurcation of the proper hepatic artery into the left and right hepatic arteries. However, ten prominent hepatic anatomical variants are categorized, highlighting the importance of performing pre-treatment angiographic imaging to evaluate the hepatic arterial anatomy.[65] Angiography

also allows for potential prophylactic coil embolization of hepatic arterial branches, if necessary, and for the determination of the optimal catheter position to administer a simulation scout tracer and subsequent ^{90}Y microspheres.

Unlike other forms of radiotherapy, accurate dosimetry cannot be predicted in ^{90}Y TARE, although an estimate of the microsphere distribution following administration can be achieved through a simulation of the treatment using Technetium-99m-labelled macro-aggregated albumin (^{99m}Tc-MAA) SPECT imaging. During this procedure, 100-200 MBq of ^{99m}Tc-MAA is injected into the tumour's hepatic arterial vasculature and follow-up SPECT imaging provides an estimation of the ^{90}Y microsphere distribution. It also provides a means to quantify the degree of lung shunting and predict gastrointestinal microsphere uptake. It is currently recommended that the mean lung dose should not exceed 30 Gy for an individual treatment as to mitigate the risk of radiation pneumonitis, although accumulating data suggest this toxicity threshold is likely overestimated.[66]

There is controversy over the capacity of ^{99m}Tc-MAA to successfully mimic the *in vivo* ^{90}Y microsphere distribution. A retrospective study of 83 patients with HCC treated with glass microspheres demonstrated that ^{99m}Tc-MAA SPECT is a poor surrogate to quantitatively predict HCC tumour dose, as measured the reproducibility coefficient (2.4 for ^{99m}Tc-MAA SPECT vs. 1.6 for ^{90}Y PET), and that further work is needed to find a more reliable methodology to perform pre-treatment dosimetry.[67] This may be a result of the broad diameter range of ^{99m}Tc-MAA particles (10-100 μm), a significant difference in the number of ^{99m}Tc-MAA particles administered (~0.5 x 10^6), or catheter position differences between simulation and treatment. Conversely, there is research that shows ^{99m}Tc-MAA tumor-to-normal (T:N) liver perfusion ratios serve as good response predictors, and also facilitate the pre-treatment planning and estimation of the required amount of administered ^{90}Y activity.[68–70]

Treatment planning in ^{90}Y TARE is based on simplistic formulae that relate a desired liver dose to the administered ^{90}Y activity. The body-surface area (BSA) method, typically used for treatment planning with resin microspheres, was originally developed to overcome the high toxicities resulting from treatment planning with an early, overly simplistic empirical approach.[71] The BSA method considers the patient's tumour mass, healthy liver mass, and BSA while assuming a correlation between BSA and liver volume

in a healthy population.[72] However, there is evidence to suggest the absorbed dose to the liver does not correlate with the administered activity when using the BSA method for treatment planning.[73] Consequently, patients with small livers are generally overdosed and patients with large livers are underdosed.[73–75]

A non-empirical approach is the mono-compartment method, also referred to as the medical internal radiation dose (MIRD) method. In this model, the desired absorbed dose is set assuming a homogeneous distribution of microspheres within the target volume such that 1 GBq of ^{90}Y activity distributed within 1 kg of liver tissue will provide a mean absorbed dose of ~50 Gy.

The final approach to treatment planning uses the partition model – a patient-specific, three-compartment model that is tailored to desired dosimetric endpoints for the lungs, healthy liver, and tumour. As inputs, the partition model requires patient-specific tumour volumes, healthy liver volumes, and a T:N uptake ratio. While the partition model is superior to the mono-compartment model, it is still an approximation which fails if multiple tumours are present with varying uptake ratios.

1.3.3 Treatment

Once a patient is deemed eligible for TARE, ^{90}Y microsphere administration is performed as an outpatient procedure. First, selective catheterization of the appropriate hepatic arterial vessel (chosen during pretreatment angiography) is carried out under the guidance of DSA. Once the catheter is in place, microspheres are released into the vasculature. Unfortunately, commercially available microspheres are administered blindly following catheter placement. This prevents any evaluation of the microsphere distribution during the procedure.

Efforts to visualize the microsphere distribution and perform intra-procedural dosimetry during administration using have been investigated. The feasibility of visualizing iron-labelled microspheres using MRI for *in vivo* microsphere tracking during their administration into a porcine model has been demonstrated.[76] Pinhole bremsstrahlung SPECT imaging using a camera mounted on a robotic arm was shown to provide a fast dosimetry assessment, suggesting it could be used to optimize the administered ^{90}Y activity.[77] A maneuverable time of flight (TOF) PET system with near real-time image

reconstruction capability has recently been investigated which could potentially enable real-time dosimetry in ^{90}Y TARE.[78] A hybrid imaging system was proposed consisting of an X-ray C-arm combined with a gamma camera for simultaneous nuclear medicine and fluoroscopic imaging capabilities.[79] Despite these recent efforts, MRI, SPECT, and PET imaging are not yet clinically implemented for real-time microsphere tracking and intra-procedural dosimetry as they present significant infrastructure costs and increased procedural complexity.

TARE is performed in interventional radiology suites which are typically equipped with DSA and cone beam CT (CBCT). These X-ray imaging modalities may be sufficient to perform microsphere tracking and intra-procedural dosimetry during microsphere administration in ^{90}Y TARE when using radiopaque ^{90}Y microspheres. A brief discussion on the potential benefits of this approach are presented in Section 7.2.

1.3.4 Treatment Verification

Potential discrepancies in the particle distribution between the pre-treatment ^{99m}Tc-MAA simulation and the ^{90}Y microspheres suggests that post-treatment imaging should be performed to determine the true microsphere distribution and corresponding absorbed dose distribution. The *in vivo* ^{90}Y microsphere distribution is typically determined through the imaging of bremsstrahlung radiation produced as ^{90}Y β^-particles traverse the soft tissue and interact with atomic nuclei. Bremsstrahlung radiation can be detected using SPECT imaging. In quantitative SPECT, scatter rejection and attenuation correction methods rely on readily identifiable characteristics in the bremsstrahlung energy spectrum. However, bremsstrahlung radiation is ill-suited for quantitative SPECT imaging as it lacks a well-defined photopeak. To optimize performance, two major parameters that are investigated in SPECT data acquisition are the choice of collimator and the energy window used for data collection. Monte Carlo (MC) simulations of clinical SPECT scanners have shown that medium-energy collimators and energy windows of 100-150 keV provide optimal image contrast[80], and phantom studies with various tumour sizes and ^{90}Y activity concentrations have corroborated these findings.[81,82] Despite the large number of studies aiming to improve bremsstrahlung SPECT imaging, most approaches require the use of computationally intensive MC methods and are therefore not routinely implemented in

clinical practice. Instead, simple bremsstrahlung SPECT protocols are established with CT-based attenuation corrections and energy window-based scatter corrections that are easily implemented on clinical SPECT scanners.

Although ^{90}Y is regarded as a pure β^- emitter, there is a small probability of decay through the β_{01}^- pathway to the 0^+ first excited state of ^{90}Zr at 1.76 MeV, followed by another decay through internal pair production (β^+/β^- emission) with a branching ratio of $31.86 \pm 0.47 \times 10^{-6}$ to stable ^{90}Zr.[83] The decay scheme of ^{90}Y is shown in Figure 1.3.

Figure 1.3: Decay scheme of ^{90}Y. This figure was reproduced based on Nickles *et al*., A New Internal Pair Production Branching Ratio of ^{90}Y: The Development of a Non-Destructive Assay for ^{90}Y and ^{90}Sr.[83]

The emission of a β^+ particle in this transition allows for the imaging of ^{90}Y microspheres using PET. Although ^{90}Y was found to decay via internal pair production in 1955,[84] it wasn't until 2009 that this pair production was used to determine the *in vivo* ^{90}Y microsphere distribution using PET imaging.[85] Since then, PET has been increasingly used in ^{90}Y TARE and has been shown to be superior to bremsstrahlung SPECT in the assessment of target and non-target activity.[86] Despite encouraging results in the verification of the ^{90}Y microsphere distribution using PET, it is subject to inherent limitations. The primary issue associated with ^{90}Y PET imaging is this extremely small branching ratio associated with internal pair production, which requires high administered ^{90}Y activities and relatively long scan times (10-40 minutes/bed position).[86] Most modern PET scanners used for post-treatment verification in ^{90}Y TARE are equipped with lutetium-

based scintillator crystals due to their high density and excellent temporal resolution[87], however, the naturally occurring radioisotope lutetium-176 (^{176}Lu) gives rise to undesirable background counts within the scintillator (2.6% of naturally occurring lutetium is ^{176}Lu), reducing system performance and complicating accurate quantification under the low-count conditions in ^{90}Y PET. In addition, many PET workstations don't offer ^{90}Y as a radionuclide choice for PET scans. In these cases, other radionuclides within the software package must be chosen and corrected for the different ^{90}Y half-life and positron branching ratio.[88]

While it has been shown that PET can produce quantitative images of ^{90}Y microsphere distributions, further research is required to determine the ideal image reconstruction techniques and acquisition parameters for PET imaging in post-treatment dosimetry following ^{90}Y TARE.[49–51]

1.3.5 Microsphere Distribution

Dosimetry based on post-treatment PET and SPECT imaging may be put into context by describing true dose heterogeneity observed in pathohistological studies of explanted tissue samples. The earliest study of the non-uniformity of the microsphere distribution was performed in 1991 by Fox *et al*., who analyzed a cubic centimeter of liver tissue following ^{90}Y TARE and found extreme dose gradients varying more than five orders of magnitude over a distance of only 2 mm.[89] It was also shown that a third of the examined volume received less than 33.7% of the predicted dose. A study by Roberson *et al*., published less than one year later, performed a similar analysis on a VX2 rabbit tumour model and estimated that the minimum tumour dose (31 Gy) was less than half of the average tumour dose (71 Gy).[90] The next landmark studies were performed over a decade later by Kennedy *et al*. and Campbell *et al*. Following the explant of a liver after ^{90}Y TARE, Campbell found microsphere densities of ~250 MS/mm^3 at the tumour-normal liver interface – a factor of ~70 greater than the density in the normal liver.[91] Subsequent estimates of average doses within the tumour periphery ranged from 200 to 600 Gy.[92] Kennedy later presented a complete pathological analysis of four explanted livers previously treated with ^{90}Y TARE.[54] The study revealed extremely high doses varying from 100 to 8000 Gy and a preferential deposition of microspheres at the tumour edge compared to the center of the tumour or the normal liver with ratios from 3:1 to 20:1.

1.3.6 Dose-Response Relationship

As previously mentioned, healthy liver tissue has a relatively poor tolerance to radiation.[27] In EBRT, an absorbed dose of 30-35 Gy to the whole liver increases the risk for RILD.[5] However, in TARE, toxicity limits are twice as large at 70-80 Gy.[89,92,93] There have been cases where the healthy liver mean dose has exceeded 100 Gy without complications.[94] The difference between EBRT and TARE healthy liver toxicity thresholds is attributed to differences in the dose rate (~1 Gy/min in EBRT compared to ~0.001 Gy/min in TARE) and dose heterogeneity (microscopic sparing of healthy tissue in TARE).[95]

Tumour response to therapy can be measured by anatomical changes in tumour size, density, or metabolic activity. There are four commonly used guidelines in the assessment of tumour response following TARE: the World Health Organization (WHO)[96], European Association for the Study of Liver (EASL)[97], response evaluation criteria in solid tumours (RECIST)[98], and the modified response evaluation criteria in solid tumours (mRECIST)[99]. Although most evidence supporting a dose-response relationship in ^{90}Y TARE is based on retrospective studies, there is evidence that shows a correlation between absorbed dose, tumour response, and overall survival. However, a precise tumour dose threshold for objective tumour response is yet to be defined.[100] A review of retrospective dose-response studies for HCC patients receiving glass microspheres shows that the reported mean dose required to elicit an objective tumour response varies by a full order of magnitude.[101] To further highlight this inconsistency, one study reported a mean dose of 100 Gy for responders[102] while another study reported a mean dose of 147 Gy for non-responders.[103] This blatant contradiction suggests we need an improved approach to quantifying the dose-response relationship. Recently, the DOSISPHERE-01 trial became the first randomized, prospective study in ^{90}Y TARE. It demonstrated that personalized dosimetric treatment planning resulted in a significant increase both in objective response (71% vs. 36%) and survival (26.6 months vs. 10.7 months), without an increase in liver toxicity.[104]

Efforts in exploring alternative dose-response metrics have also been investigated in predicting response in ^{90}Y TARE. Dose-volume metrics ranging from D_{20} to D_{80} have

been shown to correlate with tumour response, where D_{20} to D_{80} represent the minimum dose received by 20% and 80% of the tumour volume, respectively.[103,105,106]

If accurate dose thresholds and healthy tissue toxicity limits can be established, and post-administration imaging can verify the microsphere distribution and corresponding absorbed dose, a viable dose-response relationship can be established and should translate into improved patient outcomes.

1.4 Limitations

While PET and SPECT voxelized ^{90}Y activity data can provide reasonably reliable estimates of average absorbed dose values at the macroscopic level[107], its utility for relating absorbed dose to outcome is associated with large uncertainties. This may be partially attributed to their poor spatial resolution, measured by the full width at half-maximum (FWHM), which is reported to range from 7.0 to 30.0 mm for bremsstrahlung SPECT and between 5.0 and 10.0 mm in ^{90}Y PET.[9–11] This is several times larger than the average range of ^{90}Y β^-emissions in tissue (2.4 mm) and is orders of magnitude larger than the distance scales over which changes in microsphere concentration (microns) can take place.[91]

Still, TARE has tremendous potential to provide clinicians with highly quantitative dosimetric data as ^{90}Y activity is deposited in discrete locations (since it is coupled to the microspheres) and the spatial patterns of dose deposition from ^{90}Y sources are well-known. It follows that the only required information is an accurate description of the microsphere distribution with the target volume. Fortunately, a novel preclinical glass microsphere (Eye90) has been developed by ABK Biomedical (Halifax, NS, Canada) that is radiopaque and readily visible through high-resolution CT imaging. This development allows for an accurate determination of the radiopaque microsphere spatial distribution as a result of a significant increase in spatial resolution imaging, and therefore provides a means to extract improved dose estimates relative to those derived from SPECT and PET imaging.

An additional, a non-technical benefit of CT imaging over PET imaging lies in its economic advantage. A study in the United States showed oncological PET/CT imaging costs the patients an additional 57% relative to CT imaging after six months post-treatment.[108] Furthermore, an Italian institution performed a cost-analysis study that

suggested an institutional cost savings of 54% when using contrast-enhanced CT relative to PET in oncological imaging.[109] We can conclude that CT imaging provides an advantage to PET imaging not only in terms of spatial resolution, but also in its economic impact to both patients and medical institutions.

1.5 Research Objectives

This thesis presents the development, implementation, and validation of a CT-based framework for post-treatment dosimetry in ^{90}Y TARE, and is comprised of a series of three manuscripts, each addressing a specific research objective.

Manuscript 1 is presented in Chapter 3 and addresses the first objective – to quantify the inherent radiopacity of novel glass microspheres that will allow for the development of calibration curves to relate radiopaque microsphere concentration within a CT voxel to the corresponding voxel intensity. The manuscript reference is provided below.

- Henry, C., Mawko, G., Tonkopi, E., Frampton, J., Kehoe, S., Boyd, D., Abraham, R., Gregoire, M., O'Connell, K., Kappadath, S., Syme, A. (2019). Quantification of the Inherent Radiopacity of Glass Microspheres for Precision Dosimetry in Yttrium-90 Radioembolization. *Biomedical Physics & Engineering Express*, 5, 055011.

The results detailed in manuscript 1 motivated the construction of a clinical calibration phantom whose design and analysis spanned the remainder of the project. The clinical calibration phantom analysis is presented in Chapter 6.

Manuscript 2 is presented in Chapter 4 and addresses the second objective – to perform dosimetry in ^{90}Y TARE by convolving dose kernels with simulated ^{90}Y activity distributions derived from micro-CT imaging of non-radioactive, radiopaque microspheres distributions within a porcine renal model. Furthermore, the impact of the spatial resolution of an imaging system on the extraction of specific dose metrics was investigated. The manuscript reference is provided below.

- Henry, C., Strugari, M., Mawko, G., Brewer, K. D., Abraham, R., Kappadath, S., Syme, A. (2021). Post-administration Dosimetry in Yttrium-90 Radioembolization through Micro-CT Imaging of Radiopaque Microspheres in a Porcine Renal Model. *Physics in Medicine & Biology*, 66, 095011.

Manuscript 3 is presented in Chapter 5 and addresses the third objective – to perform dosimetry in ^{90}Y TARE through clinical CT imaging of radiopaque ^{90}Y microspheres in a rabbit liver model, and to compare the CT-based dose metrics to those produced from conventional PET-based dosimetry. The manuscript reference is provided below.

- Henry, C., Strugari, M., Mawko, G., Brewer, K., Abraham, R., Liu, D., Gordon, A., Bryan, J., Kappadath, S., Syme, A. (2021). Precision Dosimetry in Yttrium-90 Radioembolization through PET/CT Imaging of Radiopaque Microspheres in a Rabbit Liver Model. *European Journal of Nuclear Medicine & Medical Imaging - Physics. DOI: 10.21203/rs.3.rs-806070/v1*

The second chapter of this thesis describes the theoretical and methodological framework that is required to successfully interpret subsequent chapters. The seventh and final chapter of this thesis will summarize the key findings of this work and suggest avenues for future research.

Chapter 2 Theory

As a foundation for the remainder of the thesis, this chapter presents the theoretical and methodological tools relevant to this work. Given the multidisciplinary nature of this research, concepts from both diagnostic imaging and nuclear medicine are presented. Specifically, the theoretical framework of radioactivity is outlined in Section 2.1, with an emphasis on decay pathways relevant to ^{90}Y TARE. The physics of photon interactions relevant to PET and CT imaging are presented in Section 2.2, followed by charged particle interactions in Section 2.3. Approaches to radiation dosimetry are provided in Section 2.4. An overview of the fundamental principles of CT and PET are provided in the final two sections, Section 2.4 and Section 2.5, respectively.

2.1 Radioactivity

Radioactivity, or radioactive decay, was discovered by French physicist Henri Becquerel in 1896. Radioactive decay is a spontaneous and stochastic process in which an unstable nucleus transforms into one or more daughter nuclei. This transformation is accompanied by the emission of energetic particles (protons, neutrons, electrons, or positrons), high-energy photons (gamma rays), or both. The activity $A(t)$ of a radioactive material containing a large number of identical radionuclides $N(t)$ represents the total number of nuclear decays (disintegrations) per unit time and is defined as a product of $N(t)$ and λ, as demonstrated in Equation 2.1.

$$A(t) = \lambda N(t) \tag{2.1}$$

Here, λ is a unique, radionuclide-specific characteristic called the decay constant. It represents the fraction of nuclei that will decay per unit time and is typically expressed with dimensions of reciprocal time, s^{-1}. The SI unit of activity is the Becquerel [Bq], where 1 Bq = 1 s^{-1}. The rate of depletion in the number of radionuclides $N(t)$ is described by Equation 2.2.

$$\frac{dN(t)}{dt} = -A(t) = -\lambda N(t) \tag{2.2}$$

This first-order differential equation is expressed in integral form in Equation 2.3.

$$\int_0^t \frac{dN(t)}{N(t)} = -\int_0^t \lambda \, dt \tag{2.3}$$

Under the assumption of an independent λ with respect to time, Equation 2.3 can be solved to produce an expression for the number of remaining nuclei at any time t.

$$N(t) = N_0 \, e^{-\lambda t} \tag{2.4}$$

Here, N_0 is the number of radioactive nuclei at time t = 0. Combining Equation 2.4 and 2.1, an expression for the activity $A(t)$ may be derived.

$$A(t) = \lambda N(t) = \lambda N_0 e^{-\lambda t} = A_0 e^{-\lambda t} \tag{2.5}$$

Here, A_0 is the initial activity of the radionuclide at time $t = 0$. Equation 2.5 applies to all radionuclides, regardless of their decay scheme. The decay constant is related to the half-life and mean lifetime of a radionuclide through Equation 2.6.

$$\lambda = \frac{\ln(2)}{\tau_{1/2}} = \frac{1}{\tau} \tag{2.6}$$

The half-life $\tau_{1/2}$ of a radionuclide is defined as the time is takes for an activity source to decay to 50% of its initial value. The mean lifetime τ of a radionuclide is greater than $\tau_{1/2}$ by a factor of $1/\ln(2) \approx 1.44$. Assuming a half-life $\tau_{1/2}$ = 64.24 hr, the decay constant for ^{90}Y is λ = 1.08 x 10^{-2} hr^{-1} or 3.00 x 10^{-6} s^{-1}. This corresponds to a mean lifetime of τ = 92.7 hr or τ = 3.34 x 10^5 s.

One form of radioactive decay relevant to ^{90}Y TARE is β^- decay, where a neutron-rich parent nucleus undergoes a nuclear transformation by converting a neutron into a proton and subsequently ejecting an electron e^- and electron antineutrino $\bar{\nu}_e$. In the case of ^{90}Y, this decay is described in Equation 2.7.

$$^{90}_{39}Y \rightarrow {}^{90}_{40}Zr + e^- + \bar{\nu}_e \qquad 2.7$$

As electrons are emitted from ^{90}Y nuclei, they experience coulombic interactions with nearby charged particles (e.g., atomic nuclei and orbital electrons). Inelastic collisions with nearby electrons result in a transfer of kinetic energy and subsequent absorbed dose to the medium, detailed later in Section 2.3. The kinetic energy lost in charged particle interactions with atomic nuclei is converted to bremsstrahlung radiation. The energy spectrum of bremsstrahlung radiation is continuous, ranging from zero to the maximum possible energy of the electrons. Bremsstrahlung emission is proportional to the square of the atomic number and inversely proportional to the square of the charged particles mass[110], and can provide an estimate of the ^{90}Y activity distribution through post-treatment SPECT imaging in ^{90}Y TARE.

As discussed in Section 1.3.4, there is also a small probability of internal pair production in the decay scheme of ^{90}Y through the β_{01}^- decay path to stable ^{90}Zr, as shown in Figure 1.3. Internal pair production is an alternative to gamma decay where an unstable nucleus having a minimum excess energy of 1.02 MeV ejects an electron-positron pair, as described by the reaction in Equation 2.8.

$$^{90}_{40}Zr^{*} \rightarrow {}^{90}_{40}Zr + e^{-} + e^{+} \quad (2.8)$$

Here, $^{90}_{39}Zr^{*}$ is the ^{90}Zr nucleus in an excited state and e^{+} is a positron. The production of a positron through internal pair production allows for post-treatment PET imaging to estimate the ^{90}Y activity distribution in TARE.

2.2 Interaction of Photons with Matter

Post-treatment imaging modalities used to estimate the ^{90}Y activity distribution in TARE rely on fundamental radiation interactions in matter. This section briefly describes these radiation interactions, beginning with the concept of photon attenuation.

2.2.1 Attenuation Coefficient

For a monoenergetic, narrow beam of photons with intensity I incident on a material of thickness dx, the reduction in intensity dI due to photon attenuation is proportional to a constant μ.

$$\frac{dI(x)}{dx} = -\mu I(x) \quad (2.9)$$

Upon integration and solving Equation 2.9 (note similarity with Equation 2.2), we can determine an expression for the photon intensity within the material $I(x)$. This is known as Beer's law and is given in Equation 2.10.

$$I(x) = I_o e^{-\mu x} \quad (2.10)$$

Here, I_o is the initial intensity of the incident photon beam and μ is the linear attenuation coefficient, typically expressed in units of cm^{-1}. This parameter is dependent on the energy of the photon and the atomic number of the material and may be physically interpreted as the probability a photon will interact in the material per unit path length. As μ is dependent on the physical density ρ of the material, it is often normalized by the density to yield $\frac{\mu}{\rho}$, the mass attenuation coefficient often expressed in units of cm^2/g.

The four major types of photon interactions relevant to diagnostic imaging and nuclear medicine are 1) Compton (incoherent) scattering, 2) photoelectric absorption, 3) pair production, and 4) Rayleigh (coherent) scattering. The total mass attenuation coefficient is the sum of the mass attenuation coefficients for each individual photon interaction and is provided in Equation 2.11.

$$\frac{\mu}{\rho} = \frac{\sigma_R}{\rho} + \frac{\sigma}{\rho} + \frac{\tau}{\rho} + \frac{\kappa}{\rho} \qquad 2.11$$

Here, $\frac{\sigma_R}{\rho}$ is the Rayleigh scattering contribution, $\frac{\sigma}{\rho}$ is the Compton scattering contribution, $\frac{\tau}{\rho}$ is the photoelectric absorption contribution, and $\frac{\kappa}{\rho}$ is the pair production contribution. The relative contribution from each photon interaction in soft tissue is shown in Figure 2.1 as a function of photon energy.

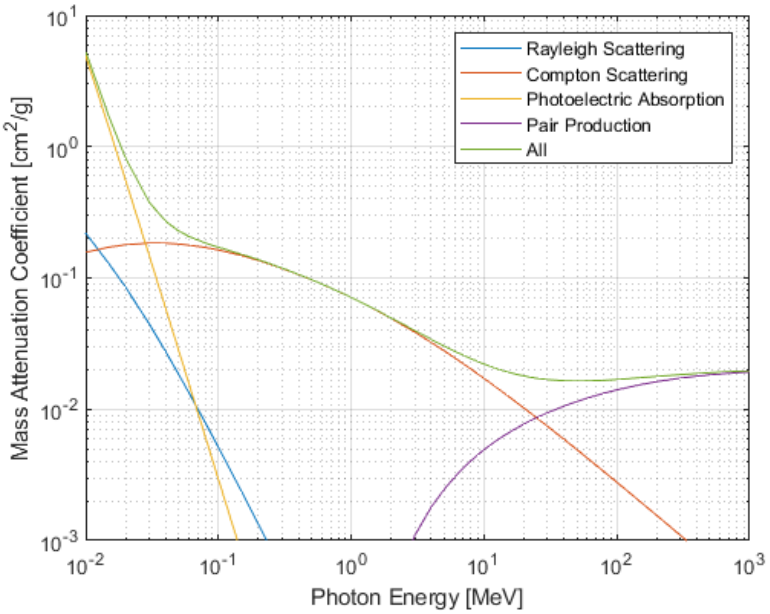

Figure 2.1: Mass attenuation coefficients for photon interactions in soft tissue as a function of photon energy.

In soft tissue, Rayleigh scattering and photoelectric absorption dominate at low photon energies, Compton scattering dominates at intermediate energies, and pair production dominates at high energies. Each photon interaction will be briefly explained

in the following sections with an emphasis on the Compton scattering and photoelectric absorption.

2.2.2 Rayleigh Scattering

Also known as coherent scattering, Rayleigh scattering occurs when an incident photon is elastically scattered by an atom. This interaction has no effect in terms of radiation dosimetry as the interaction is elastic and no energy is transferred from the photon to the atom, although the detection of these scattered photons will have a negative impact on diagnostic image quality. Fortunately, this interaction mainly occurs with very low energy photons and its impact is almost negligible in the diagnostic energy range.[110] For example, Rayleigh scattering accounts for only 0.8% of all photon interactions at a photon energy of 40 keV in soft tissue.[111] The Rayleigh mass attenuation coefficient $\frac{\sigma_R}{\rho}$ is proportional to the atomic number Z of the atom and inversely proportional to the square of the photon energy $h\nu$.

$$\frac{\sigma_R}{\rho} \propto \frac{Z}{(h\nu)^2} \qquad 2.12$$

2.2.3 Photoelectric Absorption

In photoelectric absorption, an incident photon's energy is completely absorbed by the atom and is subsequentially transferred to a tightly bound electron, typically belonging to an inner electron shell. This absorption is followed by the ejection of the electron, referred to as a photoelectron. The kinetic energy T of the photoelectron is equal to the difference of the incident photon energy $h\nu$ and the binding energy E_b of the electron.

$$T = h\nu - E_b \qquad 2.13$$

The ejection of the photoelectron produces a vacancy within an inner shell, which is immediately filled by an outer shell electron with a lower binding energy. This produces another vacancy, which is then filled by an electron with an even smaller binding energy. This cascading effect results in the emission of characteristics X-rays with energy equal to

the difference in binding energy between the higher and lower electron shells. Alternatively, the binding energy can be released as Auger electrons. As the atomic number of the absorber decreases, the probability of characteristic X-ray emission (fluorescent yield) is reduced.[110] A schematic of photoelectric absorption is given in Figure 2.2.

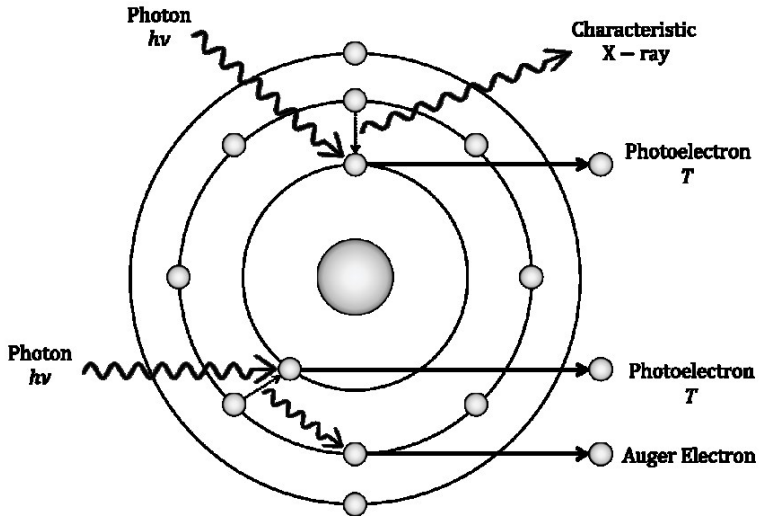

Figure 2.2: Photoelectric absorption schematic. An incident photon is absorbed by the atom resulting in the emission of a photoelectron. The vacancy is filled by an outer shell electron, which is accompanied by either the emission of a characteristic X-ray (top) or an Auger electron (bottom).

The mass attenuation coefficient for photoelectric absorption is approximately proportional to the cube of the atomic number and inversely proportional to the cube of the photon energy.

$$\frac{\tau}{\rho} \propto \left(\frac{Z}{h\nu}\right)^3 \qquad 2.14$$

Although the probability of photoelectric absorption generally decreases with increasing photon energy, there are notable exceptions. Sharp discontinuities (absorption edges) exist in the probability of photoelectric absorption that correspond to the electron binding energies. This differential absorption is exploited to provide improved CT image contrast when performing CT-based dosimetry in ^{90}Y TARE. For example, the mass attenuation coefficient for the photoelectric effect is shown in Figure 2.3 for soft tissue, a standard plate glass composition (sodium carbonate, calcium oxide, and silicon dioxide), and the

microsphere composition of an early microsphere formulation (silicon dioxide, strontium carbonate, gallium oxide, yttrium oxide).[111] The increased attenuation of the microspheres is due to photoelectric absorption of the photons by the higher atomic number elements within the microsphere composition.

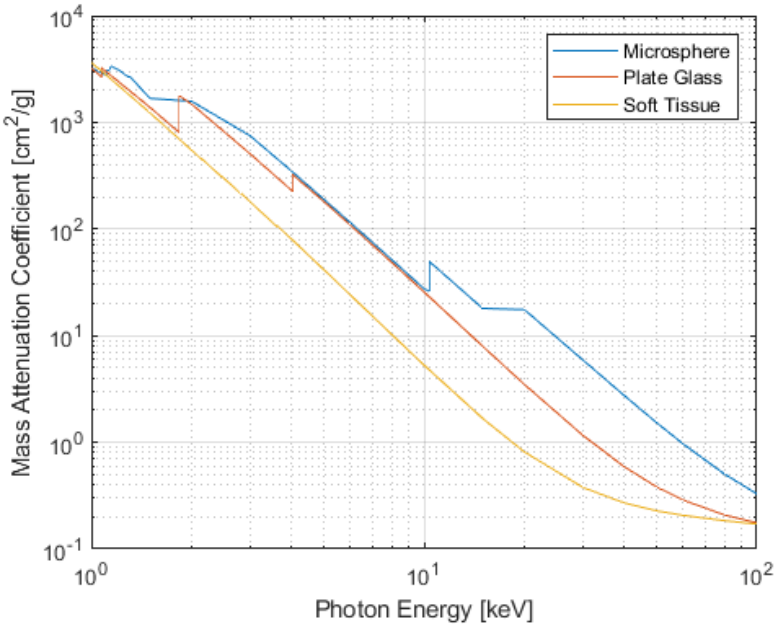

Figure 2.3: Mass attenuation coefficients for photoelectric absorption in soft tissue, plate glass, and an early microsphere formulation, as a function of photon energy.

2.2.4 Compton Scattering

Compton scattering is the dominant photon interaction in soft tissue with a broad energy range extending from ~20 keV to ~20 MeV, although this range gradually narrows with increasing atomic number.[110] In Compton scattering, a photon interacts with an unbound, stationary electron. Of course, electrons are electrostatically bound to a nucleus, but when photon energy is much greater than the electron binding energy ($E_b \ll h\nu$), the electron can be modeled as unbound and stationary.[110] As a result of the photon-electron interaction, the photon of energy $h\nu$ loses a fraction of energy to the electron, which is ejected with energy E from the atom with scattering angle ϕ. The photon is deflected by scattering angle θ with reduced energy $h\nu'$. The kinematics of Compton scattering are depicted in Figure 2.4.

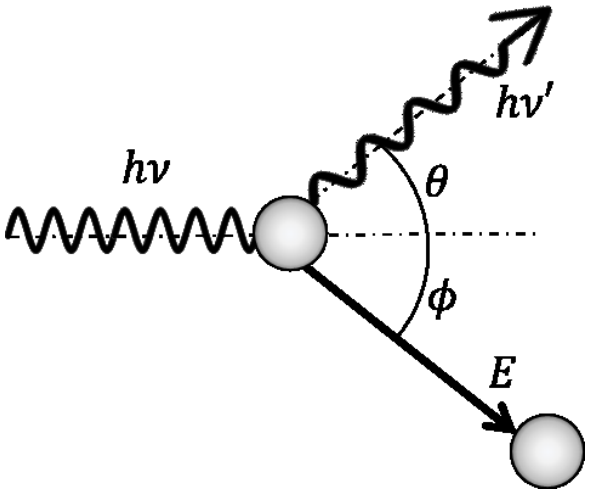

Figure 2.4: Kinematic geometry describing the photon-electron interaction in Compton scattering.

Through the application of conservation of energy and momentum laws, multiple kinematic relationships can be derived, such as the energy of the scattered photon $h\nu'$ as shown in Equation 2.15.

$$h\nu' = \frac{h\nu}{1 + \alpha(1 - cos\,\theta)} \tag{2.15}$$

The constant α is the photon energy normalized by the electron rest energy, ${}^{h\nu}/_{m_e c^2}$. Equation 2.16 shows the relationship between the scattered electron angle and photon angle.

$$cot\,\phi = (1 + \alpha)\,tan\frac{\theta}{2} \tag{2.16}$$

The scattered electron has kinetic energy given by Equation 2.17.

$$E = h\nu - h\nu' = h\nu\frac{\alpha(1 - \cos\theta)}{1 + \alpha(1 - \cos\theta)} \tag{2.17}$$

Equations 2.15, 2.16, and 2.17 describe the kinematics of the Compton scattering, but reveal nothing regarding the probability of interaction. The Klein–Nishina formula, jointly derived by Oskar Klein and Yoshio Nishina in 1928, gives the differential cross section for photons scattering at angle θ in a cone of differential area $d\Omega$.[112]

$$\frac{d\sigma_e}{d\Omega_\theta} = \frac{r_0^2}{2}\left(\frac{h\upsilon'}{h\upsilon}\right)^2\left(\frac{h\upsilon}{h\upsilon'} + \frac{h\upsilon'}{h\upsilon} - sin^2\,\theta\right) \qquad 2.18$$

Here, r_0 is the classical electron radius (2.818 x 10^{-15} m). The proportionality of the mass attenuation coefficient in Compton scattering is given in Equation 2.19.

$$\frac{\sigma}{\rho} \propto \frac{Z}{A}\sigma_e \qquad 2.19$$

Here, σ_e is the electron scattering cross section determined through integration of Equation 2.18 over all photon scattering angles. Given the approximately constant ratio of Z to A (outside of hydrogen), the mass attenuation coefficient for Compton scattering is independent of the atomic number of the scattering medium.[110]

2.2.5 Pair Production

In pair production, an incident photon interacts with the electromagnetic field of an atomic nucleus, giving up all its energy to spontaneously generate an electron-positron pair. The conversion of photon energy to mass requires the incident photon energy to exceed the rest mass of the electron-positron pair (1.022 MeV). The remaining photon energy is distributed as kinetic energy between the electron and positron, which is then transferred to the surrounding material through excitation and ionization events. As the positron comes to rest, it combines with a free electron in an annihilation event to produce two oppositely directed 511 keV photons. Because pair production occurs within the electromagnetic field

of a nucleus, the interaction probability is proportional to the atomic number, as shown in Equation 2.20.

$$\frac{\tau}{\rho} \propto Z \tag{2.20}$$

2.3 Charged Particle Interactions in Matter

The previous section reviewed mechanisms by which radiation interacts with matter and transfers energy to charged particles. These concepts are fundamental in understanding the function of the imaging modalities employed for dosimetry in this thesis, however, they do not describe the deposition of radiation energy in an absorbing medium. In this section, a description of charged particles interaction in matter is provided. It is through these interactions that radiation dose is deposited.

2.3.1 Stopping Power

Charged particles continuously interact with surrounding electrons and atomic nuclei through Coulombic interactions. This contrasts with photons, which can lose energy in a single, catastrophic interaction. The stopping power S is a parameter that describes a charged particle's differential energy loss dT per unit path length dx, typically expressed in units of MeV/cm.

$$S = \frac{dT}{dx} \tag{2.21}$$

Stopping power plays a critical role in dosimetry and is dependent on the characteristics of the charged particle (mass, charge, velocity) as well as the absorbing medium (density, atomic number). Dividing the stopping power by the physical density ρ gives the mass stopping power [MeV·cm^2/g], which can be further divided into the mass collision stopping power $\left(\frac{dT}{\rho dx}\right)_c$ and mass radiative stopping power $\left(\frac{dT}{d\rho x}\right)_r$.

2.3.2 Mass Collisional Stopping Power

Mass collisional stopping power, shown in Equation 2.22, results from charged particle interactions with orbital electrons.

$$\left(\frac{dT}{\rho dx}\right)_c = \left(\frac{dT_s}{\rho dx}\right)_c + \left(\frac{dT_h}{\rho dx}\right)_c \quad 2.22$$

Here, $\left(\frac{dT_s}{\rho dx}\right)_c$ and $\left(\frac{dT_h}{\rho dx}\right)_c$ are the stopping power terms resulting from soft and hard coulombic interactions, respectively, where hard and soft refer to the proximity of the charged particle to the atom.[110] The soft collision term in Equation 2.23 was originally derived by Bethe in 1930,

$$\left(\frac{dT_s}{\rho dx}\right)_c = k\left[ln\left(\frac{2m_0c^2\beta^2H}{I^2(1-\beta^2)}\right) - \beta^2\right], \quad 2.23$$

where

$$k = \frac{2Cm_0c^2z^2}{\beta^2} \quad 2.24$$

The constant C in Equation 2.24 is equal to $\pi r_0^2\left({}^{N_AZ}/_{A}\right)$, where ${}^{N_AZ}/_{A}$ is the number of electrons per gram of the medium, m_0 is the electron mass, N_A is Avogadro's constant, Z and A are the atomic and mass numbers, respectively. The parameter z is the charge of the incident charged particle, β is the ratio of the particle velocity to the speed of light c, I is the mean excitation potential of the atom, and H is an energy threshold value separating hard and soft collisions.

For electrons, the hard collision term is based on the Møller cross section.[113] The resulting stopping power formula governing both hard and soft collisions is given by Equation 2.25.

$$\left(\frac{dT}{\rho dx}\right)_c = k\left[ln\left(\frac{\tau^2(\tau+2)}{2(I/m_0c^2)^2}\right) + F^-(\tau) - \delta - \frac{2C}{Z}\right] \quad 2.25$$

Here, $\tau = T/m_0c^2$, δ is a correction term for electric dipole polarization, C/Z is an electron shell correction term, and $F^-(\tau)$ is a electron-specific function of energy.[110]

2.3.3 Mass Radiative Stopping Power

Mass radiative stopping power $\left(\frac{dT}{\rho dx}\right)_r$ results from interactions with atomic nuclei to produce bremsstrahlung radiation and is defined in Equation 2.26.

$$\left(\frac{dT}{\rho dx}\right)_r = \sigma_0 \frac{N_A Z^2}{A}(T + m_0c^2)\bar{B}_r \qquad 2.26$$

The constant σ_0 is equal to $\frac{1}{137}\left(\frac{e^2}{m_0c^2}\right)$ and B_r is a slowly varying function of Z and T.[113] The absorbed dose contribution from these radiative losses in soft tissue is estimated to be three orders of magnitude less than the electron dose contribution, and is therefore not considered clinically relevant in ^{90}Y TARE.[114] However, as previously mentioned, bremsstrahlung production is of fundamental importance for SPECT imaging of the ^{90}Y microsphere distribution. The total mass stopping power is the sum of the both the collision and radiative stopping power contributions.

$$\frac{dT}{\rho dx} = \left(\frac{dT}{\rho dx}\right)_c + \left(\frac{dT}{\rho dx}\right)_r \qquad 2.27$$

2.3.4 Absorbed Dose

The absorbed dose D to a medium is related to the mass collisional stopping power and the electron fluence Φ through Equation 2.28, under the conditions of negligible radiative stopping power and charged particle equilibrium (charged particle number entering a volume equals the charged particle number leaving the volume).[110]

$$D = \Phi \left(\frac{dT}{\rho dx}\right)_c \qquad 2.28$$

Equation 2.28 provides a conceptual understanding of how the absorbed radiation dose depends on the characteristics of the charged particle and the absorbing material through the collisional mass stopping power. In the following section, dosimetry formalisms implemented in this thesis are described.

2.4 Radiation Dosimetry

The absorbed radiation dose is defined as the radiation energy deposited in matter per unit mass. The SI unit of absorbed dose is the Gray [Gy], where 1 Gy = 1 J kg^{-1}. Radiation dosimetry is as the measurement of the absorbed radiation dose. This section reviews three approaches to radiation dosimetry implemented in this thesis.

2.4.1 Medical Internal Radiation Dose

The MIRD method described by Loevinger *et al*. assumes a homogeneous activity distribution within the target organ.[115] The general expression used by MIRD to calculate the absorbed dose in a target organ is described by Equation 2.29,

$$D(r_T) = \sum_S \tilde{A}(r_S) \cdot S(r_T \leftarrow r_S) \qquad 2.29$$

where D is the absorbed dose to a target organ r_T, $\tilde{A}$ is the cumulated activity in a source organ r_S, and S is the mean dose per cumulated activity deposited from the source organ to the target organ. The dose to the target organ is summed over contributions from all source organs.

In ^{90}Y TARE, microspheres remain fixed in the liver as permanent implants, hence the effective half-life for ^{90}Y is equal to its physical half-life. This feature in TARE greatly simplifies the dosimetry. The cumulated activity $\tilde{A}$ is given by Equation 2.30.

$$\tilde{A} = \int_0^\infty A(t)\, dt = \int_0^\infty A_0 e^{-\lambda t}\, dt = \tau A_0 \qquad 2.30$$

Here, A_0 is the administered activity and τ is the mean lifetime. The parameter S is defined in Equation 2.31,

$$S(r_T \leftarrow r_S) = \frac{\sum_i y_i E_i \phi_i(r_T \leftarrow r_S)}{m_{r_T}} \qquad 2.31$$

where y_i is the fraction of nuclear disintegrations emitted with energy E_i from a source organ, ϕ_i is the fraction of energy absorbed in the target organ, i is the number of nuclear disintegrations in the decay scheme of the radioisotope, m is the mass of the target organ. Values used for S have been previously calculated for various radioisotopes and standardized anthropomorphic phantoms.[116]

In ^{90}Y dosimetry, the absorbed dose is almost entirely due to the high-energy β^-, which deposits its energy locally. Therefore, the absorbed energy fraction ϕ in Equation 2.31 is unity. Furthermore, since there is one principal decay mode, the term $\sum_i y_i E_i$ in Equation 2.31 is equal to the average energy E_{avg} of the ^{90}Y β^- particle. This can be determined by integrating the product of the β^- energy E and the emission spectrum Ψ, as shown in Equation 2.32.

$$E_{avg} = \int_0^{E_{max}} E\, \Psi(E) dE \qquad 2.32$$

The ^{90}Y emission spectrum is provided in Figure 2.5.[117] The integral under the curve is equal to the branching ratio (~0.999) of the primary ^{90}Y decay pathway β_{00}^- displayed in Figure 1.3. The average energy E_{avg} of the spectrum is 0.927 MeV, or 1.485 x 10^{-13} J.

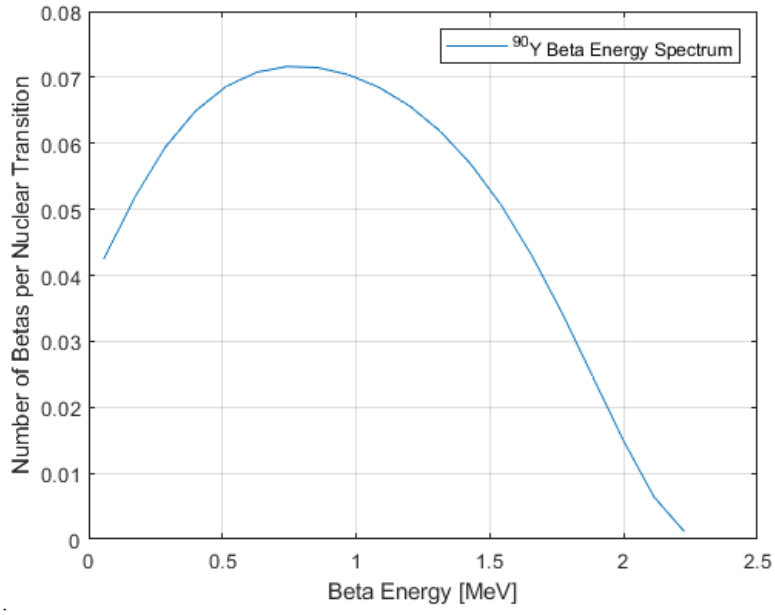

Figure 2.5: ^{90}Y emission spectrum.

Under the assumptions of ^{90}Y dosimetry ($S = {E_{avg}}/{m}$ and $\tilde{A} = \tau A_0$), the MIRD expression for the absorbed dose to a target volume can be simplified for ^{90}Y dosimetry, as shown in Equation 2.33.

$$D_{MIRD} = \frac{A_0 * 50}{M} \qquad 2.33$$

Here, A_0 is the administered ^{90}Y activity in GBq and M is the mass of the target in kg. A significant limitation in the MIRD method of dose calculation is the assumption of a uniform distribution of activity within a target volume, which has been shown to be false in ^{90}Y TARE as microspheres form highly heterogeneous patterns within the tumour.[54,91] Despite this limitation, the MIRD method is a widely implemented tool in the establishment of a reference dose in ^{90}Y TARE. If dose metrics other the average dose estimate are desired, more complex dosimetry formalisms must be implemented. These formalisms require an estimate of a voxelized ^{90}Y activity concentration, provided either by post-treatment SPECT or PET imaging.

2.4.2 Dose-Point Kernel Convolution

A more accurate approach in radionuclide dosimetry is dose-voxel kernel (DVK) convolution. A DVK describes the absorbed dose distribution around an activity source uniformly distributed within a single voxel. DVKs are computed using validated MC platforms which quantify the absorbed dose in surrounding, predefined voxel sizes per unit source of radionuclide activity.

Mathematically, convolution is an operation that acts on two functions f and g to produce a third function which describes the amount of overlap of f as it is shifted over g. A 3D discrete convolution between f and g is given in Equation 2.34.

$$(f * g)(x, y, z) = \sum_{x'} \sum_{y'} \sum_{z'} f(x', y', z') \cdot g(x - x', y - y', z - z') \qquad 2.34$$

For radionuclide dosimetry, the absorbed dose D can be determined from a discrete convolution of a DVK and a radionuclide cumulated activity distribution $\tilde{A}$.

$$D(x, y, z) = \left(\tilde{A} * DVK\right)(x, y, z) \qquad 2.35$$

The convolution of $\tilde{A}$ and DVK may be performed in the frequency domain using the fast Fourier transform to decrease the computational burden. Convolution is the most widely used dosimetry method in ^{90}Y TARE with clinical implementation available through multiple software platforms, including PLANET® Dose (DOSIsoft, Cachan, France) Velocity Rapidsphere (Varian Medical Systems Inc., Palo Alto, CA, USA), and MIM SurePlan™ LiverY90 (MIM Software Inc., Cleveland, OH, USA).[100]

2.4.3 Monte Carlo

MC methods, referencing the stochastic nature of the Monte Carlo casino in the principality of Monaco, use random numbers to sample probability distributions governing radiation interactions in matter to accurately simulate radiation transport.[118] In this thesis, MC methods are applied to 1) calculate a range of DVKs for convolutional dosimetry and

2) to a compute highly accurate ground truth dose distribution based on a quantitative map of cumulated ^{90}Y activity. Specific parameters for the MC simulations in DVK calculations are provided in Section 4.4.6 and Section 5.4.5.3. For the ground truth dose distribution, MC parameters are provided in Section 4.4.5. MC dosimetry in ^{90}Y TARE is not performed clinically as its primary advantage is lost since the liver is one of the most homogeneous organs in the human body. Furthermore, MC methods are known to suffer from long computational times as millions of particles must be simulated to achieve a satisfactory statistical uncertainty, posing an additional barrier to clinical implementation.

2.5 Computed Tomography

The first viable CT scanner was invented by Sir Godfrey Hounsfield in 1971, who later received a Nobel prize for his contributions to the field of medicine. At the time of this writing, CT is 50 years old.[119] During the past half-century, CT has rapidly developed as an invaluable tool in diagnostic radiology with an estimated half million patients in the United States benefiting from CT examinations every day.[120] This section details the underlying CT principles of image formation, instrumentation, image quality, and image reconstruction.

2.5.1 Principles

The process of CT image formation requires the measurement of X-ray attenuation profiles over many source angles following their transmission through an absorbing medium.[121] The attenuation profile at a given X-ray source angle is called a projection, which is composed of attenuation values along individual ray paths. The attenuation value of a given ray is representative of the line integral of linear attenuation coefficients. Measured projections are used in CT image reconstruction to produce a voxelized distribution of linear attenuation coefficients. As the X-rays pass through the medium, a given voxel will attenuate the photons based on the composition of the material in that voxel. For example, for a patient of thickness d, the intensity of an attenuated X-ray beam is given in Equation 2.36.

$$I(x) = I_o e^{-\int_0^d \mu(x)dx} \tag{2.36}$$

Given the intensities of the attenuated and unattenuated beams, $I(x)$ and I_o, respectively, image reconstruction techniques can recover the linear attenuation coefficient distribution.

Image data in CT is expressed in terms of Hounsfield units (HU), where the HU scale is a measure of a voxel's linear attenuation coefficient μ relative to water μ_{H20}.

$$HU = 1000 \cdot \frac{\mu - \mu_{H20}}{\mu_{H20}} \qquad 2.37$$

By definition, Equation 2.37 illustrates that water and air have a HU of 0 and -1000, respectively. A HU of 1 is associated with a change of 0.1% in μ relative to μ_{H20}. Since the linear attenuation coefficient is a nonlinear function of photon energy, all substances (except air and water) will have variations in HU when measured using different tube potentials.

2.5.2 Instrumentation

Essential components of a CT scanner include the gantry, table, X-ray tube, collimator, and detector.[121] The X-ray tube responsible for the generation of the incident photon beam is housed within a rotating gantry system, allowing for X-ray projections to be recorded at many angles (typically more than 1000). Within the evacuated X-ray tube, electrons are accelerated from a cathode by a high potential (80-140 kVp) into a solid target (anode) where they decelerate to produce X-rays in the form of bremsstrahlung radiation. However only ~1% of energy incident on the target is converted to X-rays – the rest is deposited as heat.[121] Therefore, the target is rotated within the X-ray tube to distribute the heat over a larger area. The target is composed of tungsten for its high melting point (3,370 ℃) as well as its high atomic number (Z = 74), which is essential for efficient bremsstrahlung production.[121]

The X-rays emitted from the target are collimated within the gantry to produce the desired beam dimensions. In clinical CT, the beam width in the longitudinal dimension is typically small (~mm), hence this type of collimation is referred to as fan beam CT (FBCT). Prior to collimation, X-ray filtration removes low-energy X-rays that contribute only to superficial patient dose. Furthermore, the 'bowtie' shape of these filters preferentially

attenuates the beam to compensate for the nonuniform attenuation of the X-rays by the patient.

In helical CT scanning, the table moves at a constant speed through the gantry. This is opposed axial scanning where a step-and-shoot approach is implemented. Helical scanning provides the advantage of speed by eliminating the start/stop motions of the table and is therefore more convenient for clinical workflow. However, axial scanning provides better resolution in the longitudinal dimension as it does not depend on data interpolation, which is required in helical scanning.[121] In helical CT, the ratio of table translation per 360° to the nominal collimated beam width is referred to as the pitch factor. A pitch factor value < 1 indicates oversampling while a pitch factor > 1 indicates undersampling.

Radiation detectors in modern CT scanners use solid-state devices composed of a scintillator coupled to a photodiode. The scintillator crystal generates visible light following the absorption of incident X-rays. The surface of the scintillator crystal is sintered (scored with a saw or laser) to improve detection efficiency, then coupled with a photodiode to convert the visible light to an electrical signal. The scintillator coupled to a photodiode forms a single detector module. An array of these modules is mounted on a curved frame on the rotating CT gantry.

2.5.3 Image Reconstruction

The problem to be solved in CT image reconstruction is to recover the distribution of linear attenuation coefficients $\mu(x, y)$ from measured projections. Each ray in the projection data represents a line integral of the linear attenuation coefficients. The projection of an object at position s and projection angle θ is given in Equation 2.38.

$$p(s,\theta) = ln\left(\frac{N_0}{N}\right) = \int_{-\infty}^{+\infty}\int_{-\infty}^{+\infty} \mu(x,y)\,\delta(x\,\cos\theta + y\,\sin\theta - s)\,dx\,dy \qquad 2.38$$

Here, δ is the Dirac delta function and N_0 and N are the number of unattenuated and attenuated photons measured by the detector. The calculation of a series of projections over

multiple angles θ is referred to as a Radon transform, and provides the mathematical basis for tomographic image reconstruction.[122] An illustration of the Radon transform is provided in Figure 2.6. An axial slice of the Shepp-Logan phantom, overlaid with standard and rotated (45°) cartesian coordinate systems, is shown in Figure 2.6(a).[123] The projection of the image as described by Equation 2.38 is provided in Figure 2.6(b) for an angle θ = 45°. The Radon transform of the object (referred to as a sinogram) is shown in Figure 2.6(c), with the projection in Figure 2.6(b) represented as a single horizontal red line in the sinogram.

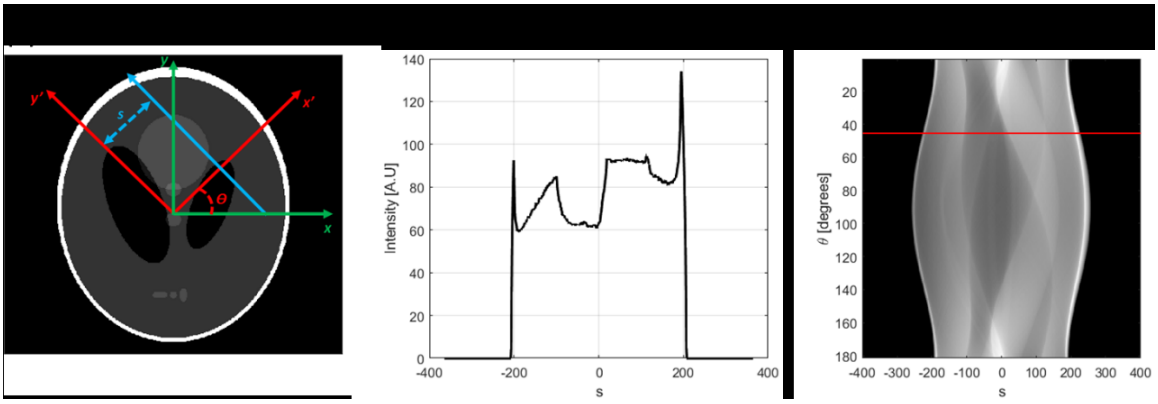

Figure 2.6: (a) An axial slice of the Shepp-Logan phantom. (b) Projection integral of (a) at angle θ. (c) Radon transform of (a).

Performing a Fourier transform of $\mu(x, y)$ provides a means to derive a fundamental theorem essential in tomographic image reconstruction. Let the Fourier transform of $\mu(x, y)$ be $U(u, v)$.

$$U(u, v) = \int_{-\infty}^{+\infty} \int_{-\infty}^{+\infty} \mu(x, y)\ e^{-2\pi i(ux+vy)}\, dx\, dy \qquad 2.39$$

Here, u and v are the corresponding quantities of x and y in Fourier space. Transforming to a polar coordinate system ($u = r\cos\theta$ and $v = r\sin\theta$) and applying the sifting property of the delta function, we arrive at Equation 2.40.

$$U(r, \theta) = \int_{-\infty}^{+\infty} \int_{-\infty}^{+\infty} \mu(x, y)\ e^{-2\pi irs}\, \delta(x\cos\theta + y\sin\theta - s)\, ds\, dx\, dy \qquad 2.40$$

Inserting Equation 2.38 into Equation 2.40, we arrive at Equation 2.41.

$$U(r,\theta) = \int_{-\infty}^{+\infty} p(s,\theta)\, e^{-2\pi i r s}\, ds \qquad 2.41$$

Equation 2.41 is the Fourier transform of the Radon transform. This relationship is known as the Fourier slice theorem and is summarized in Equations 2.42 and 2.43.

$$U(r,\theta) = \mathcal{F}[p(s,\theta)] \qquad 2.42$$

$$p(s,\theta) = \mathcal{F}^{-}[U(r,\theta)] \qquad 2.43$$

Here, $\mathcal{F}$ and $\mathcal{F}^{-}$ are the Fourier transform and inverse Fourier transform, respectively. The Fourier slice theorem states the following two calculations are mathematically equivalent:

1. 1D Fourier transform of a projection $p(s,\theta)$ at angle θ
2. Polar line at angle θ in 2D Fourier transform of $\mu(x,y)$

The Fourier slice theorem provides the basis for the most commonly used reconstruction algorithm, filtered backprojection (FBP).[121] In FBP, the Fourier slice theorem is used in concert with frequency filtering and backprojection. Backprojection can be through of as a "smearing" of the linear attenuation coefficient across the reconstructed image space at a specific angle θ. It is defined in Equation 2.44 given a projection $p(s,\theta)$

$$\mu(x,y) = \int_{0}^{\pi} d\theta \int_{-\infty}^{+\infty} p(s,\theta)\ \delta(x\cos\theta + y\sin\theta - s)\, ds \qquad 2.44$$

Invoking the Fourier slice theorem and applying the delta function sifting property, Equation 2.44 becomes

$$\mu(x,y) = \int_0^{\pi} d\theta \int_{-\infty}^{+\infty} \int_0^{+\infty} U(r,\theta)\ e^{-2\pi i r(x\cos\theta + y\sin\theta)}\, dr \qquad 2.45$$

The direct application of Equation 2.45 in image reconstructions results in a blurry version of the true object, regardless of the number of projections used in reconstruction. This issue may be mitigated with the addition of a ramp filter $|r|$.

$$\mu(x,y) = \int_0^{\pi} d\theta \int_0^{+\infty} U(r,\theta)\, e^{-2\pi i r(x\cos\theta + y\sin\theta)}\, |r|\, dr \qquad 2.46$$

To summarize, the FBP steps implicit in Equation 2.46 are as follows:

1. Log normalize image projection data
2. Take Fourier transform of (1)
3. Filter (2) in Fourier space
4. Take inverse Fourier transform of (3)
5. Back project (4) over all projection angles

Although the ramp filter, or Ram-Lak filter, compensates for the 1/r resolution loss in FBP, it also amplifies any high frequency noise.[121] To suppress this noise in the reconstructed image, the ramp filter can be apodized as in the Shepp-Logan, Hamming, Cosine, Hann filters. Examples of these filters are given as a function of spatial frequency k in Figure 2.7.

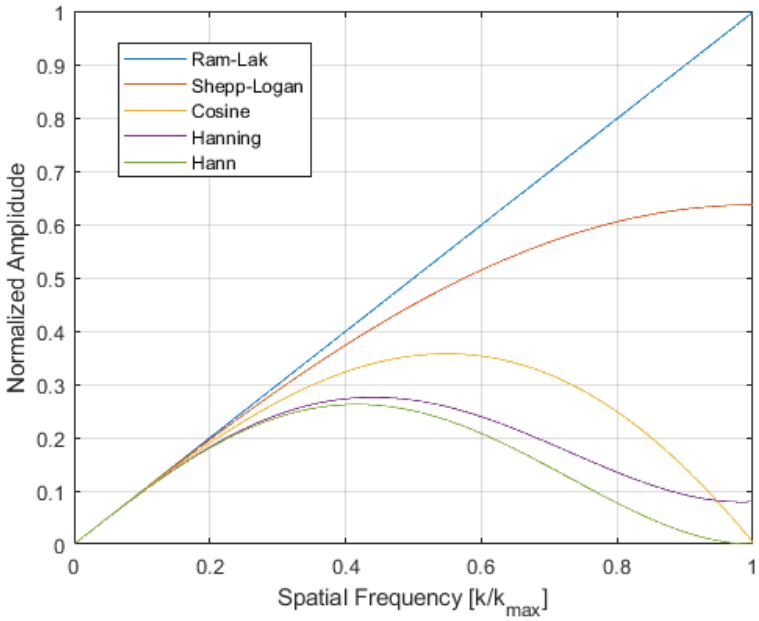

Figure 2.7: Ram-Lak, Shepp-Logan, Cosine, Hanning, and Hann filters used in FBP.

The choice of image reconstruction filter generally depends on the anatomy to be imaged. For example, when looking for small, discrete fractures in bone, kernels without significant roll off at high frequencies should be implemented in image reconstruction to maintain sufficient detail and accentuate these fine features. Conversely, when looking for low contrast changes in uniform regions, such as the liver, a softer, noise-reducing kernel might be desirable. In either case, there are unavoidable tradeoffs between contrast resolution and spatial resolution. In ^{90}Y TARE, embolized vasculature can present as low image contrast in diffuse, macroscopic regions, and also as high image contrast for fully embolized microvasculature. Hence, the choice of reconstruction filter in CT image reconstruction will consequently impact the evaluation and quantification of the ^{90}Y activity distribution.

2.5.4 Image Quality

The quality of the reconstructed CT images is characterized by spatial and contrast resolution. Contrast resolution describes the degree to which structures with comparable image intensity can be distinguished from one another.[121] Statistical noise in the image is a significant limitation for low contrast resolution, but a number of strategies can be employed to address this limitation. Noise may be reduced by increasing the photon flux

through an increase in tube current or in tube potential, at the cost of increasing the patient radiation dose. X-ray tube output is approximately linear in tube current and approximately proportional to the square of the tube potential. Alternatively, image noise may be reduced by increasing the reconstructed slice thickness to allow more photons to contribute to the signal-to-noise ratio (SNR), or by using an apodized filter during image reconstruction.

The spatial resolution of an imaging modality describes its ability to distinguish two small, adjacent objects.[121] The strength of CT as an imaging modality lies in its excellent spatial resolution. Spatial resolution is measured by the FWHM of a point spread function (PSF) in the transverse plane and by a slice sensitivity profile (SSP) in the longitudinal plane. Physical factors affecting spatial resolution in CT are the X-ray focal spot size, detector size and density, and pitch. Nonphysical parameters related to image reconstruction the impact spatial resolution include the reconstructed field-of-view (FOV), slice thickness, and image reconstruction kernel.

2.6 Positron Emission Tomography

PET is an imaging modality employed in nuclear medicine that is capable of depicting *in vivo* distributions of positron-emitting radionuclides. In ^{90}Y TARE, positron production is due to internal pair production in the ^{90}Y decay scheme.[83] Unlike Floruine-18 (^{18}F), the most widely utilized radioisotope in PET imaging, ^{90}Y emits a positron only 32 per million decays compared to 967 per thousand decays for ^{18}F. The extremely low probability of positron emission in ^{90}Y poses challenging in ^{90}Y PET imaging. This section describes fundamental concepts in PET, with an emphasis on ^{90}Y PET imaging.

2.6.1 Principles

After a positron is generated in the decay of a radionuclide (β^+ decay, pair production, or internal pair production, e.g.), it gradually loses kinetic energy through coulombic interactions (ionization and excitation) with the surrounding charged particles. When the positron comes to rest and combines with an electron in an annihilation event, two 511 keV photons are produced. Conservation of momentum requires that the photons are emitted approximately 180° apart. If the annihilation event is surrounded by a ring of suitable detectors, the annihilation photon pairs can be detected based on their arrival time

at two opposing detectors to form a line-of-response (LOR) between the detectors. This mode of coincidence detection provides a means to record angular projections of the activity distribution which can be used to for image reconstruction (Section 2.4.3). A schematic describing an annihilation event and detection is provided in Figure 2.8.

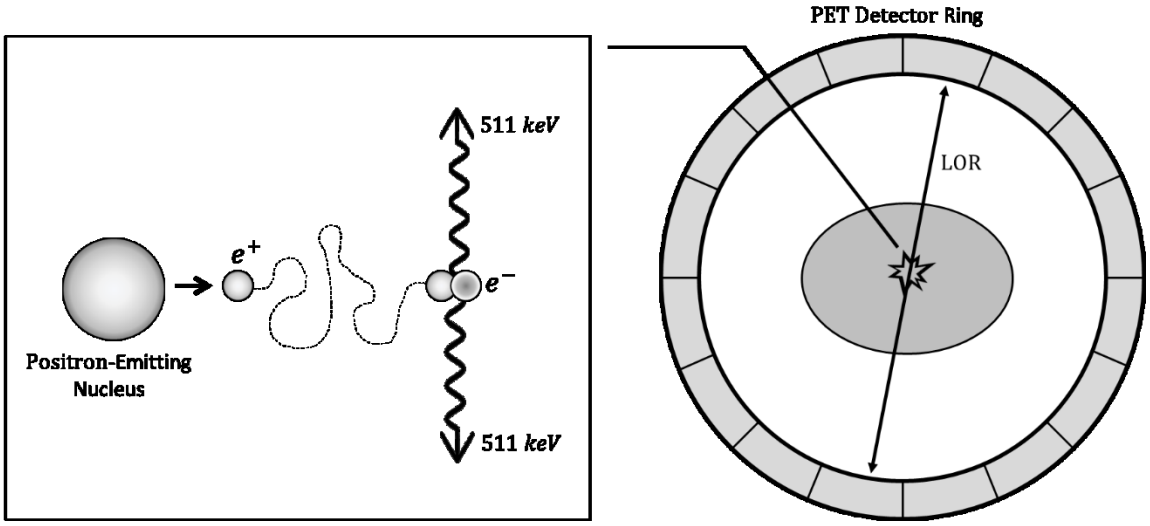

Figure 2.8: Schematic of an electron-positron annihilation event occurring within a patient inside of a PET detector ring.

2.6.2 Instrumentation

Most current clinical PET systems rely on scintillation detectors. Desirable scintillator properties in PET include a high light output, short signal decay time, high intrinsic energy resolution, and high stopping power for 511 keV photons. Many scintillator materials have been implemented in PET detectors, including thallium-doped sodium iodide (NaI[Tl]), bismuth germanate (BGO), and cerium-doped lutetium oxyorthosilicate (LSO[Ce]).[124] Modern PET scanners use lutetium-based compounds for the scintillator due to the high density and excellent temporal resolution.[87] The visible light generated by a sintered scintillator crystal is detected and measured using a coupled photodetector, either a photomultiplier tube (PMT) or a semiconductor-based photodiode.

In a PMT, incident photons deposit energy in a photocathode to trigger the ejection of photoelectrons into an evacuated chamber. Under an applied electric potential, electrons are accelerated through a series of dynodes to produce a cascade of secondary electrons, all contributing to the final signal. PMTs provide signal gains of a million or more,

providing excellent SNR for low levels of visible light.[124] Its drawback is in poor efficiency in photoelectron emission following the absorption of a scintillation photon. Although used less frequently, photodiodes provide improved detection efficiency owing to their high density. This improvement comes at the cost of SNR due to thermally activated charge flow and poor signal amplification.

Individual scintillation crystals are not usually coupled directly to a single PMT due to cost and space constraints. The most common scintillator-PMT arrangement is referred to as a block detector in which a group of scintillator crystals share multiple PMTs. The spatial location of the annihilation event can be determined from the output of multiple PMTs using a weighted centroid algorithm.[124] Block detectors form the structural unit in PET scanners. The leading PET detector design consists of several rings of detectors that surround the patient in the longitudinal dimension. Although this design offers complete angular coverage, the longitudinal coverage is limited (~20 cm), often necessitating multiple couch shifts to fully image the region of interest.[124] The presence of multiple detector rings raises challenges in the determination of detector combinations used to measure coincidence events, but offers a substantial increase in detection sensitivity (~5x).[124] In a 2D PET acquisition mode, tungsten septa are inserted between adjacent rings to absorb photons incident at oblique angles relative to the transverse plane. In 3D mode, these septa are retracted.

An electrical pulse is generated from the detector in response to an incident photon. If the pulse height is sufficiently large (proportional to energy of photon), a timestamped pulse with width τ is compared with other detector signals. A prompt coincidence is registered if there is an overlap in the pulse length between detectors. Prompt coincidences are divided into true, random, and scatter coincidences. A true coincidence is the detection of a pair of annihilation quanta originating from the same annihilation event. Only true coincidences contribute useful information in PET. Random coincidences occur when annihilation quanta from different events are detected within the same coincidence window. Scatter coincidences occur when one or both photons are scattered and still detected within the same window. Both random and scatter coincidences assign activity to

LORs that do not intersect the true location of an annihilation event. Therefore, random and scatter coincidences need to be corrected for PET imaging to be fully quantitative.

2.6.3 Image Reconstruction

Before raw PET image data can be considered quantitative, corrections must be made to account for the degrading effects attenuation within the patient, scattered and random coincidences, detector inhomogeneity, and dead time.[124]

In ^{90}Y PET, random coincidences make a large contribution (80%) to all measured coincidence events, and if left uncorrected, will significantly reduce image contrast and quantitative accuracy.[125] For quantitative PET imaging, random coincidences must be estimated and subtracted from the total number of coincidence events in each LOR. A widely adopted and accurate approach, one that is also employed in this work, is delayed event subtraction.[126] In this approach, a duplicate channel records detector signals intentionally delayed by a time $t \gg \tau$. By introducing this delay, true coincidences arising from actual annihilations will be removed and remaining coincidences provide an estimate for the random coincidences.

The most significant correction in PET is for photon attenuation. Consider an annihilation event at position x within a patient of thickness T. For a coincidence to occur, both photons must be detected. The probability P_{det} both photons reach the detectors is given by Equation 2.47.

$$P_{det} = e^{-\mu x} \cdot e^{-\mu(T-x)} = e^{-\mu T} \qquad 2.47$$

The linear attenuation coefficient for soft tissue at 511 keV is $\mu = 0.095$ cm^{-1}. Note that Equation 2.47 indicates the probability of photon attenuation is independent of the source position x, therefore the attenuation correction requires the determination of attenuation probability for a source along each LOR. This can be determined through the comparison of a 511 keV transmission source scan through a patient (transmission scan) to an unattenuated scan with the patient absent (blank scan). Although this method is quantitatively accurate with a 511 keV source, it suffers from noise and long scan times during which patient motion may reduce the accuracy of this approach.[124] The introduction

of combined PET/CT systems provided a significantly faster means for attenuation correction with the added benefit of improved spatial resolution imaging. However, linear attenuation coefficients do not scale linearly from low energy X-rays used in CT to high energy annihilation photons (511 keV). This necessitates a scaling process to adjust the linear attenuation coefficients for the appropriate photon energy.[124] Potential problems arise with a CT-based attenuation correction. Patient motion between the PET and CT scans will result in image mis-registration, leading to incorrect attenuation correction factors, as well as the inaccurate projection of ^{90}Y activity onto the patient's anatomy.

Scattered photons, if uncorrected for, will reduce image contrast and degrade quantitative accuracy. Corrections for scatter coincidences range from empirical approaches, advanced energy window methods, deconvolution, and model-based methods.[126] In this thesis, a model-based scatter correction was applied. These methods make use of Compton scattering to model the distribution of coincidence events in which a photon experienced a single scattering event. Although multiple implementations of model-based corrections exist, all rely on the Klein–Nishina formula to calculate the probability that a scattered photon will be detected by a particular detector.[127–129]

Other corrections are required for detector dead time and detector normalization. A quantitatively accurate PET image requires the count rate to increase linearly with the activity inside the FOV. This condition can be violated due to the limited temporal resolution of the detector, particularly at high count rates, resulting in a count loss referred to as dead time.[126]

The Fourier-based image reconstruction techniques described in Section 2.4.3 assume each LOR has identical sensitivity in the detection of 511 keV photons. However, this is an invalid assumption for experimentally acquired data due to variations in detector efficiency and geometry. The process of correcting for these differences is called normalization and can be achieved through a uniform exposure of all detector elements to a 511 keV source and calculating a detector-specific calibration factor.

Once PET data corrections have been applied, the number of counts along a LOR is proportional to the line integral of activity along the LOR and the same Fourier-based image reconstruction techniques described in Section 2.4.3 can be applied to reconstruct

an activity distribution. However, in clinical PET, iterative reconstruction algorithms are the standard in image reconstruction, as opposed to FBP in CT image reconstruction.[130] A prominent iterative reconstruction algorithm in PET is the expectation maximization (EM) algorithm that computes the maximum likelihood (ML) of a voxel belonging to an activity distribution by assigning a greater weight to high count regions of a projection profile and lower weight to count deficient regions. This statistical weighting algorithm is often referred to as ML-EM. Due to the iterative nature of ML-EM, image reconstruction is computationally intensive and requires extended time relative to FBP. A method to reduce algorithm calculation time is called ordered subsets (OS). In this method, a subset of projections is used in the initial iterations of the algorithm. More projections are included as the image gets refined during the iterative process. When ML-EM incorporates OS, it is called OS-EM. This is the algorithm used in PET image reconstruction in this thesis.

Following image reconstruction, raw data is stored with units of counts per voxel per second. To convert these values to absolute activity concentration, typically Bq/mL, requires the application of a calibration factor CF.

$$CF = \frac{A\,p}{V\,C} \qquad 2.48$$

Here, A is the known activity within the fixed volume V, C is the raw voxel data in counts per voxel per second, and p is the branching ratio for positron production in the radionuclide decay scheme. This is determined experimentally through PET imaging of a phantom uniformly filled with a known activity concentration. The measurement of CF is known to be a major source of uncertainty in dosimetry.[131] The accuracy of CF depends on how well the activity concentration $\frac{A}{V}$ is known. This measurement is made with a dose calibrator traceable to a primary standard laboratory. Although standards exist for the measurement of ^{90}Y activity, there is no traceability to a primary standard for ^{90}Y microspheres in TARE.[132] The CF accuracy also relies on p, currently estimated at 31.86 $\pm$ 0.47 x 10^{-6} with a uncertainty of approximately 1.5%.[83]

2.6.4 Image Quality

As in CT, image quality in PET is characterized by both spatial and contrast resolution. The spatial resolution is typically defined by the FWHM of the PSF of a small activity source in the reconstructed image.[124] Measuring the spatial resolution in PET is performed by imaging a point source in air and reconstructing the image through FBP with reconstructed pixel size set to less than 1/3 of the expected FWHM of the PSF in all dimensions. This provides a best-case comparison between PET scanners despite the nonrealistic clinical conditions. In PET, the spatial resolution is fundamentally limited by the positron range and annihilation photon non-collinearity, as well as the intrinsic resolution of the scintillator crystal and parameters specific to image reconstruction algorithms. Spatial resolution (as measured by the FWHM) in ^{90}Y PET has been shown to range from 5.0 to 10.0 mm.[9,11]

Image contrast in PET is typically measured using contrast recovery coefficients (CRCs) derived from phantom imaging studies using radioactive spheres in a non-radioactive background. Although CRCs are generally near unity for large volumes, image noise can significantly reduce CRCs.[124] Specifically, in ^{90}Y PET imaging, the low positron fraction (~32 ppm) results in an inherently low SNR. Additionally, bremsstrahlung production in ^{90}Y PET results in very high random coincidences, further contributing to image noise.[88]

2.7 Summary

To summarize, this chapter provides a foundational background for the theoretical and methodological tools employed in the remainder of this thesis. Specifically, the concept radioactivity was introduced as it pertains to the decay of ^{90}Y. Photon attenuation and radiation interactions in matter were discussed as a prerequisite for the discussion of the underlying principles in PET and CT imaging of ^{90}Y. An introduction to charged particle interactions in matter provided the basis for radiation dosimetry and was followed by a description the various dosimetric approaches employed in ^{90}Y dosimetry. Together, these concepts are essential in the interpretation of the remainder of this thesis.

Chapter 3 Manuscript 1: Quantification of the Inherent Radiopacity of Glass Microspheres for Precision Dosimetry in Yttrium-90 Radioembolization

3.1 Prologue

In this manuscript, a methodology is proposed to quantify the inherent radiopacity of novel glass microspheres for the development of calibration curves to relate microsphere concentration within a CT voxel to corresponding HU enhancement for that voxel. This relationship was investigated through clinical CT imaging of microsphere distributions in liver tissue-equivalent phantoms. This work showed that HU and microsphere concentration are positively correlated over a range of CT acquisition parameters and demonstrated the potential of CT to quantify the infusion of microspheres for more accurate dosimetry in ^{90}Y TARE.

This manuscript was published in *Biomedical Physics & Engineering Express.* The reference is provided below.

- Henry, C., Mawko, G., Tonkopi, E., Frampton, J., Kehoe, S., Boyd, D., Abraham, R., Gregoire, M., O'Connell, K., Kappadath, S., Syme, A. (2019). Quantification of the Inherent Radiopacity of Glass Microspheres for Precision Dosimetry in Yttrium-90 Radioembolization. *Biomedical Physics & Engineering Express*, 5, 055011.

3.2 Abstract

Purpose: To develop a methodology to quantify the inherent radiopacity of radiopaque microspheres through CT imaging of liver tissue-equivalent phantoms, and to produce a calibration curve that relates microsphere concentration within a CT voxel to the corresponding HU of the voxel.

Methods: The radiopaque microspheres under investigation were composed of a proprietary blend of yttrium-strontium-gallium-silicate oxide glass similar in size and density to TheraSphere microspheres. Tissue-equivalent phantoms were designed to determine CT voxel enhancement from microspheres uniformly distributed within the

phantoms. Phantoms were imaged with CT to determine the average HU and with brightfield microscopy to determine the corresponding microsphere concentrations.

Results: HU and microsphere concentration are positively correlated ($r^2 = 0.949$) over a range of CT acquisition parameters. Calibration curve slopes range from 1.68 to 2.36 HU per microsphere per CT voxel. Minimum detectable limits are between 22 and 31 microspheres per CT voxel.

Conclusion: CT has the potential to quantify the radiation dose from the infusion of microspheres for more accurate dosimetry in TARE when used in conjunction with proper dosimetry software. This finding may improve our understanding of the relationship between absorbed dose and tumour response, which could ultimately translate into improved patient outcomes. Optimization of the prototype microsphere composition to maximize its inherent radiopacity will be an important step in realizing this goal.

3.3 Introduction

HCC, the most common subtype of primary liver cancer, is the sixth most common cancer in the world and is responsible for 8.3% of all cancer deaths worldwide.[12] The liver is also the most common site for metastatic tumors.[48] These metastases originate from a range of primary tumours, most commonly from colorectal, neuroendocrine, and breast tumours.[133] In fact, most patients with cancers originating in structures with venous drainage via the portal vein will show evidence of metastatic liver disease at the time of death.[134] Whether primary or metastatic in origin, liver tumours can be treated through several different mechanisms. While surgical resection or transplantation is considered to be the optimal treatment, the majority of liver cancer patients do not meet the criteria for this procedure.[20] Alternative treatments include chemotherapy, SBRT, ablation, and embolization. TARE is an established treatment modality for nonresectable, hypervascular liver cancer where ^{90}Y glass or resin microspheres are administered through the arterial vasculature of the liver to selectively target liver tumours while sparing healthy liver parenchyma. Microsphere infusion in the tumour microvasculature is possible due to the liver's unique blood supply – liver tumours derive at least 80% of their blood supply from

the hepatic artery while healthy liver parenchyma derives its blood supply primarily from the portal vein.[31]

^{90}Y is a pure β^- emitter that decays to stable ^{90}Zr through β^- decay with a physical half-life of 64.24 ± 0.30 hours.[58] The maximum and mean β^- emission energies are 2.2787 ± 0.0013 MeV and 0.9267 ± 0.0008 MeV, respectively. These energies correspond to a maximum and mean β^- range of 11 mm and 2.4 mm in water.[59,60] Due to the localized energy deposition of ^{90}Y, knowledge of the microsphere spatial distribution within the tumour is essential for accurate dosimetry. For a patient-specific measure of the absorbed tumour dose, voxelized SPECT and PET activity data can provide reasonable estimates of the mean tumour dose.[45,86,135] However, SPECT and PET can be associated with substantial uncertainties when quantifying the absorbed dose. This can be attributed to reconstruction techniques and partial volume effects resulting from the large voxel sizes of these imaging modalities.[136,137] These large voxel sizes, which are several times larger than the average range of β^- particles emitted by ^{90}Y, can mask variations in the true dose distribution and prevent accurate quantification of the absorbed dose. Consequently, there is an unmet clinical need to provide improved spatial resolution of the absorbed dose distribution in TARE. The superior spatial resolution of X-ray imaging modalities has the potential to address this clinical need.

Commercially available microspheres used in TARE include the glass-based TheraSphere® (Boston Scientific Corp., Marlborough, MA, USA) and the resin-based SIR-Spheres® (Sirtex Medical Inc., Woburn, MA, USA). A novel glass microsphere is currently under development by ABK Biomedical (Halifax, NS, Canada) with radiopaque properties that enable visualization using high-resolution X-ray imaging modalities, such as fluoroscopy or CT. Acquisition of CT images for microsphere distribution evaluation could provide the desired clinical improvement in dosimetry calculations.

In vivo validation of the radiopacity of these microspheres has been performed in the kidney of a hybrid farm pig with microsphere administrations intended to approximate human clinical treatment deliveries. After sacrifice, the kidney was explanted and imaged with a variety of X-ray imaging modalities, including clinical FBCT (SOMATOM Definition AS+, Siemens Healthcare Ltd, Erlangen, Germany), CBCT (AXIOM-Artis, Siemens Healthcare Ltd, Erlangen, Germany), micro-CT (Triumph X-O, Gamma Medica-

Ideas Inc., Los Angeles, CA, USA), and mammography (Selenia Dimensions, Hologic Inc., Marlborough, MA, USA). Figure 3.1(a-c) shows digitally reconstructed radiographs (DRRs) of the explanted kidney from all three CT imaging modalities. Figure 3.1(d) shows a mammography image of a single 3 mm thick axial slice of the kidney that was removed from a region immediately inferior to the hilum. All CT images were acquired with a tube potential of 80 kVp and are displayed with a window level of 40 HU and window width of 350 HU. The mammography image was acquired through magnification imaging with a tube potential of 25 kVp. The images are not quantitatively evaluated in this study and are simply intended to demonstrate that these microspheres are in fact radiopaque.

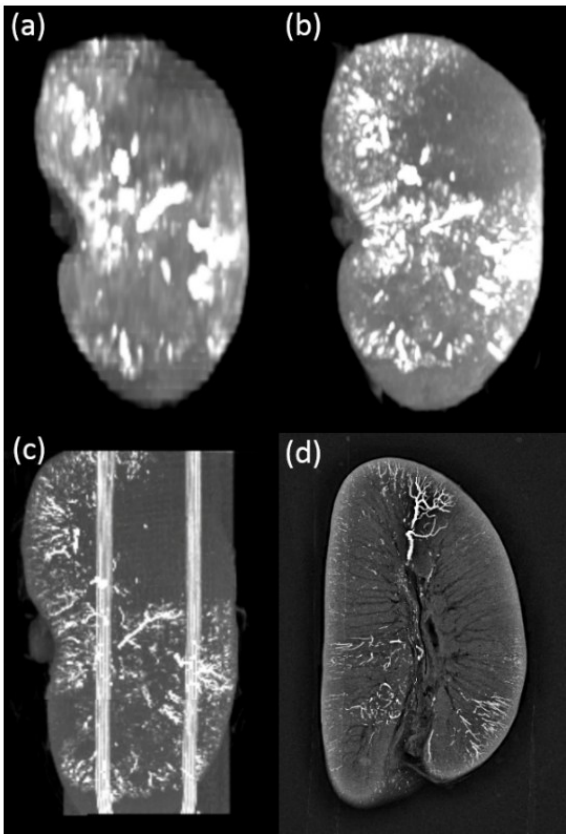

Figure 3.1: Demonstration of microsphere radiopacity across X-ray imaging modalities. (a) DRR from fan beam CT. (b) DRR from cone beam CT. (c) DRR from micro-CT. Animal heating coils are visible as vertical cylinders within the DRR. (d) Mammography image of an axial kidney slice removed from a region immediately inferior to the kidney's hilum.

One challenge associated with CT imaging for microsphere distribution evaluation is that current clinical CT scanners have in-plane and longitudinal resolution on the order

of 0.5 mm.[138] The consequence of these finite voxel sizes is that it is impossible to image individual microspheres with current clinical technology. Hence, CT voxels will have signal contributions from a combination of microspheres and tissue. Therefore, it is crucial to understand the correlation between CT voxel intensity and the microsphere concentration within the voxel before using CT for dosimetry calculations. Previous work has demonstrated that the HU values of bulk quantities of the prototype microspheres under assessment ranged from approximately 13,000 to 18,000 HU, but HU quantification of smaller, clinically relevant quantities of these microspheres has not yet been investigated.[139]

Here, we propose a methodology to quantify the inherent radiopacity of glass microspheres that will allow for the development of calibration curves to relate microsphere concentration within a CT voxel to corresponding HU enhancement for that voxel. The relationship between microsphere concentration and CT voxel enhancement is investigated through clinical CT imaging of uniform microsphere distributions in liver tissue-equivalent phantoms. Results from this work may be used to significantly improve the current clinically achievable dosimetry estimates. Post-administration CT imaging and subsequent quantification of the microsphere distribution would enable a precise absorbed dose calculation, and when coupled with physician-drawn contours of liver tumours and organs at risk, would provide dose-volume data that can improve our understanding of toxicity and therapeutic response in ^{90}Y TARE.

3.4 Methods and Materials

3.4.1 Radiopaque Microspheres

The microspheres used in this study were composed of a proprietary blend of yttrium-strontium-gallium-silicate oxide glass and were similar in size and density to TheraSphere microspheres (20-30 μm diameter, ρ = 3.3 g/cm^3). Depending on the microsphere formulation, the mole fractions of the constituent compounds ranged from 0.10–0.17 (Y_2O_3), 0.00–0.05 ($SrCO_3$), 0.15–0.30 (Ga_2O_3), and 0.50–0.67 (SiO_2). In this work, a single formulation was considered with high Y_2O_3 and $SrCO_3$ content, low Ga_2O_3 content, and mid-range SiO_2 content (Formulation 1). Following the establishment of this proposed methodology, more recent microsphere prototype formulations (herein referred

to as Formulation 2 and Formulation 3) were examined to demonstrate the increase in their inherent radiopacity, while still maintaining a size and density similar to TheraSphere microspheres.

3.4.2 Phantom Design

Liver tissue-equivalent phantoms were designed to determine CT voxel enhancement due to microsphere deposition within the phantoms. The phantoms were prepared by dissolving agarose (BP160, Thermo Fisher Scientific Chemicals Inc., Waltham, MA, USA) in distilled water (dH_2O) to achieve a 2.0% by weight (w) agarose concentration. The agarose solution was heated until it reached its boiling point, and then was poured into plastic vials (BRAND_40002, ProfiLab24, Berlin, Germany) for gelation. The agarose concentration of 2% was chosen as it produced pore sizes roughly 100x smaller than the average diameter of a microsphere, thus preventing microsphere migration through the agarose matrix.[140,141]

At a CT (SOMATOM Definition AS+, Siemens Healthcare Ltd, Erlangen, Germany) X-ray tube potential of 80 kVp, the agarose hydrogel had a value of −5 ± 8 HU (mean ± standard deviation). Trace amounts of sodium chloride (S271-3, Thermo Fisher Scientific Chemicals Inc., Waltham, MA, USA) were added to the solution to increase the HU to more accurately represent the range of liver tissue HU values reported in the literature.[142] To determine the appropriate concentrations of sodium chloride (NaCl) required to mimic the attenuation properties of liver tissue, 10 phantoms were developed using the agarose solution and doped with varying concentrations of NaCl ranging from 1.50% – 2.00% (w) and imaged with CT over three X-ray tube potentials – 80, 100, and 120 kVp. Average CT voxel values within the phantoms were plotted against the NaCl concentration of each phantom in Figure 3.2 for each X-ray tube potential. A NaCl concentration of 1.60% (w) was sufficient to increase the average CT voxel value to 20 – 30 HU for tube potentials between 80, 100, and 120 kVp. This NaCl concentration was subsequently used in the development of all liver tissue phantoms.

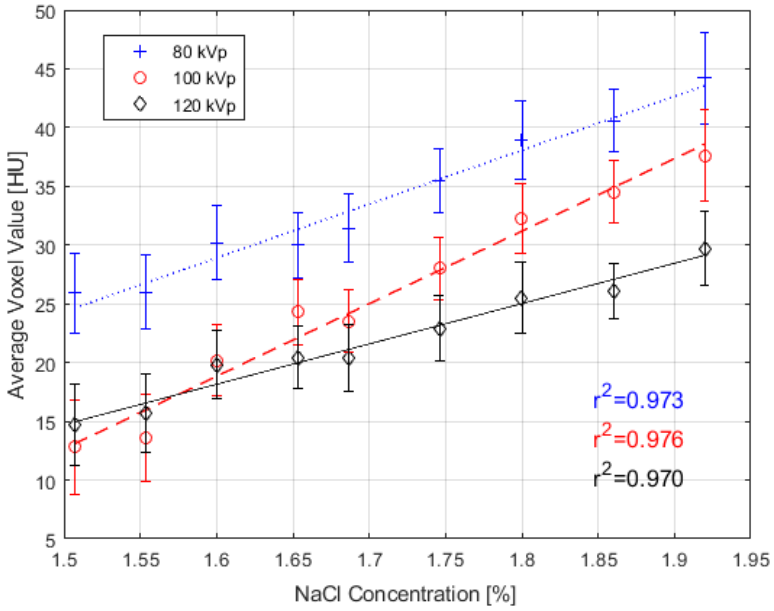

Figure 3.2: Average CT voxel values of phantoms containing dH2O, agarose [2%(w)] and varying concentrations of NaCl [1.5% - 2.0% (w)]. Data for ten phantoms were collected over three X-ray tube potentials: 80, 100, and 120 kVp. Error bars represent the standard deviation of the CT voxels values in the phantom volume.

To achieve a uniform spatial distribution of microspheres within the phantoms, microsphere samples ranging from 5.5 ± 0.1 to 40.6 ± 0.1 mg were measured using a precision scale. This range of values was chosen to approximate microsphere concentration values that were observed in the preclinical animal study. Concentrations in clinical scenarios may differ depending on tumour size and vascularity. Samples were individually deposited into 1.5 mL conical plastic vials with a cross-sectional inner diameter of 8.5 mm and a depth of 4.1 cm. Plastic vials were subsequently filled with the agarose solution and vigorously mixed using a vortex mixer for a period of approximately 10 s until the microspheres appeared to be uniformly mixed within the solution upon visual inspection. Immediately after mixing, the vials were submerged into an ice bath (~0 °C) to accelerate gelation and minimize microsphere settling to the most inferior point of the vial. Complete gelation occurred within seconds when submerged in the ice bath. Eight phantoms with varying concentrations of uniformly distributed microspheres were developed for this study with an additional phantom without microspheres serving as a control.

3.4.3 CT Imaging and Analysis

Phantoms were surrounded with slabs of solid water (Solid Water® HE, Sun Nuclear Corporation, Melbourne, FL, USA) to model X-ray scattering present in the clinical imaging of the abdomen. A 30 × 30 × 2 cm^3 square acrylic annulus was machined that allowed for the phantoms to be inserted into the central annulus space. Solid water slabs with thicknesses of 5 and 10 cm were placed above and beneath the 2 cm thick acrylic annulus allowing for simulated patients thicknesses of 12 and 22 cm. CT images were acquired from a 128-slice CT scanner (SOMATOM Definition AS+, Siemens Healthcare Ltd, Erlangen, Germany) using the CT acquisition parameters listed in Table 3.1. All scans were acquired in a helical scan mode with an exposure setting of 450 mAs. Images were reconstructed in voxels with dimensions 0.297 mm × 0.297 mm × 1.50 mm using FBP with a standard abdominal reconstruction kernel, B40f. CT imaging was performed within one hour of phantom preparation. Acquired CT images were analyzed in OsiriX (Pixmeo SARL, Bernex, Switzerland). A CT Volume-of-Interest (VOI) with axial dimensions equal to the microscope's FOV and a longitudinal dimension equal to the sum of a phantom's agarose slice thicknesses was used to determine the average CT voxel value in each phantom. Calibration curves for each CT acquisition were generated through a linear least-squares fit of the average HU and microsphere concentration in all VOIs.

CT Acquisition	Tube Potential [kVp]	Reconstructed FOV [cm]	Slice Thickness [mm]	Phantom Thickness [cm]
1	100	15	1.50	12
2	120	15	1.50	22

Table 3.1: Siemens SOMATOM Definition AS+ CT acquisition parameters.

3.4.4 Microscopy Imaging and Analysis

Post-CT imaging, the agarose hydrogels were carefully removed from the plastic vials. To ensure uniformity of the microsphere spatial distribution within each hydrogel, only the cylindrical region below the hydrogel meniscus and above the conical region within each vial was analyzed. Each cylindrical region was further divided into individual slices with an average thickness of 1.34 ± 0.13 mm (n = 71). Agarose residue was not

observed on the razor blade used to slice the hydrogel suggesting there was no loss of microspheres during this process. Individual agarose slices were imaged by brightfield microscopy (Eclipse Ti Inverted Microscope, Nikon Instruments Inc., Melville, NY, USA) to quantify the number of microspheres within a specified FOV. This process is pictorially described in Figure 3.3 and a sample microscopy image of an agarose slice is shown in Figure 3.4.

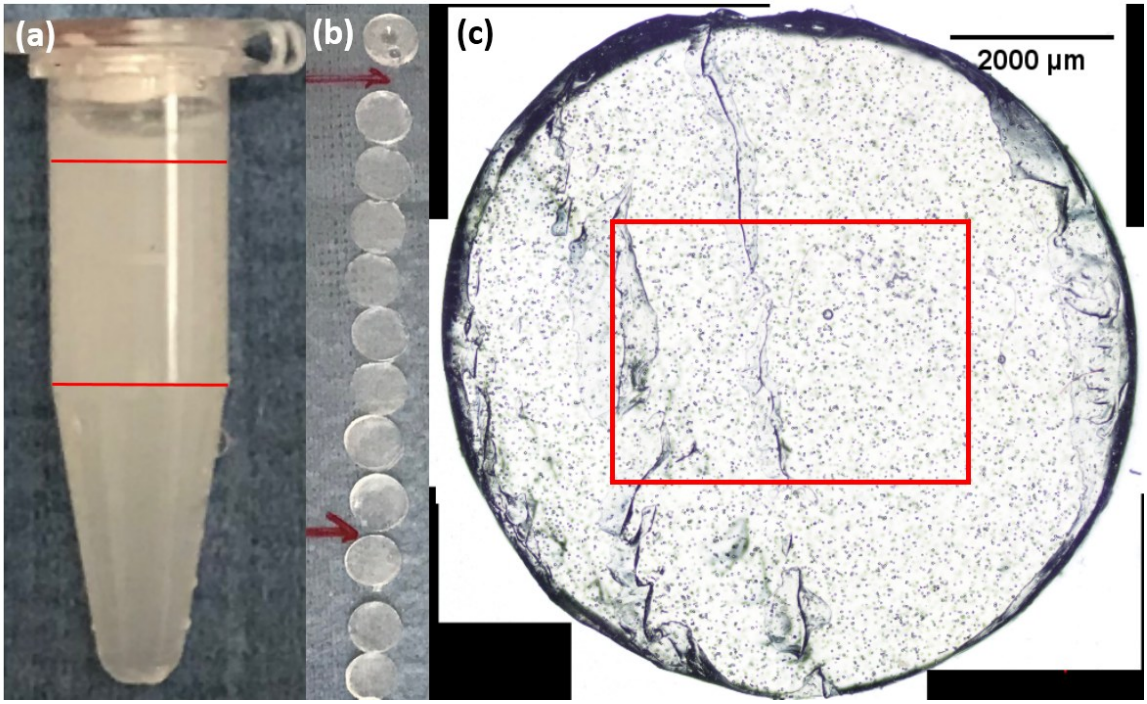

Figure 3.3: Pictorial representation of the microsphere concentration analysis. (a) Vial containing the agarose hydrogel. The analyzed cylindrical region is between the two horizontal red lines. (b) Individual agarose slices. Slices between the red arrows were analyzed. (c) Brightfield microscopy image of a single agarose slice. The red rectangle (14.20 mm^2) indicates the size and location of the microscope's FOV relative to the agarose slice.

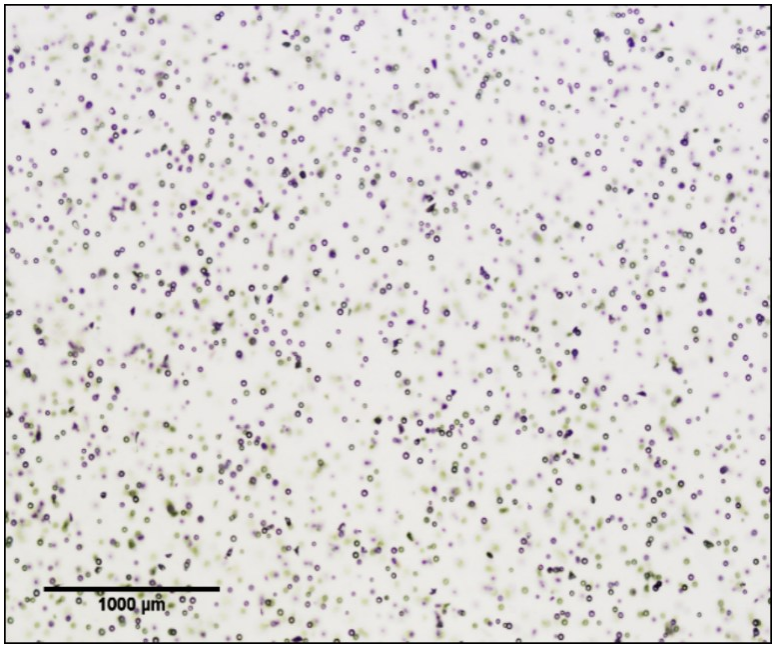

Figure 3.4: Brightfield image of an agarose slice at 2x magnification.

Microscopy images were imported into MATLAB R2018b (MathWorks Inc., Natick, MA, USA) where an in-house script quantified the number of microspheres within the microscope's 14.20 mm^2 FOV using a circular Hough transform.[143] The transform was individually calibrated for each microsphere concentration by manually counting the number of microspheres in a subset of the FOV, then optimizing the sensitivity and edge threshold parameters of the circular Hough transform to replicate those counts. Microsphere counting errors were determined by the percent difference of the manual counting and the counting determined using the Hough transform, which was approximately 3%, independent of microsphere concentration. The analyzed volume used to determine the microsphere concentration in a phantom was calculated by measuring the thickness of the agarose slices with a caliper, summing up all slice thicknesses, then multiplying this thickness by the area of the microscope's FOV. To transform the microsphere concentration from units of microspheres/milliliter [MS/mL] to units of microspheres/CT voxel [MS/voxel], the microsphere concentration was multiplied by a factor of 1.32×10^{-4} mL/voxel determined from the nominal CT voxel dimensions of 0.297 × 0.297 × 1.50 mm. The measured cylindrical volumes, range of microsphere counts within

these volumes, and calculated microsphere concentrations for all phantoms are given in Table 3.2.

To ensure all microspheres were quantified in the analyzed volume of a phantom, microscopy images were originally captured at 7 equally spaced depths within a single agarose slice using a consistent FOV and a 2x objective lens. Microspheres were counted in these 7 images and duplicate counts were removed in neighboring microscopy images by comparing the pixel coordinate pairs of all microspheres and removing coordinate pairs that differed by less than the average radius of a microsphere (15 μm). Microspheres were then counted at every second depth, i.e. depths 1, 3, 5 and 7, and duplicate counts were again removed. This process was repeated at every third depth, i.e. depths 1, 4, and 7. Assuming the 7-depth counts were the most accurate, the 4-depth and 3-depth counts deviated by less than 4%. The difference in microsphere counts when applying this approach are shown in the bar graph of Figure 3.5 for slice 8 of the phantom containing 15.2 mg of microspheres.

Microsphere Mass in Phantom [± 0.1 mg]	**Analyzed Volume [± 0.003 mL]**	**Microspheres in Analyzed Volume [± 5% MS]**	**Microsphere Concentration [MS/Voxel]**
5.5	0.1621	17602	14 ± 1
11.1	0.1428	28954	27 ± 1
15.2	0.1379	40578	39 ± 2
20.3	0.1719	49577	38 ± 2
26.1	0.1813	62477	46 ± 2
31.5	0.1750	73589	56 ± 3
35.5	0.1501	62468	55 ± 3
40.6	0.1561	80598	68 ± 3

Table 3.2: Microsphere concentration data for the eight agarose phantoms containing microspheres.

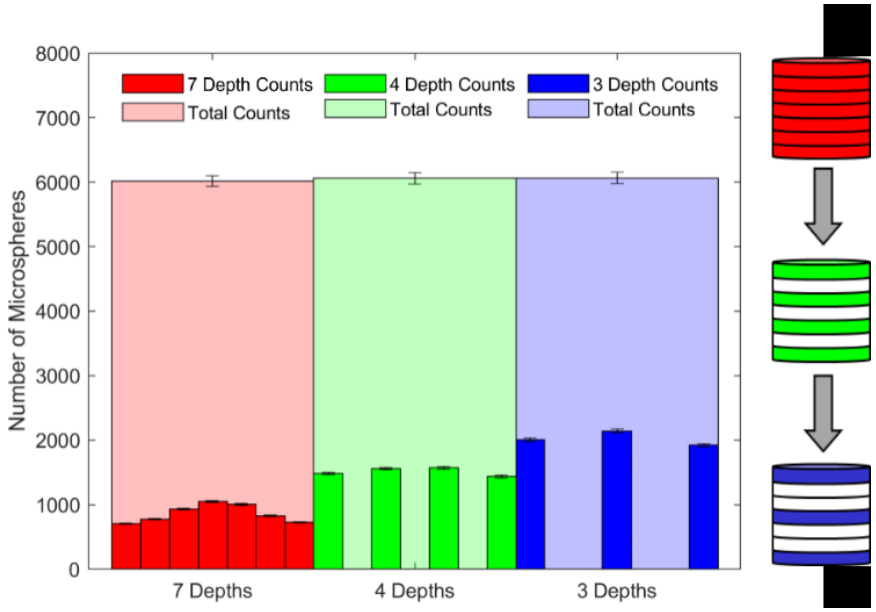

Figure 3.5: Differences in microsphere counts when using 7, 4, and 3 depths to quantify the total number of microspheres within slice eight of the phantom containing 15.2 mg of microspheres. A pictorial representation of depth selection in an agarose slice is shown to the right of the bar graph.

This microsphere quantification method was validated in the remaining eight slices of this phantom and the mean microsphere counts using 7, 4, and 3 depths were compared across all slices. Tukey's multiple comparison test demonstrated that there were no significant differences between the mean microsphere counts when using different depths to quantify the number of microspheres. As a result, the microscopy images in the remaining phantoms were collected and analyzed only for 3 equally spaced depths within a single agarose slice. Across all agarose phantoms investigated in this study, capturing microscopy images at 3 equally spaced depths within a single agarose slice rather than 7 reduced the number of microscopy images to be analyzed from 777 to 333. This reduced microscopy image acquisition and analysis time by more than half (13.4 to 5.7 hours) while still maintaining high quantitative accuracy in determining the total number of microspheres.

The pyramid-like shape of the 7-depth counts in Figure 3.5 can be attributed to the order in which microspheres were removed from adjacent microscopy images. A microsphere count was first established in the middle image (4/7) resulting in the highest count. Microspheres with similar pixel coordinates detected in the adjacent superior (5/7)

and inferior (3/7) images were removed from those images. Similarly, microspheres detected in (5/7) with similar pixel coordinates as those detected in (6/7) were removed from (6/7), and microspheres detected in (3/7) with similar pixel coordinates as those detected in (2/7) were removed from (2/7). This iterative process was applied until the uppermost (7/7) and lowermost (1/7) images were reached. Hence, the fewest microspheres were detected in the images that are the farthest away from the middle image.

3.4.5 Limit of Detection

The International Organization for Standardization defines the limit of detection (LOD) as the net concentration of a component in a material that will lead to the conclusion that the concentration of analyzed component is greater than that of a control sample.[144] This LOD concept has previously been applied to iodinated contrast agents in CT[145], and was invoked to describe the limit of microsphere detectability and is calculated using Equation 3.1.

$$LOD_{HU} = LOB_{HU} + 1.645\sigma_{low} \tag{3.1}$$

Here, LOD_{HU} is the LOD in terms of HU, LOB_{HU} is the limit of blank (LOB) determined from repeat measurements of a control sample, 1.645 is the Z-score for a one-sided standard normal distribution with a false positive detection rate of $\alpha = 0.05$, and σ_{low} is the HU standard deviation when microspheres are present in the phantom at the lowest microsphere concentration. The parameter α corresponds to the probability of committing false positives. For α = 0.05, the LOD_{HU} is calculated assuming only a 5% probability of committing false positives. The LOB in terms of HU (LOB_{HU}) is defined in Equation 3.2.

$$LOB_{HU} = \mu_{agar} + 1.645\sigma_{agar} \tag{3.2}$$

Here, μ_{agar} and σ_{agar} are the average and standard deviation of repeat measurements of the control phantom in HU. Calculating LOB_{HU} and LOD_{HU} requires data to be normally distributed. Once the LOD_{HU} has been calculated, calibration curves are used to determine the corresponding LOD in terms of microsphere concentration, $LOD_{MS/vox}$ and $LOD_{MS/mL}$.

3.4.6 Statistical Analysis

A Student's t-test was used to compare the slopes and intercepts of the calibration curves relating average CT voxel values and microsphere concentration, as described by Andrade *et al*.[146] When comparing slopes derived from three microsphere formulations, the analysis of covariance (ANCOVA) and a post-hoc Tukey's test were implemented due to the increased number of comparisons.[146] Tukey's test was also used to compare the mean microsphere counts between agarose slices within a phantom and also between different depths within a single agarose slice. A one-sample Kolmogorov-Smirnov test was used to determine the normality of the distribution of CT voxel values.[147] The correlation between CT voxel values and microsphere concentration was quantified using the coefficient of determination, r^2. All statistical analyses were performed in MATLAB. The results of all statistical tests were considered significant when their p-values were less than 0.05.

3.5 Results

3.5.1 Microsphere Distribution

In all phantoms containing microspheres, the spatial uniformity of the microsphere distribution was examined through the analysis of CT and microscopy images. To illustrate the CT uniformity, line profiles were drawn down the central longitudinal axis of all phantoms. Line profiles of two example phantoms are shown in Figure 3.6. The mean of the standard deviations of all line profiles is 11 ± 3 HU with a standard deviation range of 7 to 15 HU. Only CT voxels below the agarose hydrogel meniscus and above the conical region were used to calculate each HU standard deviation. This distance was consistent across all phantoms with a mean of 0.95 ± 0.02 cm. However, if the agarose at the most inferior point of the phantom containing 11.1 mg of microspheres is included in the line profile, the standard deviation of the CT voxel values increases by 235% from 7 to 23 HU. This is caused by the settling of a small portion of the microspheres that in turn produced a spike in the line profile of Figure 3.6. Such a large percent change was only observed in 2 of 8 phantoms (potentially due to variations in sample preparation), but still validates the need to restrict the data analysis to the cylindrical region of each phantom.

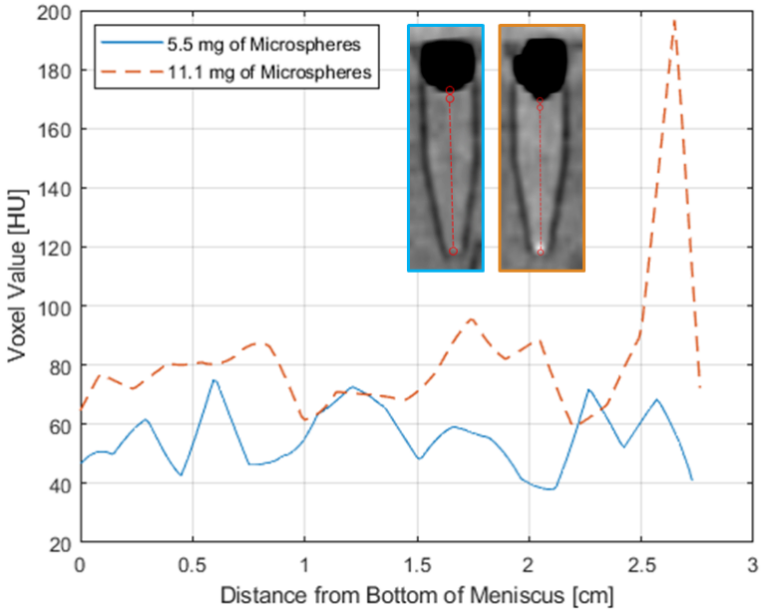

Figure 3.6: CT image line profiles (shown in inset) down the central longitudinal axis of two phantoms, beginning at the bottom of the hydrogel meniscus and terminating at the most inferior point of the plastic vial. Images were acquired using the CT acquisition parameters of acquisition 2.

For a spatial uniformity analysis on the microscopic scale, microspheres in the microscope's FOV were counted at 3 equally spaced depths of each agarose slice of the cylindrical region in each phantom. Results of these counts are shown in Figure 3.7. The horizontal bar represents the mean number of microspheres in each phantom. Error bars represent the standard deviation of the counts over the 3 depths of each slice and do not incorporate the 3% uncertainty in counts arising from the Hough transform. Tukey's multiple comparison test was employed to compare the microsphere counts in each slice of a phantom. Results show there is no statistically significant difference in the number of microspheres between the constituent slices of any single phantom, excluding slice 4 of the phantom containing 26.1 mg of microspheres. In this isolated case, slice 4 had a significantly different number of microspheres relative to slices 2 (p = 0.001), 3 (p = 0.039), 5 (p = 0.030), 6 (p = 0.007), 7 (p = 0.019), and 9 (p = 0.007). Regardless, all slices of this phantom were included when quantifying the microsphere concentration as the CT VOI used to determine the average HU in the phantom was continuous, and the volumes used to determine the microsphere concentration and average HU must be equivalent when developing calibration curves.

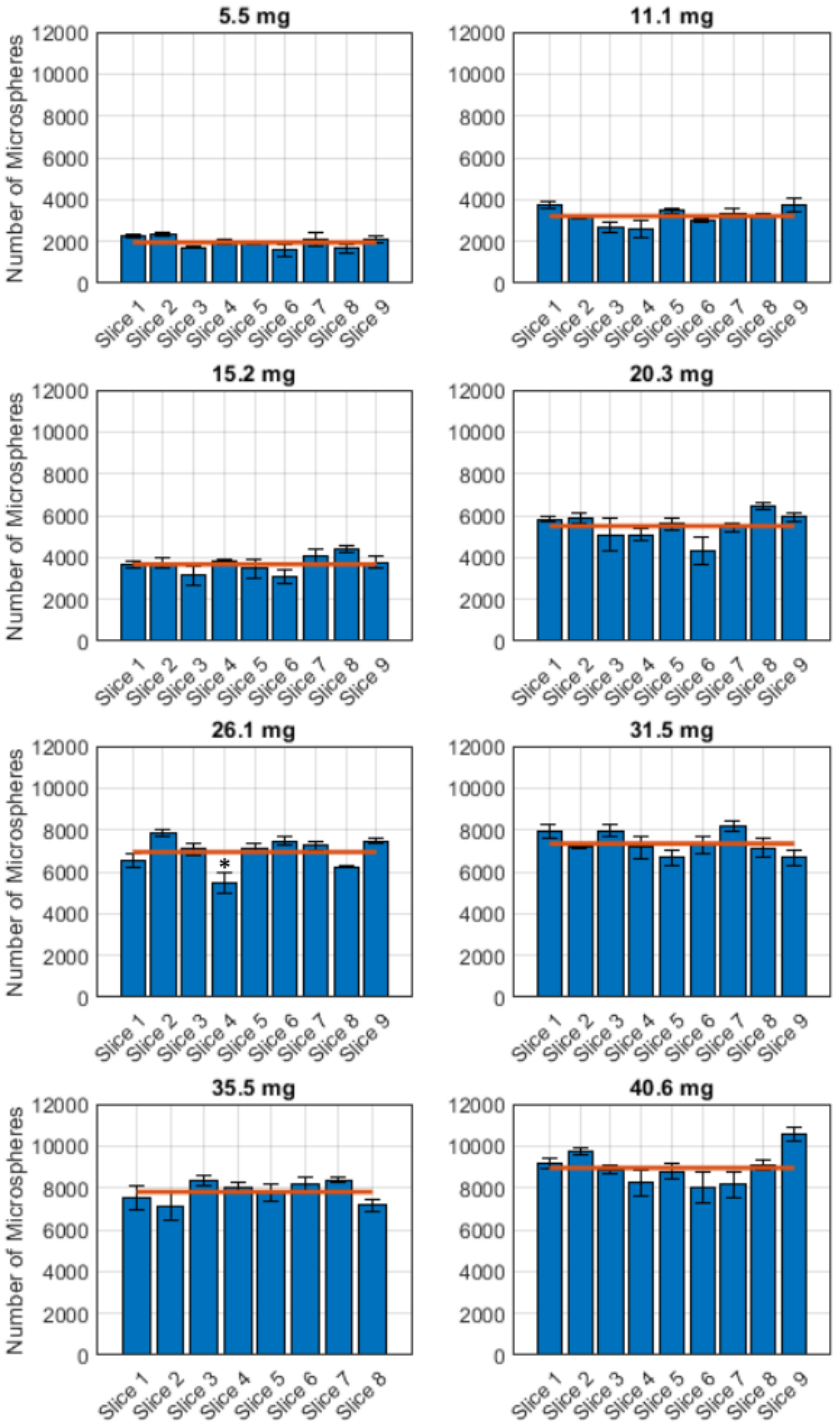

Figure 3.7: Microsphere counts in each slice of the cylindrical region of the phantoms. Slices have an average thickness of 1.34 ± 0.13 mm (n = 71). The asterisk indicates a statistical outlier and the horizontal bar indicates the mean number of microspheres in the phantom. Error bars represent the standard deviation of the counts over the three depths in each slice.

3.5.2 Calibration Curves

Microsphere concentrations used to generate the calibration curves are the concentrations in the cylindrical region of the agarose hydrogel of each phantom, as shown in Figure 3.3(a). The relationship between the average CT voxel value and the microsphere concentration in that voxel is shown in Figure 3.8 for both CT acquisitions listed in Table 3.1. The corresponding coefficients of determination are both equal to 0.949, indicating that a strong, positive correlation exists between CT voxel values and microsphere concentration. Numerical values for the calibration curves' coefficients of determination, slopes, intercepts, and confidence intervals (CI) are presented in Table 3.3.

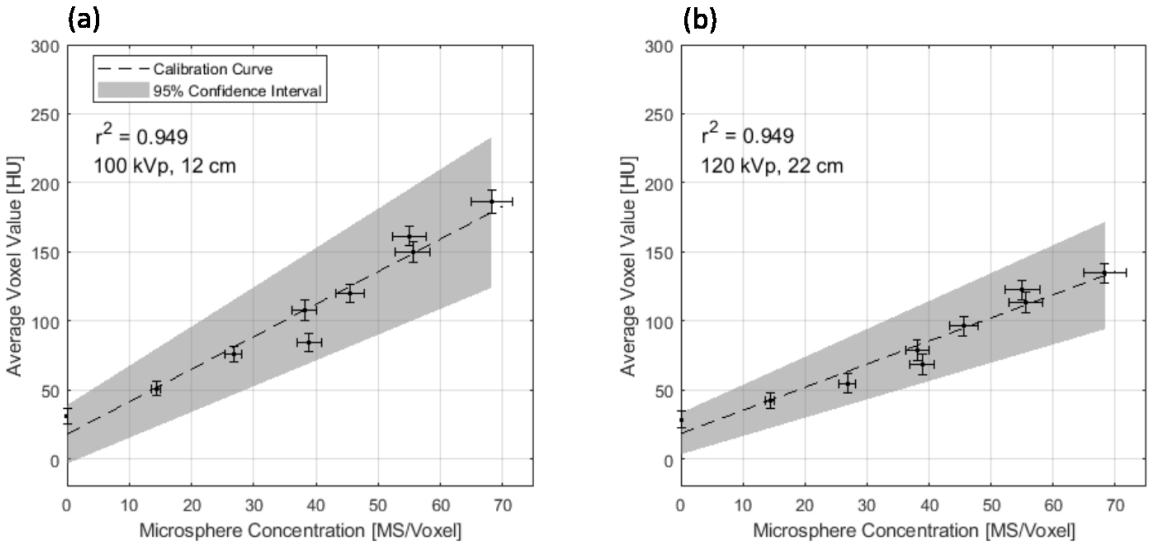

Figure 3.8: CT calibration curves relating average CT voxel value to microsphere concentration in the phantoms for (a) Acquisition 1 and (b) Acquisition 2. The HU error bars are standard deviations of the CT voxel values in the VOI. Error bars associated with microsphere concentration are calculated from volumetric and microsphere counting uncertainty.

CT Acquisition	r^2	Slope (95% CI) [MS/Voxel]	Intercept (95% CI) [HU]
1	0.949	2.36 (1.87 – 2.85)	17.79 (-3.35 – 38.93)
2	0.949	1.68 (1.33 – 2.02)	18.38 (3.35 – 33.41)

Table 3.3: Coefficients of determination, slopes, intercepts, and corresponding confidence intervals for the linear fits of the calibration curves.

3.5.3 Limit of Detection

The distribution of the CT voxel values constituting each phantom met the condition of normality according to a one-sample Kolmogorov-Smirnov test, as required to determine their LOD_{HU}. As phantoms were originally developed to cover a wide range of microsphere concentrations, σ_{low} in Equation 3.1 was approximated using the HU standard deviation of the phantom with the minimum microsphere concentration containing 5.5 mg of microspheres. The LOD_{HU} values are equal to 69 and 71 HU for CT acquisitions 1 and 2, respectively. These LOD_{HU} values are 38 and 42 HU greater than the average HU of the control phantoms for CT acquisitions 1 and 2, respectively. Due to different slope and intercept values between the two calibration curves, the $LOD_{MS/vox}$ values are equal to 22 to 31 microspheres per CT voxel for CT acquisitions 1 and 2, respectively. These values correspond to 1.63×10^5 and 2.37×10^5 MS/mL, respectively.

3.6 Discussion

3.6.1 Microsphere Distribution

Due to the restriction of analyzing the phantoms in the cylindrical region of the agarose hydrogel, as shown in Figure 3.3(a), the microsphere spatial distribution in the phantoms did not demonstrate any significant changes in the number of microspheres as a function of depth, excluding slice 4 from the phantom containing 26.1 mg of microspheres. This spatial uniformity is macroscopically verified by the uniform HU values in the cylindrical region of the two representative phantoms in Figure 3.6.

3.6.2 Calibration Curves

According to Table 3.3, CIs for the slopes and intercepts overlap for all acquired CT scans. Results of a Student's t-test show there are no significant differences between the intercepts associated with each calibration curve, but there is a significant difference between the slope values (p = 0.018). The presence of CT image noise will also affect the quantitative determination of the true microsphere concentration in a CT voxel. Increasing the simulated patient thickness results in a corresponding increase in image noise and hence an increase in LOD_{HU}. To quantify the effect of increasing phantom thickness on the detectable limit of these microspheres, various thicknesses of solid water slabs ranging from 5 to 20 cm were imaged with CT over a range of tube potentials (80, 100, 120 kVp)

for a fixed slice thickness (1.50 mm), exposure (450 mAs), and reconstructed FOV (15.0 cm). The LOD_{HU} was calculated according to Equation 3.1 substituting μ_{agar} and σ_{agar} for the corresponding values in the solid water slabs. In Figure 3.9, the LOD_{HU} is plotted against the phantom thickness for all X-ray tube potentials. These data suggest that the LOD_{HU} increases linearly with phantom thickness due to an increase in image noise from additional X-ray scattering within the phantom. Increased X-ray tube current, thicker CT slices and smoother reconstruction kernels can be implemented to further reduce CT image noise and its effect in determining the true microsphere concentration within a voxel and corresponding LOD.[148] However, increasing slice thickness and using smoother reconstruction kernels can result in a tradeoff between image noise and spatial resolution.

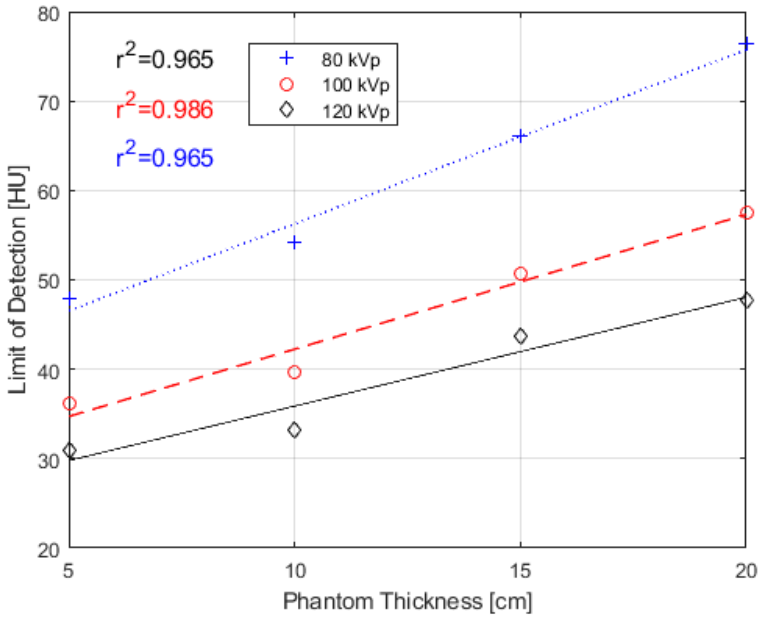

Figure 3.9: LOD_{HU} as a function of phantom thickness for three X-ray tube potentials: 80, 100, and 120 kVp.

3.6.3 CT Imaging Parameters

The CT slice thickness was kept at a constant value of 1.50 mm in this study. In clinical situations where a liver tumour may not be fully encompassed in a single slice, partial volume effects may decrease image contrast. Reduced slice thicknesses have been shown to improve tumour detection in these cases.[149] The CT reconstructed FOV was also

kept constant at 15 cm to match the annulus' radial dimension and to maximize the CT image spatial resolution.

The default Siemens' abdominal protocol image reconstruction kernel was found to produce satisfactory results for this study. CT image reconstruction of an early generation of point-source agarose models was attempted with sharper (B80f) and smoother (B10f) kernels, but the B80f kernel overly accentuated image noise and the B10f kernel smoothed out unintentionally induced non-uniformities within the agarose hydrogel. Profiles through the maximum HU value in a single point-source microsphere distribution from the first generation of phantoms are provided in Figure 3.10(a). Their corresponding CT images reconstructed with B10f and B80f kernels are shown in Figure 3.10(b) and Figure 3.10(c), respectively. The profiles show that the image reconstructed with the sharper kernel has a maximum value 61.5 HU greater than the corresponding maximum in the image reconstructed with the smooth kernel. In a uniform region void of microsphere uptake, the sharp kernel reconstruction has a standard deviation 2.5 HU greater than the smooth kernel reconstruction.

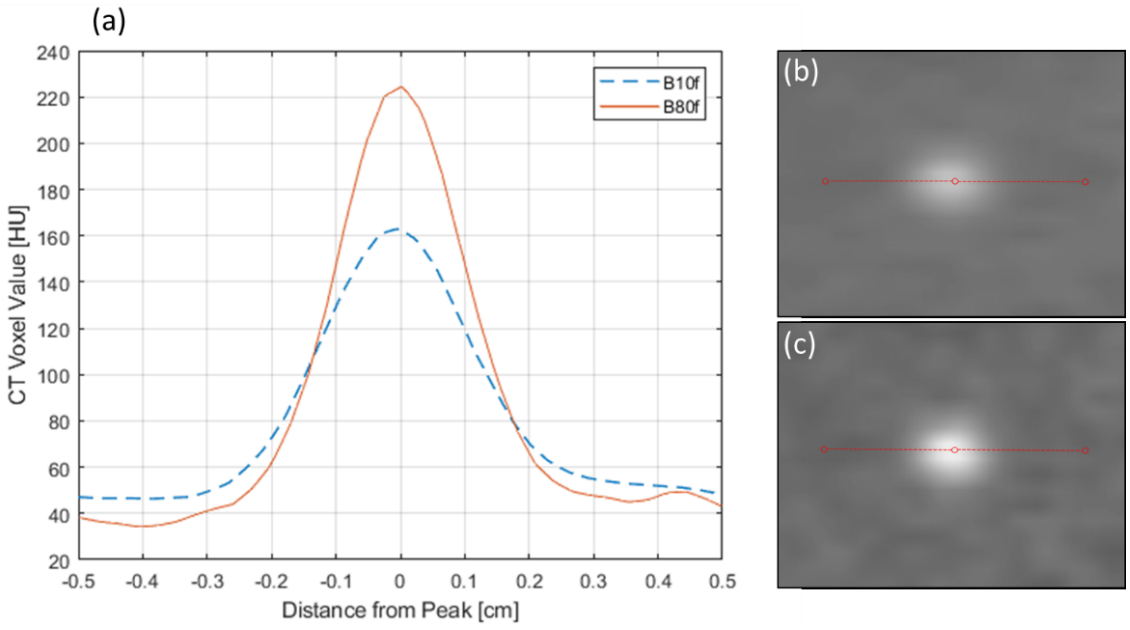

Figure 3.10: (a) CT voxel intensity [HU: -100 to 300] through the maximum value of a point-source microsphere distribution in agarose. (b) CT image of the point-source distribution reconstructed with the smooth B10f kernel. (c) CT image of the point-source distribution reconstructed with the sharp B80f kernel.

These earlier generation of phantoms were also imaged with a variation in CT slice thickness and FOV, but when the value of these parameters was halved, no significant change was detected in the average CT voxel value of the microsphere distribution. This implies that CT slice thickness and FOV can be doubled without impacting the quantification of MS concentration in these phantoms, as long as the VOI in the phantom is consistently defined.

3.6.4 Limit of Detection

As the LOD_{HU} is a function of both the mean and standard deviation of the CT voxel values of the control phantom, this parameter depends on the assumption of the liver tumour's average HU, which was arbitrarily defined between 20 and 30 HU, depending on the X-ray tube potential. Altering this baseline value will consequently alter the LOD_{HU}. Furthermore, reducing the standard deviation of the CT voxel values will improve the accuracy of the LOD_{HU} (for a fixed CT acquisition). Noise reduction techniques previously mentioned can be implemented to this end.

3.6.5 Application to Recent Formulations

As this proposed methodology to determine the inherent radiopacity of radiopaque microspheres proved successful in the original microsphere formulation (Formulation 1), it was applied to more recent microsphere formulations (Formulations 2 and 3) whose composition was optimized in an effort to increase their inherent radiopacity relative to Formulation 1. Figure 3.11 demonstrates the difference in radiopacity over these three microsphere formulations. The X-ray tube potential used to image Formulations 2 and 3 was 80 kVp, but the slice thickness and FOV were altered relative to the values used to image Formulation 1, resulting in different voxel sizes. As the CT voxel sizes differ for Formulations 2 and 3 relative to Formulation 1, the microsphere concentrations are given in terms MS/mL. In terms of this concentration unit, the $LOD_{MS/mL}$ values for Formulations 1, 2, and 3 are 2.65×10^5, 7.39×10^4, and 5.39×10^4 MS/mL, respectively. Formulations 2 and 3 have a smaller LOD compared to Formulation 1 not only due to their increased radiopacity, but also to an improvement in phantom development which increased confidence in determining the true microsphere concentration and enabled a smaller σ_{agar} used in Equation 3.2.

Determining the radiopacity of these additional microsphere formulations allowed for the refinement of this methodology, a reduction in uncertainties, and an opportunity to further investigate calibration curve linearity at higher and lower microsphere concentrations. A comparison of the slope and intercept values using ANCOVA revealed no significant differences in the intercept values, but did reveal significant differences between the slopes ($F(2,6) = 25.67$, $p = 0.001$). The post hoc Tukey test reveals a p-value less than 0.001 for the Formulation 1 and Formulation 2 comparison, $p = 0.243$ for the Formulation 1 and Formulation 3 comparison, and $p = 0.910$ for the Formulation 2 and Formulation 3 comparison. The lack of significance in the comparison of the slopes derived from Formulation 1 and Formulation 3 is attributed to the reduced range of microsphere concentrations in the analysis of Formulation 3.

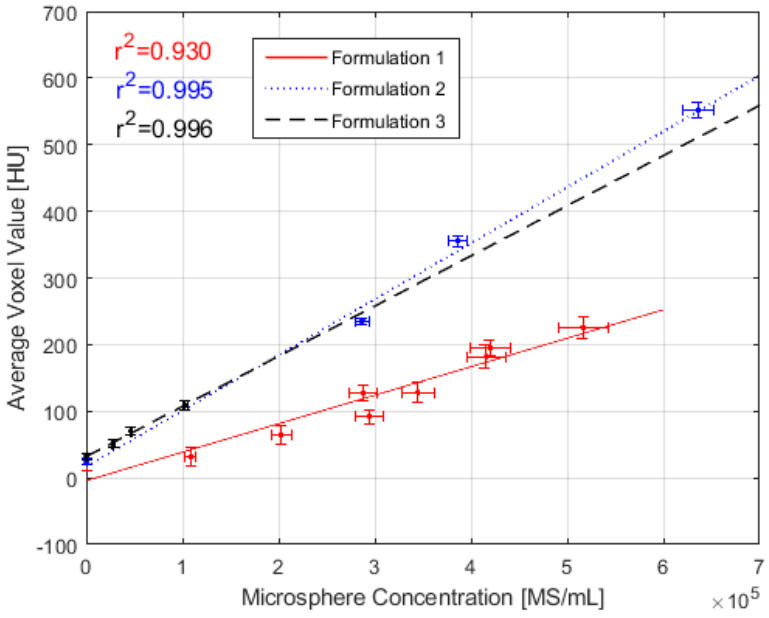

Figure 3.11: CT calibration curves for three microsphere formulations relating average CT voxel values to microsphere concentration. The HU error bars are standard deviations of the voxel values in the VOI and error bars associated with microsphere concentration are calculated from volumetric and microsphere counting uncertainty.

3.6.6 Study Limitations

The greatest uncertainty in developing calibration curves relating CT voxel values to microsphere concentration is in quantifying the number of microspheres uniformly distributed within the agarose hydrogel. When present, ridges and troughs on the surfaces of the agarose slices can produce false positives when quantifying the number of microspheres using a circular Hough transform. More careful slicing or a more accurate methodology for microsphere quantification may provide increased confidence in a calibration curve's slope and intercept.

Agarose was chosen as the primary material in the phantoms due to its tissue-equivalent properties, ease of access, and its ability to incorporate other trace elements to alter the X-ray imaging properties of the material. However, agarose is not ideal from a material stability standpoint. Due to its large water fraction, phantom dehydration poses a problem if they are not vacuum sealed and are to be imaged over the course of several hours, depending on local humidity conditions. This quality limits the practical use of agarose as a liver tissue surrogate in developing calibration curves for radiopaque microspheres.

Microscopy studies of *ex vivo* liver samples have shown that glass microspheres tend to aggregate in small clusters of up to 20 microspheres, depending on liver tumour's vascularity.[54] Previous work by our group has investigated CT voxel enhancement due to small clusters (15–1500) of the initial formulation of radiopaque microspheres in liver tissue-equivalent phantoms. Preliminary results show good agreement in terms of calibration curve parameters with microsphere clusters as large as several hundred microspheres. Additional work is required to investigate this relationship for more recent microsphere formulations.

In this work, a singular liver tumour HU value is assumed. Each patient will likely have a unique tumour HU, and this will scale the calibration curves to higher or lower HU values, depending upon attenuation characteristics of the tumour. Furthermore, the HU heterogeneity within a tumour will likely be much larger than that observed in the fabricated agarose phantoms. As these CT calibration curves are relative to a background value, curves would have to be calculated on a patient-by-patient basis. To that end, NaCl phantom concentration could be altered to achieve a variety of background values.

Alternatively, pre- and post-CT imaging of a liver tumour before and after microsphere administration would give a relative HU enhancement, ΔHU, which could be an alternative metric in developing future calibration curves for these microspheres. It has also been shown that the CT scanner's manufacturer can influence HU accuracy.[150] The development of a single, transportable calibration phantom could address this problem by providing a means to calibrate CT scanners from a range of manufacturers across multiple institutions.

Since a relatively small fraction of administered activity is usually shunted to the lungs, it is entirely possible that CT-based evaluation of microsphere distribution in the lungs after treatment will not be practical. The challenge of calculating lung dose after treatment remains similar to that faced by current ^{90}Y-based microsphere administrations.

Future work aims to apply these calibration curves to CT scans of animal models embolized with radiopaque microspheres and extract an accurate radiation dose.

3.6.7 Impact

Despite many studies having demonstrated a positive correlation between the absorbed dose and objective tumour response in patients treated with ^{90}Y glass microspheres in TARE, a precise dose threshold for objective tumour response is yet to be defined. Absorbed tumour doses resulting in tumour response range from 100 – 500 Gy, although these values are estimates of an average dose determined by PET or SPECT imaging.[45,70,102,103,135] The true dose heterogeneity cannot be quantified with these low-resolution imaging modalities. However, microscopy studies of *ex vivo* liver samples have found that an actual delivered HCC tumour dose was in the range of 100 – 8000 Gy, while the intended tumour dose was 150 Gy.[54] Another microscopy study estimated that the minimum HCC tumour dose was less than half of the average tumour dose.[90] Quantifying the true tumour dose heterogeneity is vital as low dose regions correlate with reduced local control and increase the chance of local recurrence.[151] High-resolution CT imaging of microsphere distributions will provide increased confidence in the true spatial distribution of the microspheres, hence the distribution of ^{90}Y activity in the tumour. This is an essential prerequisite in determining the absorbed tumour dose and will allow for an improved characterization of the absorbed dose heterogeneity in TARE.

If high-resolution, post-administration CT imaging can better characterize the true microsphere distribution and corresponding absorbed dose, and liver tumour dose thresholds can be established for radiopaque ^{90}Y microspheres, then a viable patient-response relationship can be established and should translate into improved patient outcomes.

3.7 Conclusion

In this work, a methodology was proposed for the development of calibration curves relating microsphere concentration within a CT voxel to the corresponding HU of that voxel. This relationship was investigated through clinical CT imaging of microsphere distributions in liver tissue-equivalent phantoms. Results of this work show that HU values and microsphere concentration are positively correlated over a range of CT acquisition parameters. Our findings demonstrate the potential of CT to quantify the infusion of microspheres for more accurate dosimetry in TARE when used in conjunction with proper dosimetry software. This finding may improve our understanding of the relationship between absorbed dose and tumour response, which could ultimately translate into improved patient outcomes. The optimization of the prototype microsphere composition to maximize its inherent radiopacity will be an important step in realizing this goal.

Chapter 4 Manuscript 2: Post-Administration Dosimetry in Yttrium-90 Radioembolization through micro-CT Imaging of Radiopaque Microspheres in a Porcine Renal Model

4.1 Prologue

This manuscript describes the first implementation of CT-based dosimetry in TARE following micro-CT imaging of non-radioactive, radiopaque microspheres distributions a porcine renal model. The impact of the spatial resolution of an imaging system on the extraction of specific dose metrics was investigated. This manuscript demonstrates high-resolution micro-CT imaging of *in vivo* radiopaque microsphere distributions can provide increased confidence in characterizing the absorbed dose heterogeneity in ^{90}Y TARE, and that dose-volume metrics are correlated with the spatial resolution of the imaging modality.

This manuscript was published in *Physics in Medicine & Biology*. The reference is provided below.

- Henry, E. C., Strugari, M., Mawko, G., Brewer, K. D., Abraham, R., Kappadath, S. C., & Syme, A. (2021). Post-administration Dosimetry in Yttrium-90 Radioembolization through Micro-CT Imaging of Radiopaque Microspheres in a Porcine Renal Model. *Physics in Medicine & Biology*, *66*(9), 095011.

4.2 Abstract

Purpose: To perform post-administration dosimetry in ^{90}Y TARE through micro-CT imaging of non-radioactive, radiopaque microspheres distributions in a porcine renal model, and to explore the impact of spatial resolution of an imaging system on the extraction of specific dose metrics.

Methods: Following the administration of non-radioactive, radiopaque microspheres to the kidney of a hybrid farm pig, the kidney was explanted and imaged with micro-CT. To produce an activity distribution, 400 MBq of ^{90}Y activity was distributed throughout segmented voxels of the embolized vasculature based on an established linear

relationship between microsphere concentration and CT voxel value. This distribution was downsampled to coarser isotropic grids ranging in voxel size from 2.5 mm to 15 mm to emulate nominal resolutions comparable to those found in ^{90}Y PET and bremsstrahlung SPECT imaging. Dose distributions were calculated through the convolution of activity distributions with DVKs generated using the GATE Monte Carlo toolkit. Contours were computed to represent normal tissue and target volumes. Dose-volume histograms, dose metrics, and dose profiles were compared to a ground truth dose distribution computed with GATE.

Results: The mean dose to the target for all studied voxel sizes was found to be within 5.7% of the ground truth mean dose. The dose-volume metric D_{70} was shown to be strongly correlated with image voxel size of the dose distribution ($r^2 = 0.897$). D_{70} is cited in the literature as an important dose metric and its dependence on voxel size suggests higher resolution dose distributions may provide new perspectives on dose-response relationships in ^{90}Y TARE.

Conclusion: This study demonstrates that dose distributions with large voxels incorrectly homogenize the dose by attributing escalated doses to normal tissues and reduced doses in high-dose target regions. High-resolution micro-CT imaging of radiopaque microsphere distributions can provide increased confidence in characterizing the absorbed dose heterogeneity in ^{90}Y TARE.

4.3 Introduction

HCC – the most prevalent of all primary liver cancers – is the third leading cause of cancer deaths worldwide and its mortality rates have increased faster than mortality rates for any other common cancer.[152,153] Curative treatments include surgical resection and transplantation, although most patients do not meet the criteria for these procedures.[20,154] TARE is an alternative treatment for nonresectable liver cancer where ^{90}Y-labeled microspheres are administered through a microcatheter placed within the hepatic arterial vasculature to selectively target and irradiate liver tumours while sparing the surrounding healthy liver parenchyma. The successful infusion of microspheres in the tumour's microvasculature can be attributed to the unique perfusion of the liver in which tumoural

tissue derives its blood supply almost exclusively from the hepatic artery while healthy liver parenchyma derives approximately 80% its blood supply from the portal vein.[31]

There are two commercially available microspheres in TARE: TheraSphere® glass microspheres (Boston Scientific Corp., Marlborough, MA, USA) and SIR-Spheres® resin microspheres (Sirtex Medical Inc., Woburn, MA, USA). Both products utilize ^{90}Y as the therapeutic agent, which is a pure β^- emitter decaying to stable ^{90}Zr with a physical half-life of 64.2 ± 0.30 hours (2.68 days).[58] The average and maximum β^- emission energies are 0.9267 ± 0.0008 MeV and 2.2787 ± 0.0013 MeV, respectively, which correspond to a β^- particle range of 2.4 mm and 11.0 mm in water.[59,60] The radial distance at which 90% of the emitted ^{90}Y energy is absorbed, X_{90}, is equal to 5.4 mm.[61]

Due to the limited range of these β^- particles, it is essential to fully characterize the microsphere spatial distribution if one is to perform accurate post-treatment dosimetry in ^{90}Y TARE. PET and SPECT imaging of microsphere spatial distributions can provide estimates of the mean absorbed dose to the tumour and surrounding healthy tissue. Despite accumulating evidence supporting a strong, positive correlation between absorbed dose and tumour response in patients treated with TheraSphere microspheres, precise tumour dose thresholds have not been consistently defined.[55,70,103,135,155] This may be partially attributed to the nominal and spatial resolutions of PET and SPECT in which the nominal resolution (voxel size), among other factors, affects the achievable spatial resolution performance. The spatial resolution measured by the FWHM is reported to lie between 5.0 and 10.0 mm in ^{90}Y PET imaging and between 7.0 and 30.0 mm in bremsstrahlung SPECT imaging.[9–11]

These values are larger than the average range of ^{90}Y β^- emissions and are orders of magnitude larger than the distance scale over which changes in microsphere concentration have been observed.[54,91] The resultant blurring of the ^{90}Y activity distribution image can diminish true variations in the absorbed dose and incorrectly ascribe a more homogeneous distribution. Accordingly, there exists an unmet clinical need to provide substantially higher spatial resolution imaging of microsphere distributions to facilitate high-accuracy dose calculations in ^{90}Y TARE. The superior spatial resolution of X-ray imaging modalities has the potential to address this shortcoming.

X-ray-based evaluations of TheraSphere and SIR-Spheres distributions are not currently performed as the visualization of microsphere-loaded vasculature is insufficient to be of clinical use.[38,156] However, a novel, prototype glass microsphere is currently under development by ABK Biomedical (Halifax, NS, Canada) that incorporates high-Z elements within its material composition to confer substantial radiopacity to the microsphere. In turn, this allows high-resolution X-ray imaging to be used to visualize the microsphere's *in vivo* spatial distribution with improved accuracy relative to PET and SPECT imaging. The radiopacity of previous radiopaque microsphere formulations has been verified in clinically relevant concentrations through CT imaging of tissue-equivalent phantoms.[157]

Post-administration CT imaging of radiopaque microsphere distributions can directly impact our current understanding of the dose-response relationship in ^{90}Y TARE, which is crucial for the accurate determination of tumour doses and healthy tissue tolerances to improve normal tissue complication probability (NTCP) and TCP models. Furthermore, post-administration CT imaging could immediately reveal undertreated regions within the tumour volume which could be quickly addressed with adjuvant therapies, such as ablation or SBRT. It is important to identify these regions as they have been shown to correlate with reduced local control and an increased probability of local recurrence in the treatment of HCC.[151]

The objective of this study is to perform high-accuracy dosimetry in ^{90}Y TARE by convolving DVKs with simulated ^{90}Y activity distributions derived from micro-CT (μCT) imaging of non-radioactive, radiopaque microspheres distributions within a porcine renal model, and to explore the impact of the spatial resolution of an imaging system on the extraction of specific dose metrics.

4.4 Methods and Materials

4.4.1 Radiopaque Microspheres

The radiopaque microspheres used in this study were multi-component, yttrium-89 (^{89}Y)-infused microspheres composed of an experimental, proprietary blend of yttrium-strontium-gallium-silicate oxide glass and were similar in size and density to TheraSphere microspheres (20-30 μm diameter, ρ = 3.3 g/cm^3). A total of 480 mg of these microspheres were administered into the segmental arteries of the left kidney in a hybrid farm pig. These

microspheres did not undergo neutron activation to produce ^{90}Y as the primary goal of the animal study was to evaluate the radiopacity of the radiopaque microsphere formulation, not to perform dosimetry based on ^{90}Y activity distributions determined through nuclear medicine imaging.

4.4.2 Porcine Renal Model

The porcine model utilized in this study was a 4-month-old female Landrace-Yorkshire hybrid farm pig weighing 70 kg. Pre-procedural X-ray angiographic imaging (AXIOMArtis, Siemens Healthcare Ltd., Erlangen, Germany) following the administration of an iodine-based vascular contrast agent (ISOVUE-200®, Bracco Diagnostic Inc., Milan, Italy) allowed for the identification of the optimal microsphere administration site within the segmental artery of the left kidney. A 2.5 Fr 0.021" microcatheter placed coaxially within a 4 Fr parent catheter (Cook Medical LLC, Bloomington, IN, USA) was guided to the site where the microspheres were administered. Following administration, the kidney was explanted and flash frozen at -70°C until the time of imaging. The Centre hospitalier de l'Université de Montréal Ethics Committee approved the animal protocol whose data were analyzed for this study.

4.4.3 Micro-CT Imaging

The kidney was imaged with μCT (Triumph X-O, Gamma Medica-Ideas Inc., Los Angeles, CA, USA) using a 92 mm axial FOV and 0.18 mm isotropic voxels. The X-ray tube potential was set to 80 kVp with an exposure of 13 mAs over 512 projections, which were reconstructed using FBP. The embolized arterial vasculature was segmented through voxel intensity thresholding to serve as ^{90}Y source voxels. An external, whole-body (WB) contour was drawn ± 2 cm from the hilum in the cranial-caudal direction as the inferior and superior poles of the kidney were largely void of embolization. A 1 cm-diameter spherical volume was placed in a region of the kidney where no embolization was present to serve as a "normal tissue" VOI, designated as NT. A 2 cm-diameter spherical volume was placed at the centroid of WB to serve as a "target" VOI, designated as T. Figure 4.1 shows both VOIs within WB using a maximum intensity projection displayed in HU for both coronal and sagittal planes. The contours T, WB, and NT are coloured red, green, and magenta, respectively.

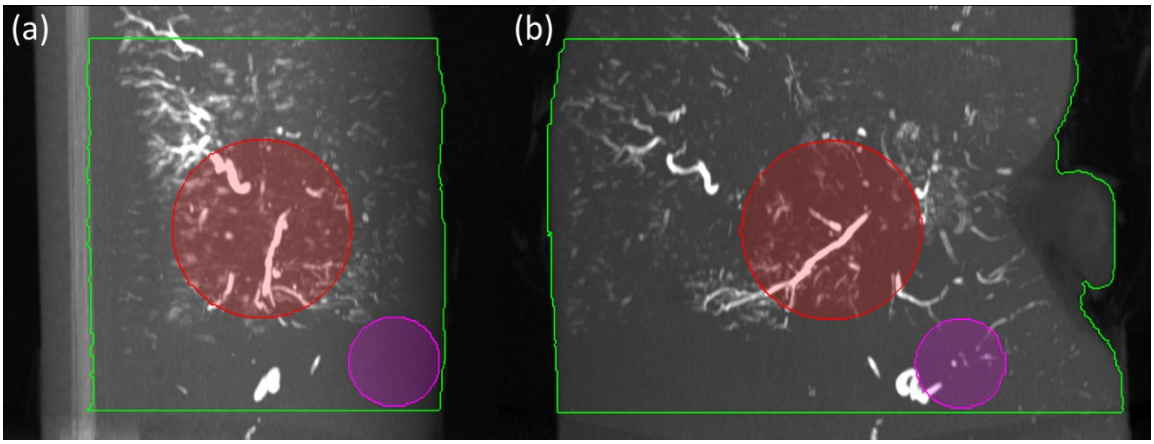

Figure 4.1: VOIs within the kidney shown on a μCT maximum intensity projection [HU: -1000 to 5000]: Red – target, Magenta – normal tissue, Green – whole-body. (a) Sagittal view. (b) Coronal view. The apparent presence of embolized tissue within the normal tissue is due to the projection of the 3D VOI onto a 2D plane.

4.4.4 Activity Distributions

Previous work demonstrated that the intensity of CT image voxels containing radiopaque microspheres increases linearly with microsphere concentration.[157] Based on these findings, 400 MBq of ^{90}Y activity was linearly distributed throughout delineated ^{90}Y source voxels based on voxel intensity. Volume and activity parameters for the VOIs are given in Table 4.1.

Volume of Interest	Volume [mL / % of WB]	Total Activity [MBq / % of WB]
WB	69.16 / 100	400.0 / 100
NT	0.52 / 0.75	0 / 0
T	4.19 / 6.06	19.0 / 4.74

Table 4.1: Volume and activity parameters for the normal tissue, target, and whole-body VOIs.

The high-resolution activity distribution $A_{0.18}$ determined from μCT imaging was down sampled to coarser resolutions using trilinear interpolation to emulate a wide range of nominal resolutions comparable to those encountered in nuclear medicine imaging. In this study, six additional ^{90}Y activity distributions were generated with isotropic voxel sizes of 2.50, 5.00, 7.50, 10.00, 12.50, and 15.00 mm, referred to as $A_{2.50}$, $A_{5.00}$, $A_{7.50}$, $A_{10.00}$, $A_{12.50}$, and $A_{15.00}$, respectively. As microspheres are permanent implants in TARE, the

cumulated activity distribution $\tilde{A}$ was determined by multiplying each activity distribution by the mean lifetime of ^{90}Y.

4.4.5 Monte Carlo Dosimetry

Simulations of ^{90}Y radiation transport were performed using the GATE v9.0 Monte Carlo toolkit installed in Ubuntu 18.04.5 LTS.[158] This version of GATE makes use of Geant4 version 10.06.p01. The Geant4 standard electromagnetic physics package option 4, designed for applications requiring higher accuracy of electron tracking, was used in all simulations. The GATE DoseActor scored dose in a voxelized digital phantom derived from the μCT kidney volume. All voxels within WB were defined as water, voxels outside of WB were defined as air, and source voxels were defined as ^{90}Y. Neither the glass microsphere nor kidney tissue composition were modeled. The ^{90}Y source, incorporating all radioactive decay pathways and atomic de-excitation, was linearly and uniformly distributed amongst segmented μCT voxels. One billion histories (^{90}Y decays) were simulated from the source voxels using a random number generator to randomly sample the ^{90}Y decay pathways. The produced decay products followed particle transport management which is distinguished on several levels: run, track, and step.[159] In the run level, the initialization and termination of each history is managed. The event level governs the simulation of a single history, where each history includes the tracks of the primary and secondary particles created during that history. In the final level, the step size of the history is calculated. Particles were explicitly tracked until they left the μCT kidney geometry or had an energy less than 1 keV. The absorbed dose per interaction was scored in each voxel and the mean absorbed dose per history was calculated from the total dose distribution. No variance reduction techniques were employed in this simulation. This MC-derived dose distribution dd_{MC} served as the ground truth dose distribution. The simulation was performed using two Intel® Xeon® E5-2630 2.30 GHz hexa-core CPUs taking ~80 hours to compute.

4.4.6 Dose-Voxel Kernels

GATE was used to compute ^{90}Y DVKs consisting of isotropic voxels with dimensions of 0.18, 2.50, 5.00, 7.50, 10.00, 12.50, and 15.00 mm, referred to as $DVK_{0.18}$, $DVK_{2.50}$, $DVK_{5.00}$, $DVK_{7.50}$, $DVK_{10.00}$, $DVK_{12.50}$, and $DVK_{15.00}$, respectively. In each of

these simulations, a ^{90}Y source uniformly distributed within a single voxel was placed at the origin of a spherical water phantom and 40 million histories were set to decay in this voxel. Voxels whose center of mass was ≤ 25 mm from the origin were assigned to water and all others were set to air. The mean absorbed dose per history was calculated for each DVK and voxels whose center of mass was > 25 mm were set to zero to ensure application of homogeneous and spherically symmetric DVKs during convolution. All ^{90}Y radiation transport parameters were identical to those used in producing dd_{MC}. The absorbed dose per voxel along cardinal axes in $DVK_{0.18}$ was benchmarked against a MC-derived ^{90}Y dose-point kernel[59] (DPK) with the dosimetric uncertainty expressed as the standard deviation σ_{dose} in the kernel's voxels along the six cardinal axes, as defined by Equation 4.1,

$$\sigma_{dose} = \sqrt{\frac{1}{N-1}\sum_{i=1}^{N}(D_i(r) - \overline{D}(r))^2} \tag{4.1}$$

where $N = 6$ is the number of cardinal axes, r is the radial distance from the origin along each cardinal axis, D_i is the absorbed dose to voxel i, and $\overline{D}$ is the mean dose across voxels from all cardinal axes. The relative statistical uncertainty σ_{stat} in the MC simulation was calculated on a per voxel basis and is defined in Equation 4.2.

$$\sigma_{stat} = \frac{\sqrt{\frac{1}{n-1}\left[\left(\frac{\sum_i d_i^2}{n}\right) - \left(\frac{\sum_i d_i}{n}\right)^2\right]}}{\frac{\sum_i d_i}{n}} \tag{4.2}$$

Here, d_i is the energy deposited in a voxel and n is the number of interactions within the voxel.

4.4.7 Convolutional Dosimetry

For a non-uniform radioisotope activity distribution in an infinite, homogeneous medium, the absorbed dose distribution D can be determined by convolving $\tilde{A}$ with a DVK according to Equation 4.3,

$$D(x,y,z) = \sum_{x'}\sum_{y'}\sum_{z'} \tilde{A}(x',y',z') * DVK(x-x', y-y', z-z') \qquad 4.3$$

where $\tilde{A}$ is the cumulative radionuclide activity distribution and DVK is the spatially invariant kernel that describes the absorbed dose in each voxel from disintegrations in the source voxel. Convolution of the cumulative ^{90}Y activity distributions with their corresponding ^{90}Y kernels was performed in the frequency domain with the fast Fourier transform to produce $dd_{0.18}$, $dd_{2.50}$, $dd_{5.00}$, $dd_{7.50}$, $dd_{10.00}$, $dd_{12.50}$, and $dd_{15.00}$, corresponding to dose distributions with voxels sizes of 0.18, 2.50, 5.00, 7.50, 10.00, 12.50, and 15.00 mm, respectively. Convolution calculations were performed in MATLAB R2020b (MathWorks Inc., Natick, MA, USA).

4.4.8 Statistical Analysis

Dosimetric evaluations of the VOIs within the kidney volume were compared using several standard dose metrics, including the minimum dose D_{min}, median dose D_{med}, maximum dose D_{max}, mean dose D_{μ}, and standard deviation σ. The coefficient of variation (COV) is defined as σ/D_{μ}. Metrics were expressed using the generic format $d^{Metric}_{VOI_{Resolution}}$. For example, the mean dose D_{μ} to the tumour T in the 2.5 mm voxel dose distribution $dd_{2.5}$ is $d^{\mu}_{T_{2.5}}$. Cumulative dose-volume histograms (cDVHs) were also calculated for all VOIs to characterize the dose distributions and extract the minimum dose to 70% and 1% of the entire volume, D_{70} and D_1, respectively. The correlation between dose metrics and image voxel size was quantified using the coefficient of determination r^2. Dose distributions were displayed using MIM Software v6.9.4 (MIM Software Inc., Cleveland, OH, USA).

4.5 Results

4.5.1 Dose-Voxel Kernels

Mean DVK profiles along cardinal axes are compared against a previously published ^{90}Y DPK in Figure 4.2, where the error bars corresponds to the dosimetric error defined in Equation 4.1.[59] Central voxel values of the DVKs differ by orders of magnitude relative to the DPK due to the use of concentric dose scoring shells surrounding a singularity opposed to a voxelized 3D grid surrounding a finite-sized source voxel. Statistical errors in the central voxel of all DVKs, as defined in Equation 4.2, are between 0.016% and 0.011%.

Beyond the central voxel, the reference DPK shows excellent agreement with $DVK_{0.18}$. However, as the DVK voxel size increases, the larger voxels begin to underestimate the dose near the origin and over-estimate the dose at greater radial distances. Ignoring bremsstrahlung losses, the total energy deposited remains constant as the same number of decay events (40 million) were generated for each DVK.

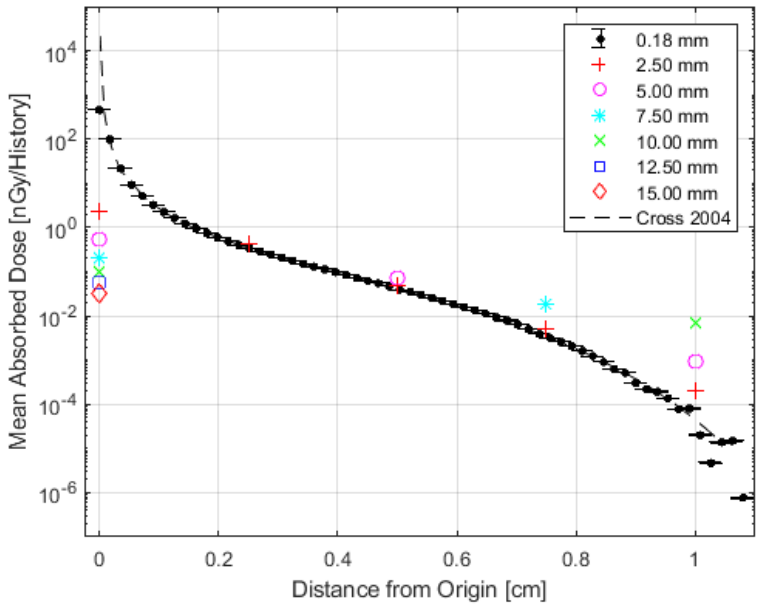

Figure 4.2: ^{90}Y DVK profiles averaged across the six cardinal axes compared against a reference DPK profile extending to a ^{90}Y β^- particle range of 11.0 mm.

Figure 4.3 presents 2D and 3D representations of ^{90}Y DVKs for three cases: $DVK_{0.18}$, $DVK_{2.50}$, $DVK_{10.00}$. Figure 4.3 shows 3D surface plots through the central slice (a,c,e) and 2D cross-sections of the central slice (b,d,f).

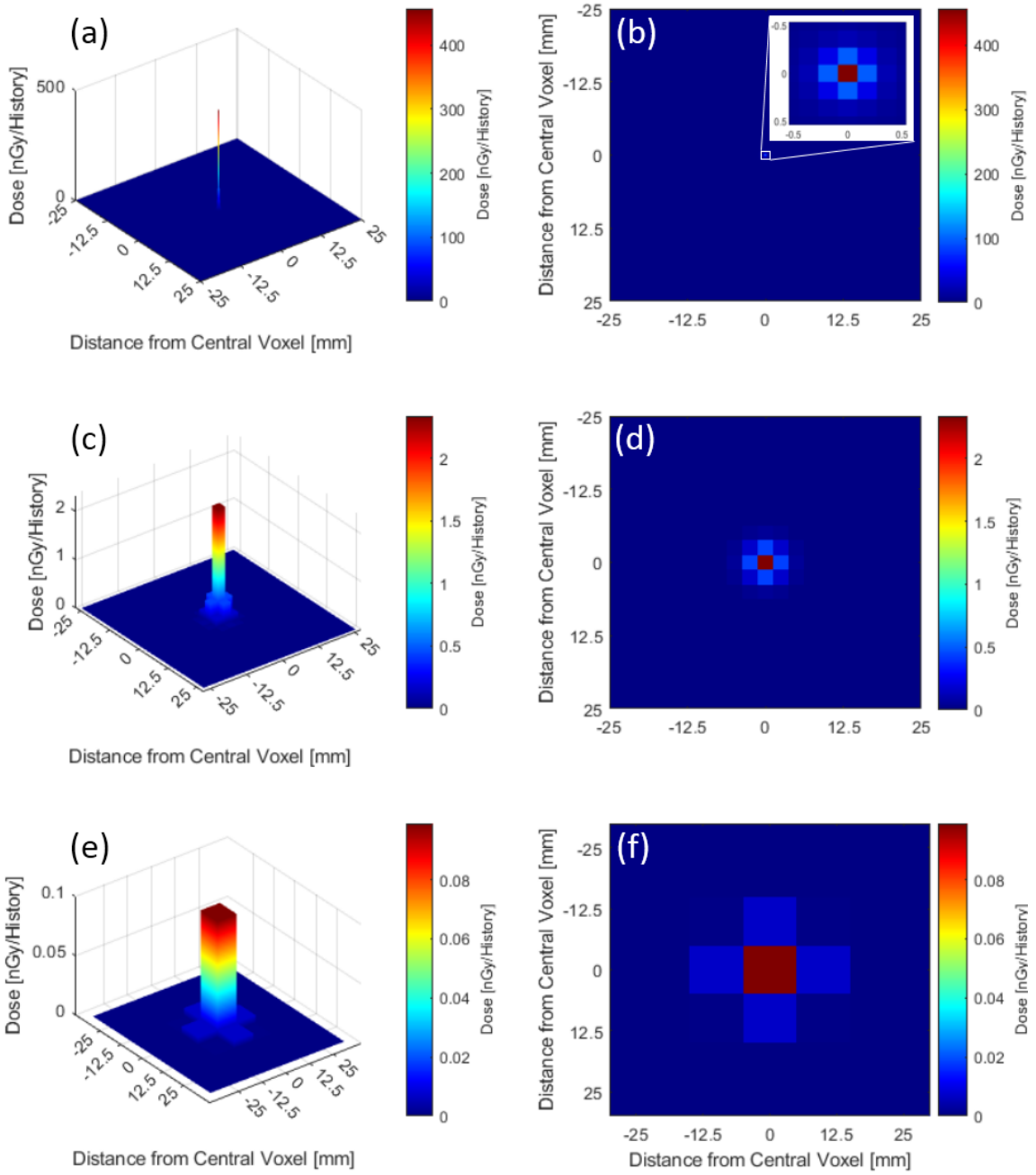

Figure 4.3: (a,c,e): 3D surface plots of $DVK_{0.18}$, $DVK_{2.50}$, $DVK_{10.00}$ through the central slice. (b,d,f): 2D cross-section of $DVK_{0.18}$, $DVK_{2.50}$, $DVK_{10.00}$ through the central slice.

4.5.2 Dose Distributions

For a qualitative assessment of the ^{90}Y dose distributions, a common axial slice from all dose distributions is shown in Figure 4.4. Qualitatively, it is difficult to distinguish dd_{MC} from $dd_{0.18}$ except in low dose regions where the statistical variations in dd_{MC} become apparent. Although hot spots exceeding 2000 Gy present in the tumour VOIs in dd_{MC} and $dd_{0.18}$ are still discernable in $dd_{2.50}$, their maximum intensity is drastically reduced through volume-averaging. Conversely, voxels void of dose in the hilum in the right-hand side of Figure 4.4(a-d) are no longer nonzero in $dd_{7.50}$, $dd_{10.00}$, $dd_{12.50}$, and $dd_{15.00}$ as volume-averaging results in an increasingly homogeneous dose distribution.

Quantitively, $d^{\mu}_{T_{MC}}$= 245 ± 511 Gy, $d^{min}_{T_{MC}}$ = 0 Gy, and $d^{max}_{T_{MC}}$ = 10,041 Gy. The percent difference of $d^{\mu}_{T_{0.18}}$ relative to $d^{\mu}_{T_{MC}}$ is -1.0%. In the remaining dose distributions, D_{μ} differs from $d^{\mu}_{T_{MC}}$ by -5.7% to 5%, suggesting that the mean dose in this macroscopic, embolized volume can be ascertained with reasonable confidence independent of the image resolution. Changes in the metric D_{70} are more sensitive to changes in the spatial resolution of the dose distributions. The percent difference of $d^{70}_{T_{0.18}}$ relative to $d^{70}_{T_{MC}}$ is -1.2%, while the relative percent difference between $d^{70}_{T_{MC}}$ and D_{70} to T within the remaining dose distributions ranges from 40.6% to 299.5%. The percent difference of $d^{1}_{T_{0.18}}$ relative to $d^{1}_{T_{MC}}$ is -0.8%, while the percent differences between $d^{1}_{T_{MC}}$ and D_1 to T within the remaining dose distributions ranges from -38.2% to -89.8%.

Figure 4.5 shows an axial slice through the centroid of NT in all dose distributions. This VOI is largely void of dose in Figure 4.5(a,b), with $d^{max}_{NT_{MC}} = 3.2\ Gy$ and $d^{max}_{NT_{0.18}}$= 1.3 Gy. The dose distributions $dd_{2.50}$ and $dd_{5.00}$ in Figure 4.5(c,d) show the effect of dose spill-in from embolized tissue outside of NT, although there remain voxels within the VOI that are void of dose, i.e. $d^{min}_{NT_{2.50}}$= 0 Gy and $d^{min}_{NT_{5.00}}$= 0 Gy. The minimum dose to NT becomes nonzero for $dd_{7.50}$, $dd_{10.00}$, $dd_{12.50}$, and $dd_{15.00}$ while the maximum dose to NT is $d^{max}_{NT_{12.50}}$= 214.5 Gy. Dose metrics for T and NT from all dose distributions shown in Figure 4.4 and Figure 4.5 are listed in Table 4.2 and Table 4.3, respectively. All units in Table 4.2 and Table 4.3 are in Gy, except for the unitless COV.

.

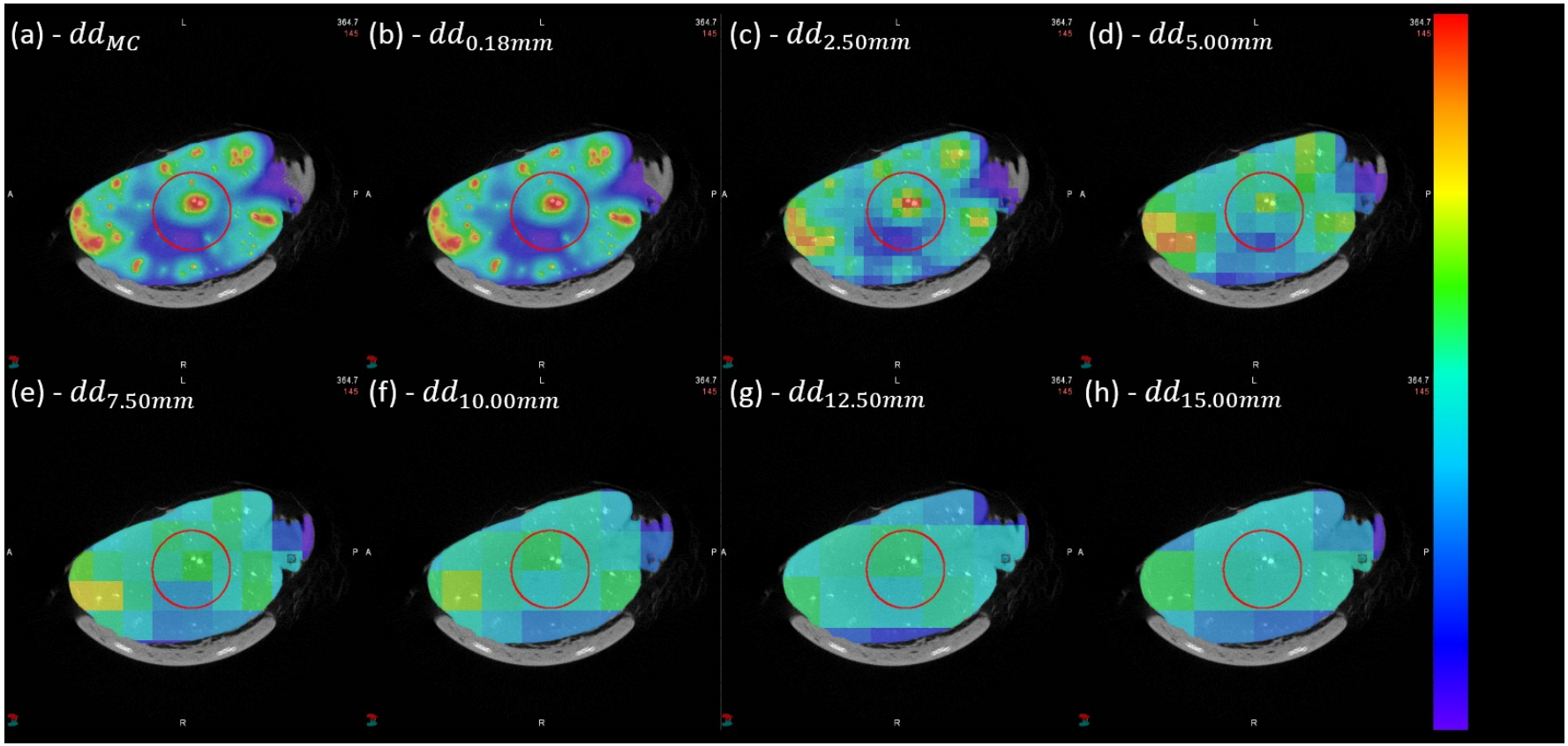

Figure 4.4: Axial fusion of µCT and dose distributions containing planar contours of the target (Red) [HU: 0 to 1500]. (a) dd_{MC} (b) $dd_{0.18}$ (c) $dd_{2.50}$ (d) $dd_{5.00}$ (e) $dd_{7.50}$ (f) $dd_{10.00}$ (g) $dd_{12.50}$ (h) $dd_{15.00}$.

Isotropic Voxel Size [mm]	D_{μ}	σ	COV	D_{70}	D_1	D_{min}	D_{med}	D_{max}
MC (0.18)	245.3	511	2.08	55.3	2556.1	0.1	107.8	10041.0
0.18	242.9	507	2.09	54.6	2534.4	1.3	106.5	9928.1
2.50	239.8	322	1.34	77.8	1580.1	2.0	136.7	1978.6
5.00	257.5	241	0.94	142.9	775.7	13.0	191.5	967.4
7.50	254.5	185	0.73	189.7	584.6	34.5	193.9	747.8
10.00	236.7	167	0.71	170.9	363.0	65.7	207.8	533.7
12.50	251.2	124	0.50	214.0	323.2	96.1	251.5	773.0
15.00	231.4	54	0.23	220.9	260.0	92.0	256.6	275.7

Table 4.2: Dose metrics for the target across all dose distributions. All units are in Gy, except the unitless COV.

Isotropic Voxel Size [mm]	D_{μ}	σ	COV	D_{70}	D_1	D_{min}	D_{med}	D_{max}
MC (0.18)	0.0	0.1	-	0.3	1.0	0.0	0.0	3.2
0.18	0.0	0.1	8.00	0.3	1.0	0.0	0.0	1.3
2.50	0.2	0.5	3.40	0.3	3.3	0.0	0.1	9.9
5.00	1.7	2.1	1.27	0.8	10.9	0.0	1.2	24.2
7.50	13.2	22.3	1.68	3.5	95.0	1.2	1.7	95.5
10.00	22.9	13.8	0.60	15.2	48.0	8.1	15.9	48.8
12.50	35.9	43.4	1.21	14.0	167.1	13.4	17.3	214.5
15.00	47.3	8.1	0.17	43.0	55.0	43.9	26.0	182.1

Table 4.3: Dose metrics for normal tissue across all dose distributions. All units are in Gy, except the unitless COV.

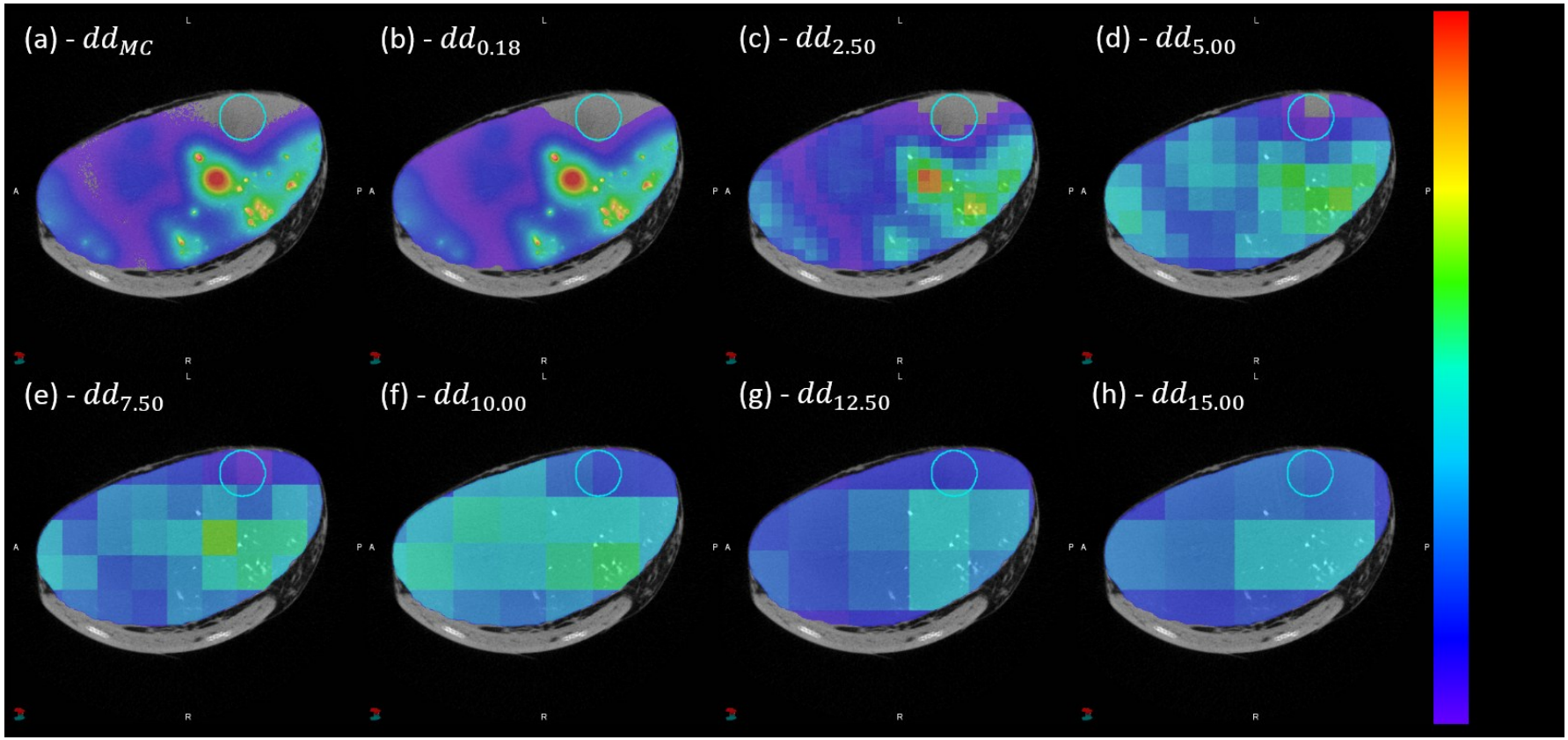

Figure 4.5: Axial fusion of μCT and dose distributions containing planar contours of the normal tissue (Cyan) [HU: 0 to 1500]. (a) dd_{MC} (b) $dd_{0.18}$ (c) $dd_{2.50}$ (d) $dd_{5.00}$ (e) $dd_{7.50}$ (f) $dd_{10.00}$ (g) $dd_{12.50}$ (h) $dd_{15.00}$.

Dose metrics for T from the convolution-based dose distributions are plotted as a function of image voxel size in Figure 4.6. The relationship between D_{70} and voxel size is well described by a linear fit ($r^2 = 0.897$). D_{μ} was found to be independent of voxel size as demonstrated by an insignificant correlation ($r^2 = 0.066$). Tumour hot spot (D_1), however, had a non-linear relationship with voxel size. The magnitude of the hotspot decreased rapidly with increasing voxel size between 0.18 mm and 5.00 mm voxels. For larger voxels, the hotspot continues to decrease, but at a slower rate. The homogeneity of the absorbed dose can be expressed by the COV which is given in Table 4.2. For T, the COV is a monotonically decreasing function of the voxel size, i.e. convolution-based distributions with larger voxel sizes have consistently more homogeneous dose distributions.

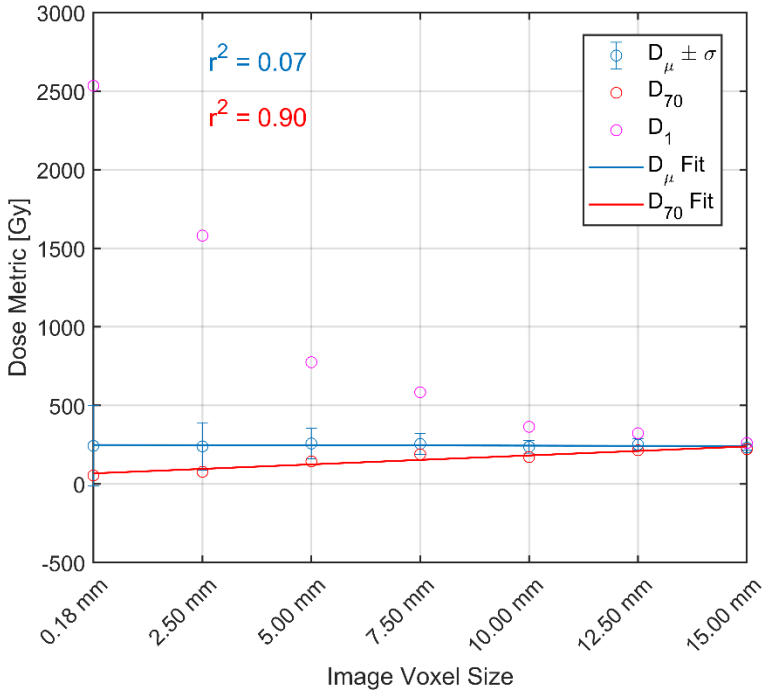

Figure 4.6: $D_{\mu} \pm \sigma$, D_{70} , and D_1 as a function of image voxel size for the target for all convolution-based dose calculations. Coefficients of determination are provided for both linear fits.

4.5.3 Dose Profiles

Dose profiles from an example, non-homogeneous axial slice are shown in Figure 4.7(a) and Figure 4.7(b) for a continuous line segment through WB hot spots, illustrated in

Figure 4.7(c). The same dose peaks and troughs are clearly discernable in both dd_{MC} and $dd_{0.18}$, although differences exist between the two profiles due to statistical variations in dd_{MC}. The maximum dose values along the profiles in dd_{MC} and $dd_{0.18}$ are 5,356 Gy and 5,313 Gy, respectively. Although these dose peaks are present in $dd_{2.50}$, the magnitudes of each peak are drastically reduced with a maximum value of only 1761 Gy, a factor of ~3 less than the maximum in dd_{MC}.The remaining dose distributions have maxima ≤ 1000 Gy and the appearance of the dose peaks and troughs present in dd_{MC} begin to become imperceptible. The dose distribution $dd_{15.00}$ produces the most homogeneous profile with values ranging from 18 to 532 Gy.

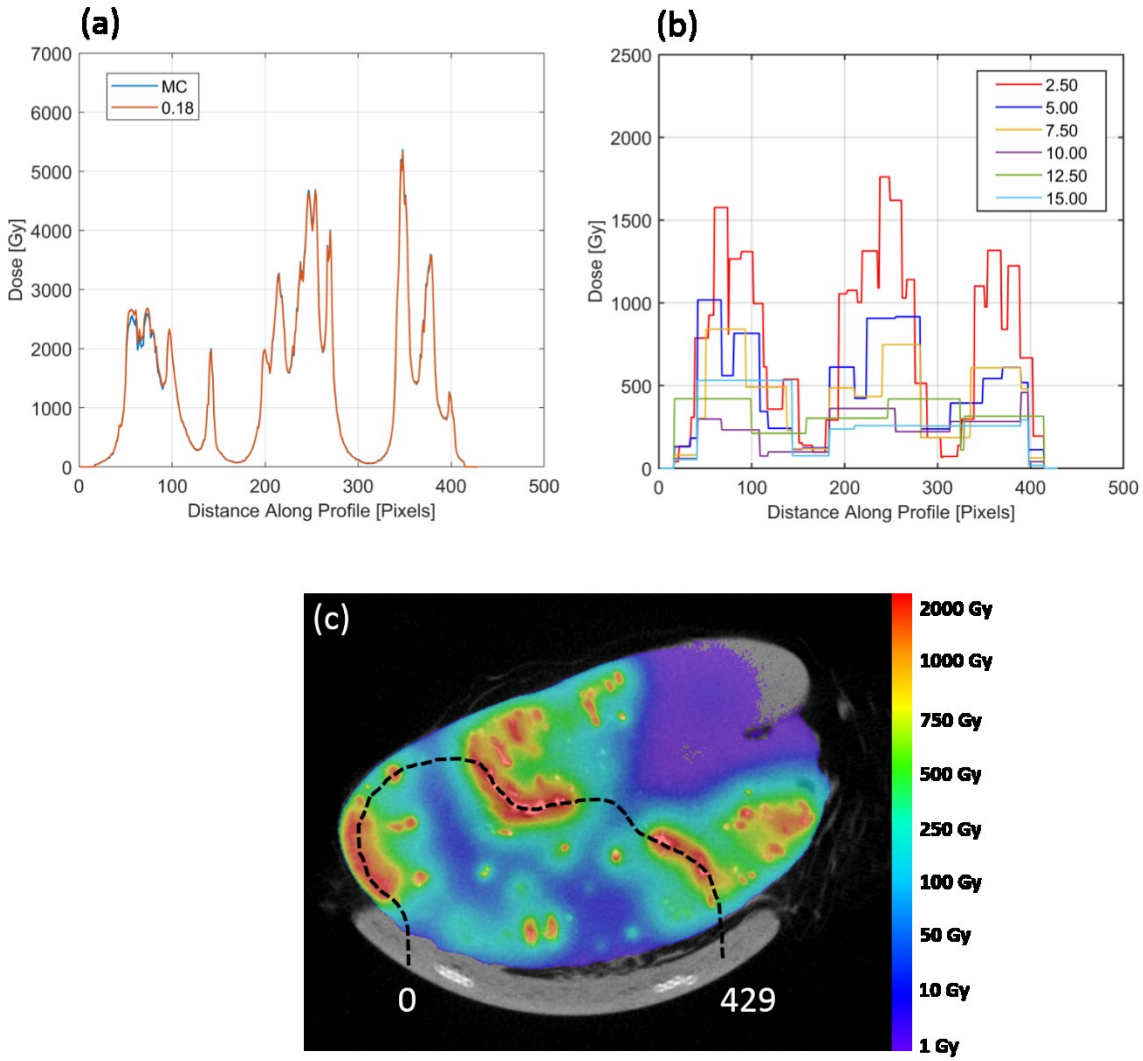

Figure 4.7: Continuous dose profile through all dose distributions. (a) dd_{MC} and $dd_{0.18}$ (b) $dd_{2.50}$, $dd_{5.00}$, $dd_{7.50}$, $dd_{10.00}$, $dd_{12.50}$, and $dd_{15.00}$. (c) Axial slice from dd_{MC} demonstrating the path of the dose profile (dotted black).

4.5.4 Dose-Volume Histograms

Figure 4.8 shows cDVHs for T and NT for all dose distributions. For dd_{MC} and $dd_{0.18}$, the cDVHs in Figure 4.8(a) are in excellent agreement, as verified in the dose profiles of Figure 4.7(a) and the axial dose distributions in Figure 4.4(a) and Figure 4.4(b). As the voxel size is increased, the shoulder region (shown within the inset of Figure 4.8(a)) of the cDVHs becomes more pronounced, which falsely indicates an increased minimum dose to the entire volume of T. Furthermore, the tails (high dose regions) of the cDVHs are no longer present. These combined effects produce a more homogeneous dose distribution

across T. For NT, as the voxel size is reduced, the curves in Figure 4.8(b) become less steep with increased maximum values.

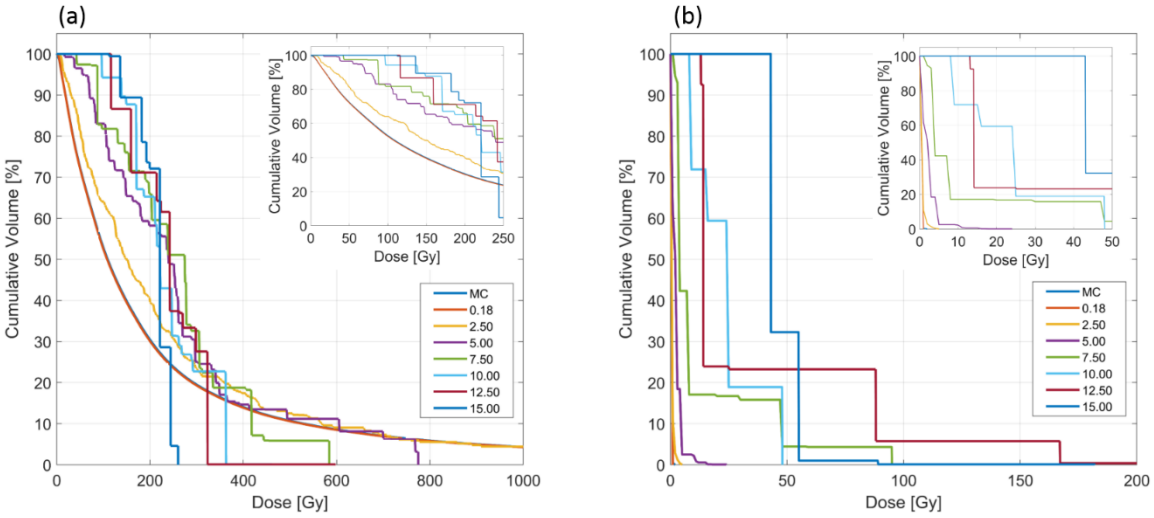

Figure 4.8: Cumulative dose-volume histograms for the (a) target (b) normal tissue. The insets in (a) and (b) show the histograms with a dose scale reduced by a factor of four to better observe the shoulder region.

4.6 Discussion

4.6.1 Activity Distributions

TheraSphere microspheres are available in six standard activity vials ranging from 3 to 20 GBq (at time of calibration) containing ~1.2 to ~8 million microspheres, respectively.[52] The physician can customize the microsphere specific activity by choosing which activity vial to be used based on the desired quantity of microspheres and activity to be administered at time of treatment. For radiopaque microspheres, the specific activity will directly impact the number of administered microspheres, consequently influencing the CT image contrast and microsphere visibility. A lower specific activity microsphere, for example, requires the administration of an increased number of microspheres (improved visibility) to achieve a target dose. However, there is an upper limit on the number of microspheres that should be administered in TARE to avoid potential healthy tissue toxicity and microsphere reflux into surrounding healthy tissue.[160,161]

Accurately defining the ^{90}Y activity distribution is essential as any errors associated with the activity will propagate into dosimetric errors. A standardized methodology should

be implemented in order to accurately quantify the ^{90}Y activity with post-administration CT. Equipped with knowledge of the microsphere's specific activity at the time of administration, a calibration phantom with known concentrations of radiopaque microspheres could be imaged and analyzed to relate HU to the microsphere concentration, hence ^{90}Y activity, within a CT voxel. For this purpose, an experimental calibration phantom was designed. An axial CT slice of this phantom, acquired from a clinical CT scanner (Optima CT580 RT, GE Healthcare, Chicago, IL, USA), is shown in

Figure *4.9*(a). For three microsphere concentrations of 0.5 mg/mL (green), 5.0 mg/mL (red), and 25.0 mg/mL (blue), there are nine cylinders with diameters ranging from 2 mm to 15 mm to further examine the effect of cylinder size on quantification accuracy. An additional VOI (magenta) was placed at the center of the phantom to quantify the HU of the solid, uniform background region. The calibration curve in

Figure *4.9*(b) was calculated through a linear least-squares fit of the average HU the microsphere concentration within the VOIs. This calibration curve was collected at a tube potential of 100 kVp and demonstrates strong linearity ($r^2 > 0.999$) of CT voxel values across the investigated microsphere concentrations. It has also been shown that HU quantification accuracy can be influenced by CT scanner manufacturer, hence the calibration phantom should be imaged at each institution using the same CT scanner and image acquisition parameters employed in post-administration CT imaging of a patient.[150]

The International Organization for Standardization defines the LOD as the net concentration of a component in a material that will lead to the conclusion that the concentration of analyzed component is greater than that of a control sample.[144] This method has been successfully implemented in identifying the minimum detectable iodine concentration in anthropomorphic phantoms[162] and can also be applied in the analysis of these calibration phantoms to determine the minimum detectable radiopaque microsphere concentration in a CT voxel. Inherent noise within a CT voxel can further reduce the confidence with which an activity level can be attributed to a voxel with a given HU value, which in turn will place a limit on the confidence with which low dose levels can be quantified.

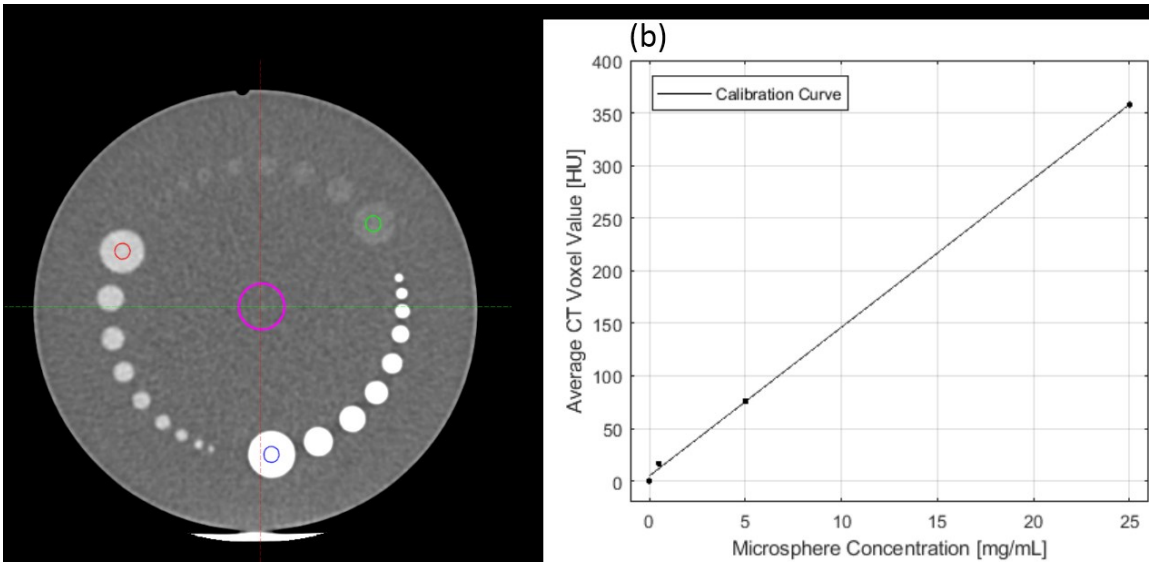

Figure 4.9: (a) Clinical CT slice of a calibration phantom containing a uniform background region (magenta) and three microsphere concentrations: 0.5 mg/mL (green), 5.0 mg/mL (red), and 25.0 mg/mL (blue). There are nine cylinders per concentration having diameters ranging from 2 mm to 15 mm (b) Calibration curve with coefficient of determination $r^2 > 0.999$. Average voxel values were extracted for the largest cylinders only.

4.6.2 Monte Carlo Dosimetry

Particle transport through the kidney was performed assuming the kidney tissue was composed entirely of water. Although the density of kidney tissue (1.066 g/mL) is slightly greater than that of water (1.000 g/mL), this is unlikely to have a significant effect in the absorbed dose calculation. A recent study comparing ^{90}Y DPK values between water and liver tissue (1.079 g/mL) has shown that relative mean differences are between 0.6 ± 0.1% and 2.0 ± 0.1%.[163] These differences are unlikely to be clinically relevant.

The elemental composition of the microspheres was not considered during ^{90}Y particle transport within the kidney. If one assumes a typical microsphere concentration of 254 ± 18 MS/mm^3 at the tumour-normal tissue interface[91] and a microsphere volume of 1.41 x 10^{-5} mm^3 (30 µm diameter), then 0.36% of a 1 mm^3 volume would consist of microspheres. Although there are higher microsphere concentrations in some of the ^{90}Y source voxels in this study, at a typical concentration of 254 ± 18 MS/mm^3, the material designation of water for source voxels within WB is justified.

A MC simulation was performed only for the nominal voxel size of the acquired μCT data. A comparison of the MC simulation results with those of the DVK dosimetry method, using the same voxel size (0.18 mm), shows negligible differences between dose metrics, DVHs, and dose profiles. As MC simulations were not performed for the larger voxel sizes, no ground truth comparison was made for $dd_{2.50}$, $dd_{5.00}$, $dd_{7.50}$, $dd_{10.00}$, $dd_{12.50}$, and $dd_{15.00}$. However, a recent study was conducted for post-administration dosimetry of 17 TARE patients through ^{90}Y bremsstrahlung SPECT imaging with an isotropic voxel size of 4.8 mm.[164] The authors determined the DVK-based mean absorbed dose to the tumour and normal liver differed by < 5% relative to their corresponding MC mean dose, which was calculated using the same activity distribution and voxel size. In another study, MIRD S-values were used to perform post-administration dosimetry, and these results were also compared to MC simulation results.[165] The activity distribution was estimated through ^{99m}Tc-MAA SPECT imaging with voxel sizes of 3.0 mm and 6.0 mm.[166] Authors concluded that performing the MC simulation using the SPECT-derived activity distribution produced dosimetric results similar to the SPECT-derived distribution alone, with differences likely due to different material composition of the phantom in their MC simulation. Based on these results, we can conclude that differences in the dose metrics of our study are likely due to the change in voxel size and are not a result of the limitations of convolutional dosimetry.

4.6.3 Dosimetric Analysis

The mean tumour dose is the most common dose metric reported in the literature.[167] According to the MIRD methodology[115], the mean absorbed dose D_{MIRD} to a target is given by Equation 4.4,

$$D_{MIRD} = \frac{A_0 \cdot 50}{M} \tag{4.4}$$

where A_0 is the administered ^{90}Y activity in GBq and M is the mass of the target in kg. Given the administered activity and tumour volume in Table 4.1 and assuming a tissue density of 1.0 g/mL, the tumour mass can be determined. Using these values as inputs into Equation 4.4, the dose to T is 226.7 Gy, which is underestimated by 7.6% when compared to the ground truth result $d^{\mu}_{T_{MC}} = 245.3\ Gy$. Equation 4.4 also fails to capture any

inhomogeneity in attempting to understand the significant variability in clinical outcomes as a function of tumour dose observed in TARE.

The mean tumour dose is expected to be equivalent when implementing any voxel-based dosimetry formalism as long as the ^{90}Y activity within the VOI is consistent across imaging modalities. A recent study compared quantitative SPECT and non-TOF PET imaging of ^{90}Y patients and showed that, when corrected for photon scatter, attenuation, and collimator response, quantitative SPECT and non-TOF PET have a mean activity difference of 0 ± 9%, despite a substantial change in voxel size.[168] Another patient study comparing TOF PET and SPECT, also corrected for scatter, attenuation, and collimator response, demonstrated that the mean absorbed dose determined by PET and SPECT varied by no more than 4 Gy in low dose regions within the liver, again, despite a large difference in voxel size.[169] The expectation of an equivalent mean tumour dose is valid assuming only the spatial resolution of the imaging system changes. The absorbed dose calculation is dependent on other factors including, but not limited to, the image reconstruction algorithm[170], energy window[81], and collimator type.[171]

High-resolution dose distributions derived from CT imaging allow for the calculation of cDVHs to extract other useful metrics, such as D_{70}, that have been shown to correlate with clinical outcomes.[105,172,173] However, this study has demonstrated that D_{70} is also correlated with the voxel size of the imaging modality (r^2 = 0.897) with a range of 165.5 Gy between the ground truth dose distribution dd_{MC}, and the dose distribution with the largest voxel size, $dd_{15.00}$. For example, if we imaged the renal model in this study with clinical CT using a standard abdominal voxel volume of 0.625 mm^3, Figure 4.6 would suggest D_{70} = 76.3 Gy. This value overestimates the ground truth equivalent $d_{T_{MC}}^{70}$= 55.3 Gy by 21.0 Gy, but it is still a substantial improvement when compared to $d_{T_{15.00mm}}^{70}$= 220.9 Gy.

Implementing high-resolution imaging modalities for post-administration dosimetry would provide the most accurate representation of extracted dose metrics, which could lead to an improved understanding of the dose-response relationship in ^{90}Y TARE. A review of recent dose-response studies for patients receiving TheraSphere microspheres shows that the reported mean dose required to elicit a tumour response varies by 500

Gy.[62,167] This work suggests that D_{μ} may not be the most appropriate parameter in defining the dose-response relationship. Additional research is needed to accurately refine the dose metrics used to establish the dose-response relationship in ^{90}Y TARE.

4.7 Conclusion

High-resolution μCT imaging of *in vivo* radiopaque microsphere distributions can provide increased confidence in characterizing the absorbed dose heterogeneity in ^{90}Y TARE relative to dosimetry based on nuclear medicine imaging. Precise knowledge of the absorbed dose distribution in ^{90}Y TARE is essential for identifying undertreated tumour volumes, identifying radiation toxicity in adjacent healthy tissue, and developing NTCP and TCP models to establish precise tumour dose and healthy tissue toxicity thresholds.

Chapter 5 Manuscript 3: Precision Dosimetry in Yttrium-90 Radioembolization through CT Imaging of Radiopaque Microspheres in a Rabbit Liver Model

5.1 Prologue

The following manuscript provides a first comparison of CT- and PET-based dosimetry in ^{90}Y TARE. The results from this work demonstrate the benefits of CT-based dosimetry, which include improved visualization of the dose distribution, reduced partial volume effects, and a better representation of dose heterogeneity allowing for the extraction of more accurate dose-volume metrics. Effects of respiratory motion are also mitigated when compared to ^{90}Y PET imaging.

The manuscript was accepted for publication in the *European Journal of Nuclear Medicine & Medical Imaging – Physics*. The reference is provided below.

- Henry, C., Strugari, M., Mawko, G., Brewer, K., Abraham, R., Liu, D., Gordon, A., Bryan, J., Kappadath, S., Syme, A. (2021). Precision Dosimetry in Yttrium-90 Radioembolization through PET/CT Imaging of Radiopaque Microspheres in a Rabbit Liver Model. *European Journal of Nuclear Medicine & Medical Imaging - Physics. DOI: 10.21203/rs.3.rs-806070/v1*

5.2 Abstract

Purpose: To perform precision dosimetry in ^{90}Y TARE through CT imaging of radiopaque microspheres in a rabbit liver model, and to compare extracted dose metrics to those produced from conventional PET-based dosimetry.

Methods: A CT calibration phantom was designed to contain posts having nominal microsphere concentrations of 0.5 mg/mL, 5.0 mg/mL, and 25.0 mg/mL. The mean HU was extracted from the post volumes to generate a calibration curve to relate HU to microsphere concentration. A nominal bolus of 40 mg of microspheres was administered to the livers of eight rabbits followed by PET/CT imaging. A CT-based activity distribution was calculated through the application of the calibration curve to the CT liver volume.

Post-treatment dosimetry was performed through the convolution of ^{90}Y DVKs and the PET- and CT-based cumulated activity distributions. The mean dose to the liver in PET- and CT-based dose distributions was compared through linear regression, ANOVA, and Bland-Altman analysis.

Results: A linear least-squares fit to the average HU and microsphere concentration data in the calibration phantom confirmed a strong correlation ($r^2 > 0.999$) with a slope of 14.13 HU/mg/mL. A poor correlation was found between the mean dose derived from CT and PET ($r^2 = 0.374$) while the ANOVA analysis revealed statistically significant differences ($p < 10^{-12}$) between the MIRD-derived mean dose and the PET- and CT-derived mean dose. Bland-Altman analysis predicted an offset of 15.0 Gy between the mean dose in CT and PET. The dose within the liver was shown to be more heterogeneous in CT than in PET with an average coefficient of variation equal to 1.99 and 1.02, respectively.

Conclusion: The benefits of a CT-based approach to post-treatment dosimetry in ^{90}Y TARE include improved visualization of the dose distribution, reduced partial volume effects, a better representation of dose heterogeneity, and the mitigation of respiratory motion effects. Post-treatment CT imaging of radiopaque microspheres in ^{90}Y TARE provides the means to perform precision dosimetry and extract accurate dose metrics used to refine the understanding of the dose-response relationship, which could ultimately improve future patient outcomes.

5.3 Introduction

World-wide, HCC is the sixth most frequently diagnosed cancer in men and the ninth in women with more than 906,000 new cases each year.[12] It is responsible for the third most frequent cause of cancer related deaths and is one of a small number of cancers with a growing rate of incidence, particularly in Europe and North America where there have been historically low rates of incidence.[12] Although liver transplant or surgical resection are considered the most effective treatments, 95% of patients are diagnosed after the disease has progressed beyond the point where these treatments are an option.[32,36,47,174] For many of these patients, embolic therapies may prolong life expectancy.[174]

^{90}Y TARE – indicated for primary and metastatic liver cancer – is a radiation-based embolic therapy that has been integrated into clinical practice for more than 20 years.[46] In

TARE, ^{90}Y-labeled microspheres are administered into the hepatic arterial vasculature to preferentially target liver tumours while sparing the surrounding liver parenchyma. This preferential uptake is achieved by exploiting the process of tumour tissue angiogenesis, resulting in tumoural vascular inflow derived exclusively from the hepatic artery while the healthy liver parenchyma receives approximately 80% of its vascular inflow from the portal vein.[31] The liver's dual blood supply is exploited to overcome the inherent limitation of EBRT – the irradiation of healthy tissue when treating the intended target.

The two commercially available microspheres are TheraSphere® glass microspheres (Boston Scientific Corp., Marlborough, MA, USA) and resin-based SIR-Spheres® microspheres (Sirtex Medical Inc., Woburn, MA, USA). As a therapeutic agent, both microspheres employ ^{90}Y – a pure β^- emitter that decays to ^{90}Zr with a physical half-life of 64.24 ± 0.30 hours (2.7 days), achieving 95% decay of the radioactivity within 11.5 days.[58] Maximum and average β^- energies are 2.2787 ± 0.0013 MeV and 0.9267 ± 0.0008 MeV, respectively, corresponding to a range in water of 11.0 mm and 2.4 mm.[59,60] The therapeutic range X_{90} in water is 5.4 mm, where X_{90} is defined as the radius of a sphere containing 90% of the absorbed dose.[61]

With this localized energy deposition, the microsphere spatial distribution within the tumour plays a critical role in determining the absorbed dose. It has been previously demonstrated that microsphere distributions observed in *ex vivo* tissue samples can be highly heterogeneous with a wide range of microsphere cluster sizes.[54,90,91,175] Furthermore, microspheres preferentially accumulate in the tumour's periphery and tend to remain localized within the portal tracts of the liver's vasculature.[175,176] These combined effects result in a highly heterogeneous dose distribution. To demonstrate, Roberson *et al*. estimated that in a small tumour nodule, the minimum tumour dose was less than half of the average dose.[90] A study performed by Kennedy *et al*. found that a TheraSphere administration intended to deliver a nominal dose of 150 Gy actually delivered doses between 100 and 8000 Gy, although only a small fraction of the volume received a dose exceeding 1000 Gy.[54] Cremonesi *et al*. later demonstrated the dose rate around a point source of ^{90}Y varied by approximately five orders of magnitude over a distance of only 2 mm.[177]

To facilitate patient-specific estimates of the absorbed dose, post-treatment ^{90}Y PET and bremsstrahlung SPECT imaging can approximate the ^{90}Y activity distribution. Voxel-based dosimetry formalisms can then be employed to calculate the absorbed dose distribution.[100] Accumulated evidence from retrospective dose-response studies in ^{90}Y TARE for the treatment of HCC with TheraSphere microspheres suggests a positive correlation between absorbed dose and tumour response, but the range of reported dose thresholds varies by a full order of magnitude.[101] Some variance in the data may be attributed to tumour size, follow-up time, response assessment criteria, and the heterogeneity of study design, however, the poor spatial resolution of ^{90}Y PET and bremsstrahlung SPECT arguably poses the most significant limitation to accurately quantifying dose thresholds for the prediction of toxicity, response, and survival in ^{90}Y TARE.[62] The spatial resolution, as measured by the FWHM**,** is reported to lie between 5.0 and 10.0 mm in ^{90}Y PET imaging and between 7.0 and 30.0 mm in bremsstrahlung SPECT imaging.[9–11] In either case, the resolution is insufficient to accurately estimate the true ^{90}Y activity distribution as the FWHM is consistently greater than the average ^{90}Y β^- emission range (2.4 mm) and orders of magnitude greater than the distance scale (microns) over which changes in microsphere concentration take place.[54,91] This limitation results in the blurring of the true ^{90}Y activity distribution, which will diminish variations in the absorbed dose and incorrectly yield a more homogeneous dose distribution. Consequently, there exists an unmet clinical need to provide substantially higher spatial resolution imaging of microsphere distributions to facilitate high-accuracy, high-precision dosimetry in ^{90}Y TARE.

CT-based imaging can provide significantly enhanced spatial resolution imaging relative to PET and bremsstrahlung SPECT imaging, but CT-based evaluations of commercial microspheres are not performed as the microspheres lack sufficient radiopacity for their visualization to be of clinical use.[38,156] Fortunately, a preclinical radiopaque microsphere product called Eye90 microspheres™ has recently been developed by ABK Biomedical (Halifax, NS, Canada). By virtue of the high atomic numbers of the elements within the material composition of these microspheres, they provide substantial radiopacity which permits high-resolution CT imaging to visualize the microspheres' spatial

distribution. This accurate portrayal of the microsphere's spatial distribution, and hence ^{90}Y activity distribution, enables precise CT-based dosimetry.[178] Furthermore, due to the fast scan time of CT relative to PET, uncertainties attributed to respiratory motion during the PET image acquisition can be effectively eliminated in CT as acquisitions can be performed with a breath hold technique.

Beyond the mean absorbed dose provided by PET and bremsstrahlung SPECT dosimetry, CT-based dosimetry can provide accurate measures of dose-volume metrics, such as D_{70} – the minimum dose absorbed by at least 70% of the target volume. Previous work has shown that the poor spatial resolution of PET and SPECT imaging may provide inaccurate estimates of D_{70} as this metric has been shown to be positively correlated with the voxel size of the imaging modality.[178]

The purpose of this study is to perform precision dosimetry in ^{90}Y TARE through CT imaging of radiopaque microspheres in a rabbit liver model and compare extracted dose metrics to those produced from PET-based dosimetry. This is the first study to provide an *in vivo* comparison of PET and CT-based dosimetry in ^{90}Y TARE.

5.4 Methods and Materials

Numerical values are reported as mean ± standard deviation [minimum, maximum], unless otherwise stated.

5.4.1 Radiopaque Microspheres

Eye90 microspheres (Eye90) are composed of a proprietary, radiopaque glass composition and are similar in density and size to TheraSphere microspheres (20-30 μm diameter, ρ = 3.3 g/cm^3). The ^{90}Y in Eye90 was produced through thermal neutron absorption of ^{89}Y embedded within the microsphere's glass matrix. A nominal bolus of 40 mg (~981,000 microspheres) was measured for administration to each rabbit. The average microsphere specific activity A_{MS} at the time of administration was 156 ± 18 Bq [142, 182].

5.4.2 CT Calibration Phantom

It has been previously demonstrated that a linear relationship, defined by Equation 5.1, exists between HU and radiopaque microsphere concentration MS_{con} over a clinically relevant range of values,

$$HU = m_{cal} \cdot MS_{con} + b_{cal} \quad 5.1$$

where m_{cal} and b_{cal} are the slope and intercept (defined below) of the calibration curve, respectively.[157] Based on this relationship, a calibration phantom was designed to contain cylindrical posts composed of a tissue-equivalent resin (Z_{eff} = 6.45, ρ = 1.03 g/cm^3) and infused with Eye90 in nominal concentrations of 0.5 mg/mL, 5.0 mg/mL, 25.0 mg/mL. There were 9 posts per microsphere concentration with a post length of 40 mm and varying diameters ranging from 2 to 9 mm in 1 mm increments, with an additional post having a diameter of 15 mm. The central axis of all posts was placed equidistant (100 mm) from the central longitudinal axis and were embedded in the resin background material with a radius of 150 mm, as shown in Figure 5.1(a).

This phantom was imaged with a clinical CT (Celesteion™ PET/CT, Canon Medical Systems, Ōtawara, Japan) using a tube potential of 100 kVp and an exposure of 270 mAs. Images were reconstructed with FBP in a 16.2 cm FOV having voxel dimensions of 0.468 mm x 0.468 mm x 2.000 mm reconstructed with a sharp body filter. An axial CT slice of the phantom is shown in Figure 5.1(b) and is displayed with a voxel intensity range of -100 to 200 HU. Within the MIM Software platform v6.9.4 (MIM Software Inc., Cleveland, OH, USA), structures were created for all 27 posts based on the known geometry of the phantom. Segmented post structures were reduced by a 1 mm radial margin and 5 mm longitudinal margin to reduce partial volume effects between the background-post and background-air interfaces, respectively. The 2 mm-diameter post segmentations were not reduced by the 1 mm radial margin as this would eliminate the structures entirely. Instead, they were reduced to a 1 mm-diameter cylinder centred on the post's central longitudinal axis. An additional cylindrical structure with a 30 mm diameter was segmented in the centre of the background region to quantify the intensity of a uniform volume void of microspheres. All segmented structures within the calibration phantom are shown in Figure 5.1(c).

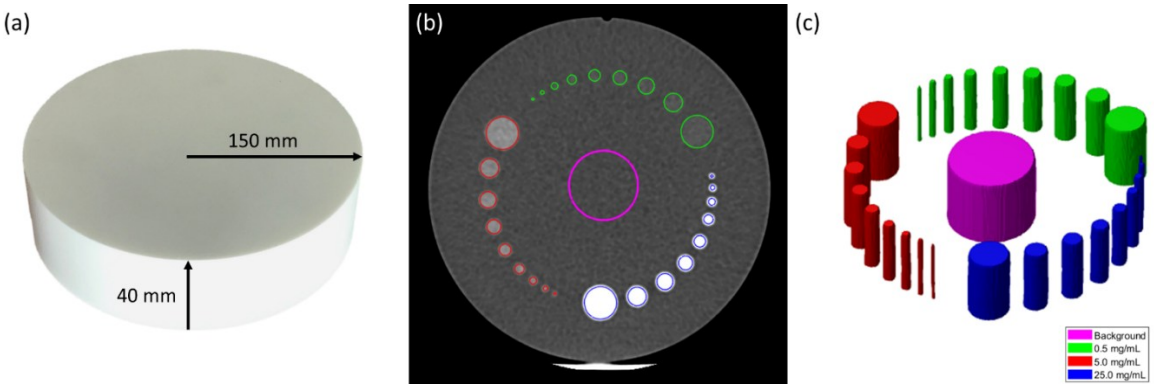

Figure 5.1: (a) Image of the calibration phantom overlaid with physical dimensions. (b) Axial CT slice [HU: -100 to 200] of the calibration phantom with segmented structures for a background region (magenta) and three microsphere concentrations: 0.5 mg/mL (green), 5.0 mg/mL (red), and 25.0 mg/mL (blue). (c) Segmented structures in the calibration phantom.

The mean HU was extracted from each structure and a calibration curve based on Equation 5.1 was determined through a linear least-squares fit of the HU and MS_{con} data. The slope m_{cal} was extracted from the fit while the intercept b_{cal} was calculated independently for each rabbit according to Equation 5.2.

$$b_{cal} = \mu_{bkg} + 1.645\sigma_{bkg} \qquad 5.2$$

Here, μ_{bkg} and σ_{bkg} are the mean and standard deviation, respectively, of voxel values in a non-embolized background region L_{bkg} within each rabbit liver to account for HU variations in the liver parenchyma between rabbits. The factor 1.645 is the Z-score for a one-sided standard normal distribution with a false positive detection rate of $\alpha = 0.05$. As the voxel values within μ_{bkg} were normally distributed, voxels with HU $> b_{cal}$ have a 95% probability of containing Eye90.

To produce a voxelized CT-based ^{90}Y activity distribution A_{CT} with units of Bq, Equation 5.1 was solved for MS_{con} and multiplied by three scalar factors: the number of microspheres per milligram MS_{mg}, the microsphere's specific activity A_{MS} measured at the time of administration, and the CT voxel volume V_{CT}, as shown in Equation 5.3.

$$A_{CT} = MS_{con} \cdot [MS_{mg} \cdot A_{MS} \cdot V_{CT}] \quad 5.3$$

Theoretically, the administered ^{90}Y activity A_0 should be recovered by summing A_{CT} over the segmented rabbit liver volume L. A recovery coefficient RC_{CT} was defined as the ratio of this sum to A_0, expressed as a percentage and shown in Equation 5.4.

$$RC_{CT} = 100 \cdot \left[\frac{\sum_L A_{CT}}{A_0}\right] \quad 5.4$$

For comparison, Equation 5.4 was applied to the PET-derived activity distribution A_{PET} for two structures, L and L_{shell}, where L_{shell} is defined as L plus a 1 cm isotropic margin. The corresponding recovery coefficients are RC_{PET} and RC_{PET}^{shell}, respectively.

5.4.3 Rabbit Liver Model

The University of Missouri Animal Care and Use Committee approved the animal protocol (#9786) whose data were analyzed for this study. Eight White New Zealand rabbits were included in this study (5 males, 3 females) weighing an average of 3.3 ± 0.2 kg [3.0, 3.5]. Rabbits are subsequently referred to as R01 through R08.

Prior to administration, each rabbit was induced with ketamine and dexmedetomidine then maintained on isoflurane and oxygen by mask. Eye90 was administered into either the left or proper hepatic arteries of the liver via a 2.4 Fr Progreat microcatheter. The average whole liver volume was 79 ± 11 mL [65, 97] and the average administered activity was A_0 = 144.2 ± 17.4 MBq [128.1, 171.0] after accounting for residual activity within the administration equipment, where the average residual activity was 8.9 ± 2.0 MBq [6.0, 12.9]. The lung shunt fraction was expected to be negligible based on results from pathologic studies of a rabbit VX2 liver tumour model following the administration of iron oxide microspheres.[179] In this study, both intra-procedural fluoroscopic imaging and post-procedural PET imaging verified microsphere deposition only within L.

5.4.4 Post-Treatment Imaging

Following microsphere administration, each rabbit was imaged with an TOF PET/CT scanner (Celesteion™ PET/CT, Canon Medical Systems, Ōtawara, Japan)

equipped with a lutetium-yttrium oxyorthosilicate (LYSO) scintillator. The radioisotope ^{90}Y was selected for the PET acquisition. Data was acquired using four overlapping bed positions with seven minutes/position. The lower and upper energy level discriminators were set to 435 keV and 650 keV, respectively. Prior to reconstruction, sinograms were corrected for scatter, randoms, and attenuation. Images were reconstructed with the OS-EM algorithm using 3 iterations and 10 subsets in a 128 x 128 x 240 matrix having isotropic voxel sizes of 2.039 mm x 2.039 mm x 2.039 mm. Postfiltering of reconstructed images was performed with a 4 mm FWHM Gaussian filter to reduce image noise.

Following the PET/CT acquisition, an additional four-phase CT was acquired with acquisition parameters set to match the parameters used during CT imaging of the calibration phantom. CT scans included a baseline unenhanced, arterial, portal, and delayed venous phase. Within MIM, the liver volume L was contoured using arterial phase CT to provide maximum contrast between liver parenchyma and surrounding soft tissue. The second structure L_{shell} was generated by isotropically extending L by a 1.0 cm margin. This margin was chosen to account for the reduced PET spatial resolution relative to CT as well as perceived ^{90}Y activity outside of L resulting from respiration, which was shown during intra-procedural angiographic imaging to displace the rabbit livers by a maximum of 1.0 cm in the cranial-caudal direction. A third structure B was generated around the exterior of the rabbit body. In the unenhanced CT, a final structure L_{bkg} was generated in a non-embolized, homogeneous background region of the liver to account for HU variations in the non-embolized liver parenchyma between rabbits. In Figure 5.2, all structures in R03 and R05 are visible in a baseline, unenhanced axial CT slice with a voxel intensity range of -100 to 200 HU.

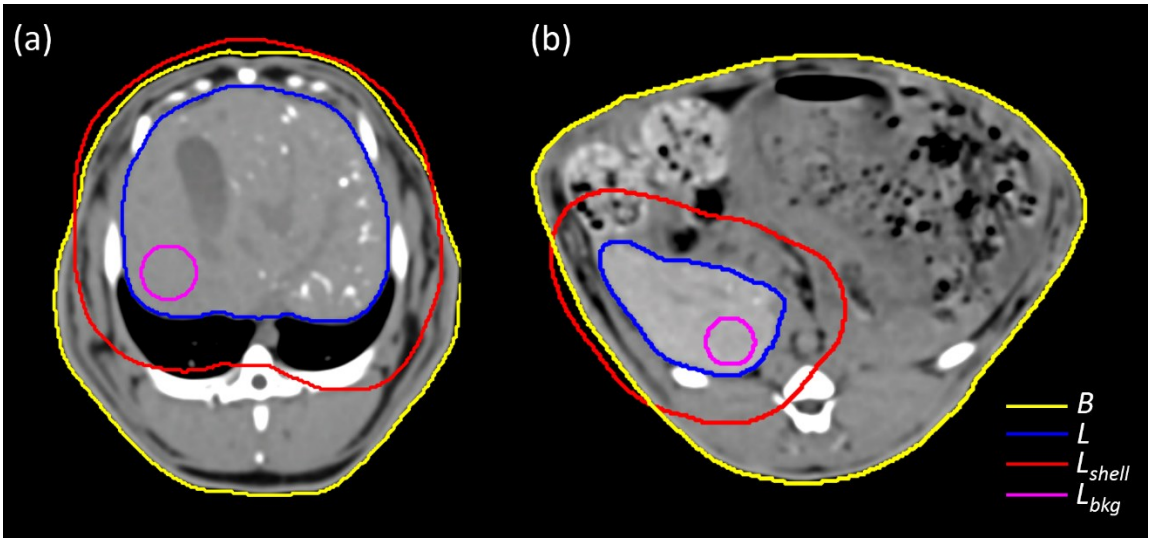

Figure 5.2: Baseline unenhanced axial CT slice [HU: -100 to 200] following the administration of Eye90 showing four structures: the rabbit's body B (yellow), the liver L (blue), the liver extended by an isotropic 1 cm margin L_{shell} (red), and the non-embolized, homogeneous background region L_{bkg} (magenta). (a) R03. (b) R05.

5.4.5 Dosimetry

5.4.5.1 MIRD

Treatment planning for commercially available TheraSphere microspheres is based on a MIRD model that assumes a uniform ^{90}Y activity distribution within a target volume.[52] In this model, the mean dose D_{MIRD} to a target volume is defined in Equation 5.5.

$$D_{MIRD} = \frac{A_0 \cdot 50 \cdot (1 - R)}{M} \qquad 5.5$$

Here, A_0 is the administered ^{90}Y activity in GBq, M is the mass of the target in kg, and R is the fractional residual activity. To serve as a reference for PET- and CT-based dosimetry, D_{MIRD} was calculated for each rabbit liver given R, A_0, the treated liver volume L, and an assumed liver density of 1.03 g/mL.

5.4.5.2 Convolution

Pathohistological studies performed on explanted human livers following ^{90}Y TARE demonstrated a highly heterogeneous *in vivo* microsphere distribution [54,91,180]. Currently, no clinical imaging modality can resolve individual microspheres, so all relevant imaging

methods present a reduced resolution approximation of the true ^{90}Y activity distribution. Within the constraints of this limitation, DVK convolutional dosimetry can be used to calculate the dose distribution based on a heterogeneous ^{90}Y activity distribution. The dose distribution D was determined through the convolution of a cumulated activity distribution $\tilde{A}$ with a spatially invariant DVK, as described in Equation 5.6.

$$D = \tilde{A} \otimes DVK = \sum_{x'} \sum_{y'} \sum_{z'} \tilde{A}(x', y', z') \cdot DVK(x - x', y - y', z - z') \qquad 5.6$$

As microspheres are permanent implants, it was unnecessary to image at multiple time points post-administration to determine the cumulated activity. Instead, $\tilde{A}$ was calculated using Equation 5.7.

$$\tilde{A}(x', y', z') = \int_0^{\infty} A(x', y', z', t)\, e^{-\lambda t}\, dt = \frac{A(x', y', z')}{\lambda} = \tau A\,(x', y', z') \qquad 5.7$$

Here, λ is the decay constant and τ is the mean lifetime of ^{90}Y. The convolution of $\tilde{A}$ and DVK was performed in the frequency domain using the fast Fourier transform. The resulting PET- and CT-based dose distributions are subsequently referred to as DD_{PET} and DD_{CT}, respectively. Dosimetry calculations were performed in MATLAB R2020b (MathWorks Inc., Natick, MA, USA).

5.4.5.3 Dose-Voxel Kernels

The DVKs in this study were calculated through simulations of ^{90}Y radiation transport in a voxelized sphere of water with the GATE v9.0 Monte Carlo toolkit encapsulating Geant4 10.06.p01.[158] Physics processes were enabled according to the standard electromagnetic physics list option 4 and electron transport was performed with an energy cutoff of 1 keV. The DVKs were calculated specific to voxel sizes of A_{CT} and A_{PET}, referred to as DVK_{PET} and DVK_{CT}, respectively. Prior to each simulation, a ^{90}Y source was uniformly distributed within the origin voxel of a spherical water phantom where 40 million histories were set to decay. Voxels whose centre of mass was ≤ 25 mm

from the origin were assigned to water and the remaining voxels were set to air. From the simulation output, the mean absorbed dose per decay was calculated in each voxel. Voxels whose centre of mass was > 25 mm were masked to zero to ensure convolution with spherically symmetric DVKs.

5.4.6 Statistical Analysis

Dosimetric evaluations were carried out through a comparison of standard dose metrics including the median dose D_{med}, maximum dose D_{max}, mean dose D_{μ}, standard deviation σ, and COV defined as σ/D_{μ}. cDVHs were calculated to determine D_{70}. The mean dose D_{μ} across all rabbits was compared between DD_{PET} and DD_{CT} through linear regression, ANOVA, and Bland-Altman analysis. For DD_{CT}, D_{μ} was calculated for the liver volume L. For DD_{PET}, D_{μ} was calculated for the structure L_{shell} to account for reduced spatial resolution and respiratory motion during PET image acquisition.

5.5 Results

5.5.1 CT Calibration Phantom

In Figure 5.3, the mean HU is given as a function of post diameter for all three microsphere concentrations within the phantom. The data show that the mean HU is independent of the post diameter for diameters > 2 mm.

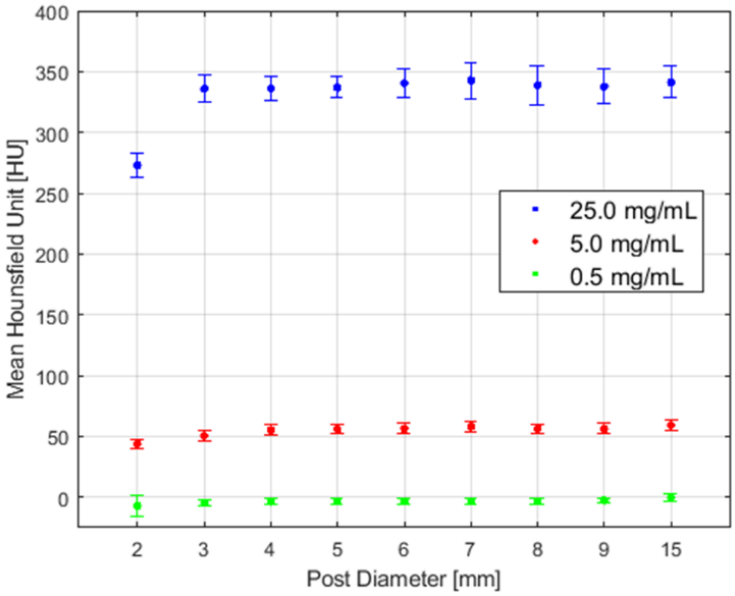

Figure 5.3: The mean HU within post structures as a function of post diameter for the three microsphere concentrations within the CT calibration phantom – 0.5 mg/mL, 5.0 mg/mL, and 25.0 mg/mL. Error bars represent the standard deviation of the voxel values within a post.

The least-squares linear fit presented in Figure 5.4 shows a strong correlation ($r^2 > 0.999$) between HU and MS_{con}. The slope is $m_{cal} = 14.13$ with 95% CI between 13.14 and 15.12. For display purposes, data were offset such that $\mu_{bkg} = 0$.

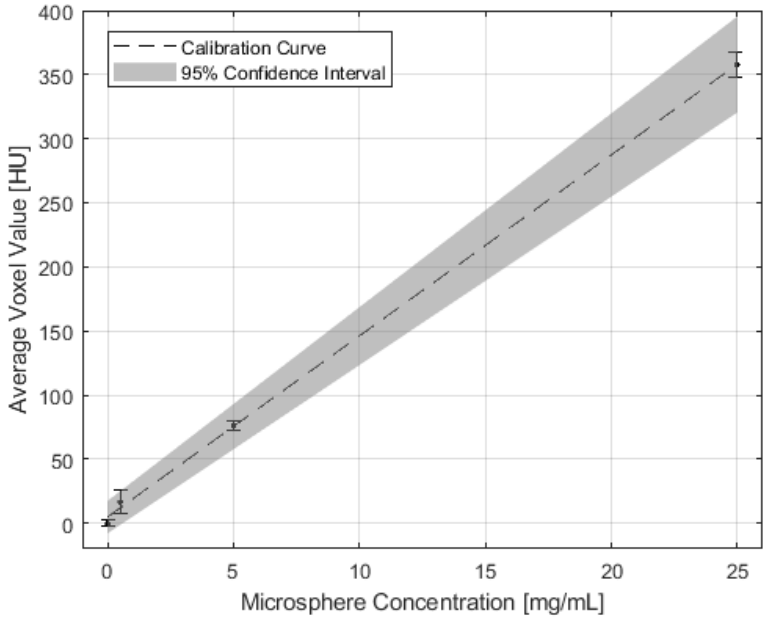

Figure 5.4: Calibration curve derived from the analysis of the calibration phantom ($r^2 > 0.999$). Voxel values were extracted for the 15 mm-diameter posts only.

The microsphere concentration MS_{con} within the liver volume L was determined using Equation 5.1 with $m_{cal} = 14.13$ and b_{cal} specific to each rabbit according to Equation 5.2. Rabbit liver backgrounds μ_{bkg} varied by 40.6 HU with a range of 69.2 to 109.9 HU, while σ_{bkg} was relatively constant across all rabbits**.** Values for μ_{bkg}, σ_{bkg}, and b_{cal} are reported in Table 5.1.

Rabbit Index	$\mu_{bkg} \pm \sigma_{bkg}$ [HU]	b_{cal} [HU]	A_0 [MBq]	A_{CT} (95% CI) [MBq]	A_{PET} [MBq]	A_{PET}^{shell} [MBq]	RC_{CT} [%]	RC_{PET} [%]	RC_{PET}^{shell} [%]
R01	99.1 ± 5.6	110.0	132.4	122.6 (114.6 – 131.9)	93.5	138.4	92.6	70.6	104.6
R02	69.2 ± 3.0	75.1	171.0	119.8 (111.9 – 128.8)	124.3	176.1	70.1	72.7	103.0
R03	84.4 ± 3.7	91.7	155.9	141.9 (132.6 – 152.6)	86.5	143.2	91.1	55.5	91.9
R04	103.8 ± 4.2	112.1	128.1	117.9 (108.7 – 126.8)	51.4	81.9	92.1	40.1	63.9
R05	96.5 ± 3.3	102.9	133.7	132.5 (123.8 – 143.9)	99.9	144.8	99.1	74.7	108.3
R06	109.9 ± 3.8	117.2	171.0	158.2 (147.9 – 171.5)	109.9	164.6	92.6	64.3	96.2
R07	105.4 ± 4.0	113.1	131.6	119.2 (110.4 – 128.2)	103.3	145.0	90.6	78.5	110.2
R08	94.8 ± 4.9	104.3	130.2	100.8 (91.7 – 108.4)	61.5	101.4	77.4	47.2	77.9

Table 5.1: Average HU, calibration curve intercepts, activity parameters, and recovery coefficients for all rabbits.

5.5.2 Activity Distributions

The CT recovery coefficient RC_{CT} was equal to 70.1% in R02 and 77.4% in R08. In the remaining six rabbits, it was found that $RC_{CT} \geq 90.0\%$ while the average RC_{CT} across all eight rabbits was 88.2 ± 8.9% [70.1, 99.1]. There was more variation in RC_{PET} with an average of 62.9 ± 13.0% [40.1, 74.7], although only R02 had A_{PET} within the 95% CI of A_{CT}. Within L_{shell}, the recovery coefficient RC_{PET}^{shell} had an average of 94.5 ± 15.1% [63.9, 110.2] and R03, R06, and R08 had A_{PET}^{shell} within the 95% CI of A_{CT}. Activity parameters (A_0, A_{CT}, A_{PET}, A_{PET}^{shell}) and recovery coefficients (RC_{CT}, RC_{PET}, RC_{PET}^{shell}) are reported in Table 5.1.

5.5.3 Dose-Voxel Kernels

The absorbed dose per decay in the central voxel of DVK_{CT} and DVK_{PET} was 2.21 x 10^{-8} Gy/History and 3.55 x 10^{-9} Gy/History, respectively. Both DVK_{CT} and DVK_{PET} had statistical uncertainties ≤ 0.01% in the central voxel. A 3D surface plot and 2D cross-section through the central voxel are shown for DVK_{CT} in Figure 5.5(a, b). The analogous plots for DVK_{PET} are shown in Figure 5.5(c, d). The vertical axis limits in the surface plots of Figure 5.5(a, c) share the same maximum to emphasize differences in the magnitude of the central voxel as a result of discrete sampling.

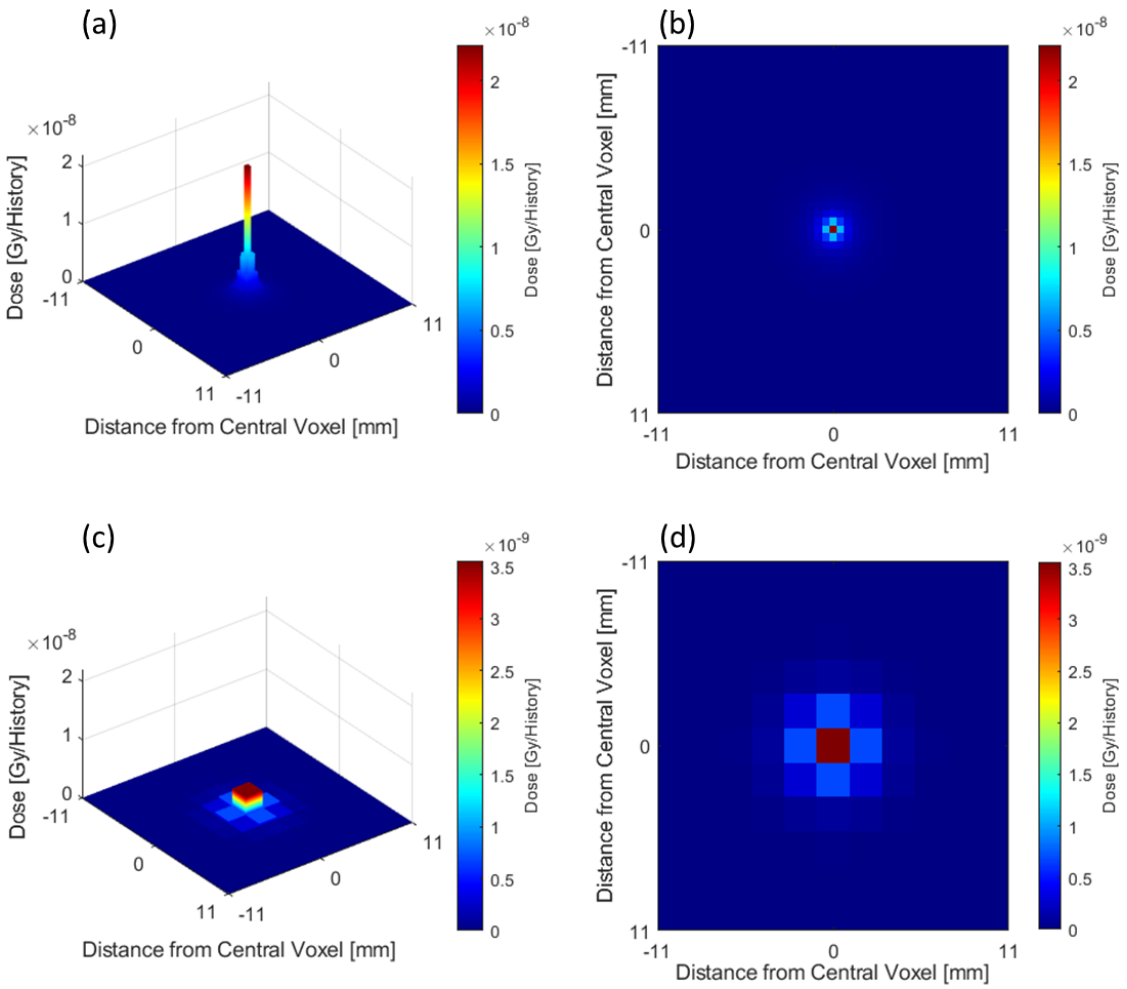

Figure 5.5: (a) 3D surface plot through the central voxel in DVK_{CT}. (b) 2D cross section through the central voxel in DVK_{CT}. (c) 3D surface plot through the central voxel in DVK_{PET}. (d) 2D cross section through the central voxel in DVK_{PET}.

5.5.4 Dose Distributions

For R05, the dose distribution DD_{CT} is shown in Figure 5.6(a-c) and DD_{PET} is shown in Figure 5.6(d-f). For R06, DD_{CT} is shown in Figure 5.7(a-c) while DD_{PET} is shown in Figure 5.7(d-f). Dose distributions are overlaid on an axial CT slice with a voxel intensity range of -100 to 200 HU. Rabbits R05 and R06 are presented as they qualitatively represent the worst and best agreement between DD_{CT} and DD_{PET}. Both dose distributions are displayed with a dose range between 50 and 500 Gy.

In Figure 5.6(a-c), from a qualitative perspective, DD_{CT} appears to contain significant dose gradients and is highly correlated with the embolized vasculature as it was

derived directly from the radiopaque microsphere distribution. In Figure 5.6(d-f), the corresponding PET-based dose distribution DD_{PET} demonstrates a clear discordance with multiple regions containing embolized vasculature. Furthermore, DD_{PET} is more homogeneous with a COV of 0.98 relative to 1.63 in DD_{CT}. At the intersection of the red crosshair in Figure 5.6, there is an absolute dose difference of 134.3 Gy between DD_{PET} and DD_{CT}.

In Figure 5.7(a-f), the dose distributions DD_{PET} and DD_{CT} in R06 share more correspondences than in R05, although DD_{CT} is mostly confined within L while DD_{PET} shows dose spilling beyond L, thereby predicting a low dose to the surrounding soft tissue. This may be attributed to respiratory motion due to the longer scan duration in PET imaging. At the intersection of the red crosshair in Figure 5.7, the absolute dose difference is 1411.2 Gy between DD_{PET} and DD_{CT}. Quantitative dose metrics from all rabbits are reported in Table 5.2.

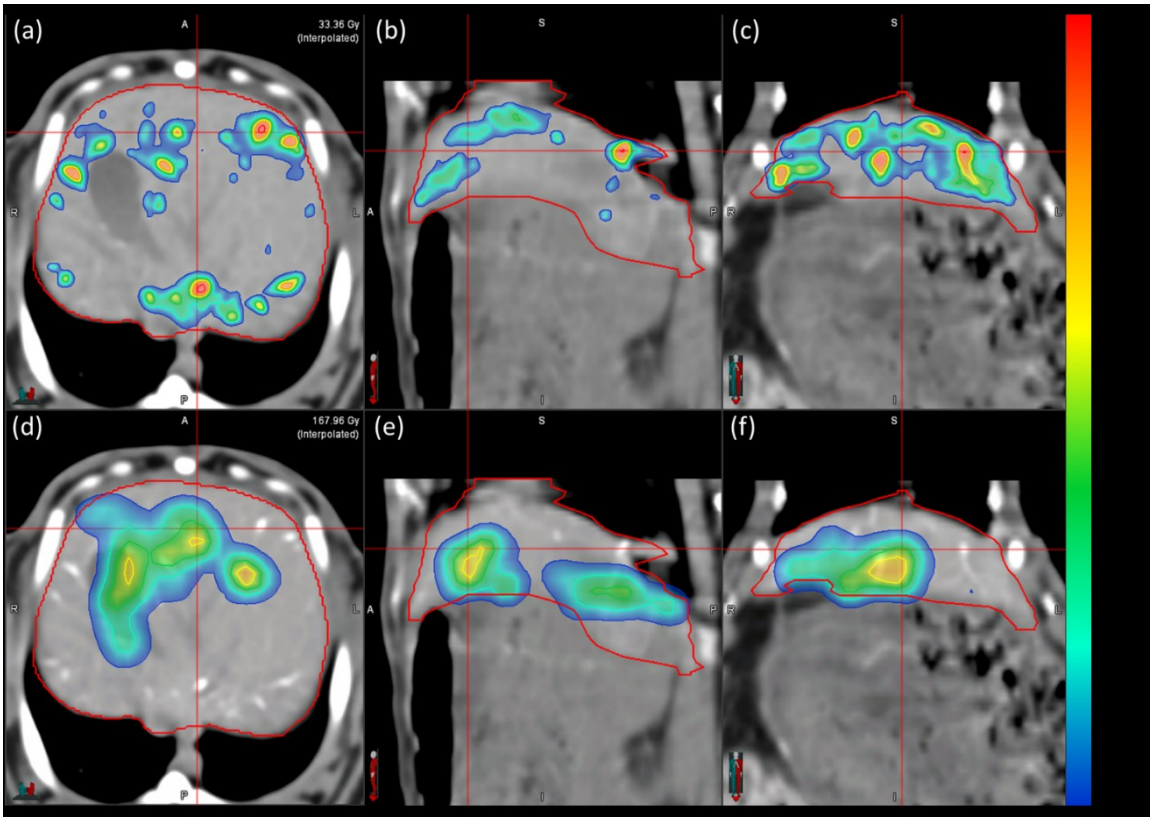

Figure 5.6: (a-c) Axial, sagittal, and coronal views of the CT-based dose distribution DD_{CT} in R05 overlaid on an axial CT [HU: -100 to 200]. (d-f) Axial, sagittal, and coronal views of the PET-based dose distribution DD_{PET} in R05 overlaid on an axial CT [HU: -100 to 200].

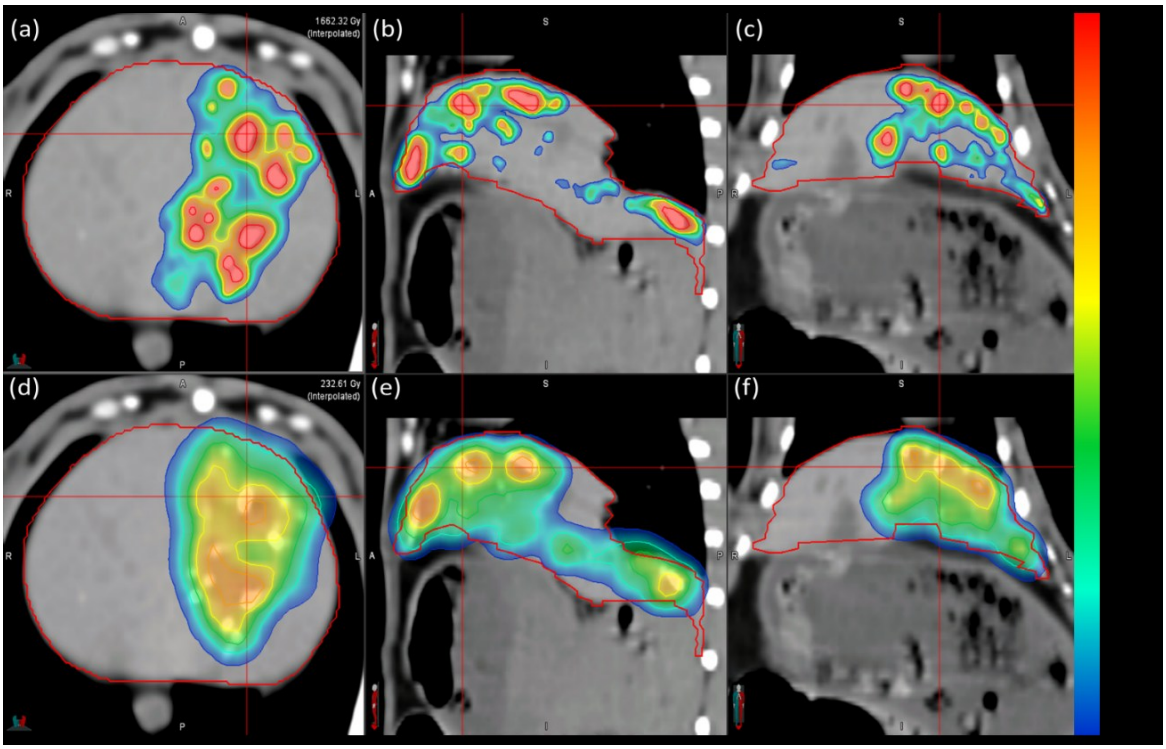

Figure 5.7: (a-c) Axial, sagittal, and coronal views of the CT-based dose distribution DD_{CT} in R06 overlaid on an axial CT [HU: -100 to 200]. (d-f) Axial, sagittal, and coronal views of the PET-based dose distribution DD_{PET} in R06 overlaid on an axial CT [HU: -100 to 200].

Rabbit	Modality	Structure	D_{med}	D_{max}	D_{μ}	σ	COV	D_{70}
R01	CT	L	5.4	1124.3	42.0	78.9	1.9	0.8
		L_{shell}	0.0	1124.3	10.9	42.9	3.9	0.4
		B	0.0	1124.3	3.5	24.9	7.1	0.3
	PET	L	36.7	372.0	65.3	66.0	1.0	11.3
		L_{shell}	6.0	372.0	24.3	44.7	1.8	2.2
		B	1.6	372.0	8.9	27.3	3.1	1.1
R02	CT	L	9.6	1155.8	32.6	57.8	1.8	1.8
		L_{shell}	0.0	1155.8	9.2	33.2	3.6	0.4
		B	0.0	1155.8	3.1	19.6	6.4	0.3
	PET	L	53.3	309.0	68.3	63.0	0.9	16.4
		L_{shell}	9.3	309.1	27.3	44.4	1.6	3.7
		B	1.9	309.0	10.2	27.8	2.7	1.1
R03	CT	L	2.6	1585.5	32.5	84.7	2.6	0.9
		L_{shell}	0.0	1585.5	10.5	48.2	4.6	0.4
		B	0.0	1585.5	4.5	31.8	7.2	0.3

		L	15.9	345.0	42.0	55.0	1.3	10.3
	PET	L_{shell}	8.2	345.0	21.3	37.7	1.8	5.3
		B	3.1	345.0	10.4	25.8	2.5	2.0
R04	CT	L	14.3	754.8	41.9	68.3	1.6	4.3
		L_{shell}	0.0	754.8	11.3	39.0	3.4	0.2
		B	0.0	754.8	3.9	23.5	6.0	0.1
	PET	L	23.4	266.0	36.9	36.3	1.0	15.4
		L_{shell}	8.5	266.0	15.8	23.8	1.5	6.1
		B	3.7	266.0	7.4	15.0	2.0	2.0
R05	CT	L	2.9	1812.3	38.4	96.3	2.5	0.8
		L_{shell}	0.1	1812.3	16.4	64.3	3.9	0.4
		B	0.0	1812.3	3.7	31.0	8.4	0.3
	PET	L	21.7	389.0	58.5	66.0	1.1	9.4
		L_{shell}	6.5	389.3	22.7	43.0	1.9	2.1
		B	1.6	389.0	9.0	27.1	3.0	1.0
R06	CT	L	13.6	1375.6	49.7	91.2	1.8	3.3
		L_{shell}	0.0	1375.6	13.5	50.5	3.7	0.5
		B	0.0	1375.6	4.4	29.7	6.7	0.3
	PET	L	67.5	337.0	72.0	54.2	0.8	39.3
		L_{shell}	9.9	336.8	28.4	41.3	1.5	4.6
		B	1.9	337.0	10.5	26.2	2.5	1.0
R07	CT	L	6.1	1005.1	30.8	63.2	2.0	1.1
		L_{shell}	0.0	1005.1	9.1	36.1	4.0	0.2
		B	0.0	1005.1	3.2	21.9	6.8	0.2
	PET	L	30.6	316.0	54.5	55.0	1.0	12.4
		L_{shell}	6.5	316.4	22.1	38.5	1.7	3.4
		B	1.9	316.0	8.8	24.5	2.8	1.2
R08	CT	L	11.8	966.2	30.2	49.1	1.6	4.0
		L_{shell}	0.1	966.2	8.3	27.7	3.3	0.2
		B	0.0	966.2	3.5	18.5	5.3	0.2
	PET	L	22.5	304.0	39.9	41.2	1.0	11.8
		L_{shell}	7.7	304.4	16.7	27.2	1.6	5.0
		B	3.2	304.0	8.4	18.6	2.2	2.0

Table 5.2: Dose metrics for all structures within the CT-based dose distribution DD_{CT} and the PET-based dose distribution DD_{PET} across all rabbits. All values are in units of Gy except for the unitless COV.

The results from linear regression are shown in Figure 5.8(a) and results from Bland-Altman analysis are shown in Figure 5.8(b). Linear regression revealed a poor correlation between D_μ in DD_{CT} and in DD_{PET} with a coefficient of determination of r^2 = 0.374. The slope of the curve is 0.586 with 95% CI between 0.482 and 0.693. Bland-Altman analysis predicts a mean offset of 15.0 Gy between D_μ in DD_{CT} and in DD_{PET} with 95% CI between 1.8 Gy and 28.2 Gy.

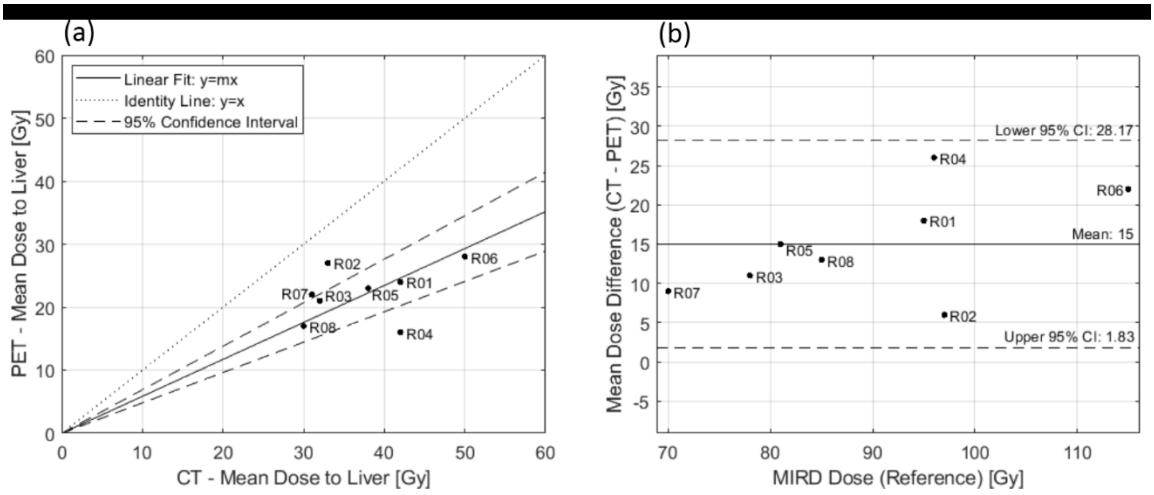

Figure 5.8: (a) Linear regression analysis with 95% CI (dashed) and identity line (dotted) for D_μ in DD_{CT} and DD_{PET}. (b) Bland-Altman analysis with 95% CI (dashed).

Figure 5.9 shows a box-and-whisker plot of D_μ from DD_{CT} and DD_{PET}, as well as the MIRD-derived dose D_{MIRD}. The data indicate a larger dispersion in D_μ for DD_{CT} relative to DD_{PET}. Median values for PET, CT and MIRD are 22.5 Gy, 35.5 Gy, and 90.0 Gy, respectively, with interquartile ranges between 19.0 and 25.5 Gy, 31.5 and 42.0 Gy, and 79.5 and 96.5 Gy, respectively. Results from ANOVA indicate D_{MIRD} and D_μ from DD_{CT} and DD_{PET} are all significantly different with $F(2,21) = 113.2$, $p = 5.65 \times 10^{-12}$. If the absorbed dose is averaged over every constituent voxel of the dose matrices DD_{CT} and DD_{PET}, the discrepancy in D_μ is resolved. In this case, the average difference in D_μ between DD_{CT} and DD_{PET} is only 1.6 ± 0.2 Gy [1.31, 1.95].

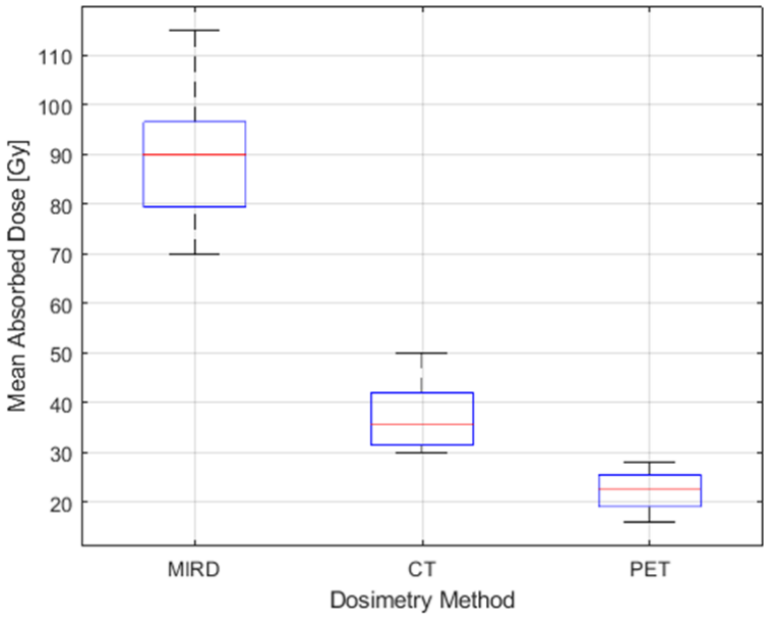

Figure 5.9: Box-and-whisker for D_{μ} across all rabbits extracted from DD_{CT}, DD_{PET}, and D_{MIRD}. The red line represents the median value, the blue box contains data between the 25th and 75th percentiles, and the black whiskers extend to the most extreme data points that are not considered outliers.

5.5.5 Dose-Volume Histograms

Shown in Figure 5.10 are cDVHs in L and L_{shell} for all rabbits. The broader shoulder of the cDVH curves for DD_{PET} indicates a bias toward lower doses relative to DD_{CT}. The long tail of the liver cDVH derived from DD_{CT} implies that a small fraction of volume L received an exceedingly high dose, with the highest dose in R05 greater than 1800 Gy. However, maxima never exceed 389 Gy in DD_{PET}. In most cases, there is better agreement in the cDVH curves of L for DD_{CT} and L_{shell} for DD_{PET}.

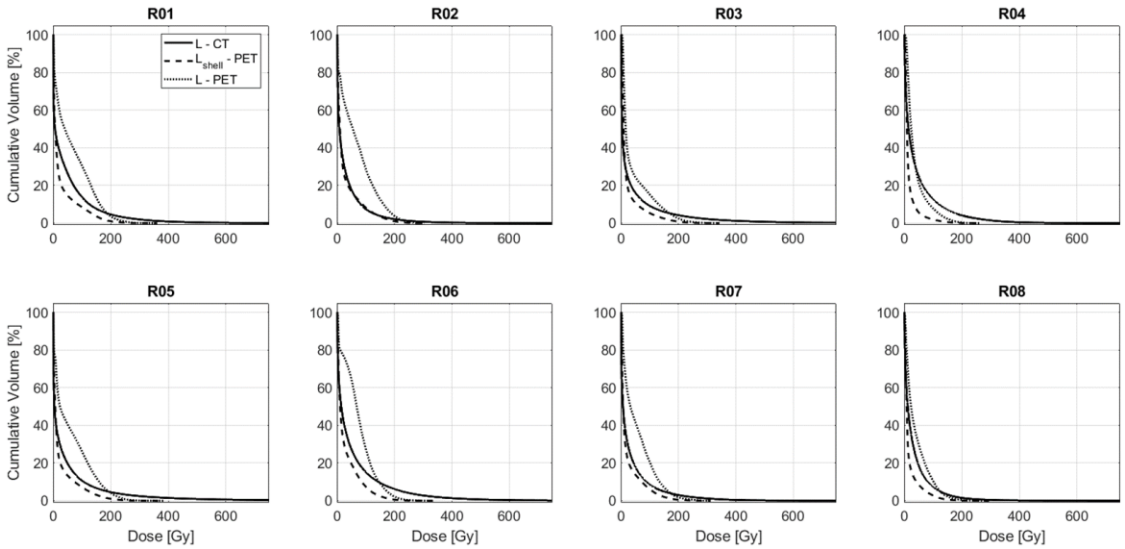

Figure 5.10: Cumulative dose-volume histograms for L and L_{shell} across all eight rabbits.

5.6 Discussion

5.6.1 CT Calibration Phantom

The calibration curve used to determine the microsphere concentration within the rabbits was derived from an analysis of the 15 mm-diameter posts only, despite the presence of embolized vasculature with vessel diameters < 15 mm. An analysis of the 3 to 15 mm-diameter posts in the calibration phantom shows that m_{cal} is independent of the post diameter ($14.01 \leq m_{cal} \leq 14.26$) as demonstrated in Figure 5.11(a). The adjacent scatter plot in Figure 5.11(b) shows that the 2 mm-diameter post ($m_{cal} = 11.63$) has a slope outside the 95% CI of the slopes for the remaining posts, likely due to partial volume effects.

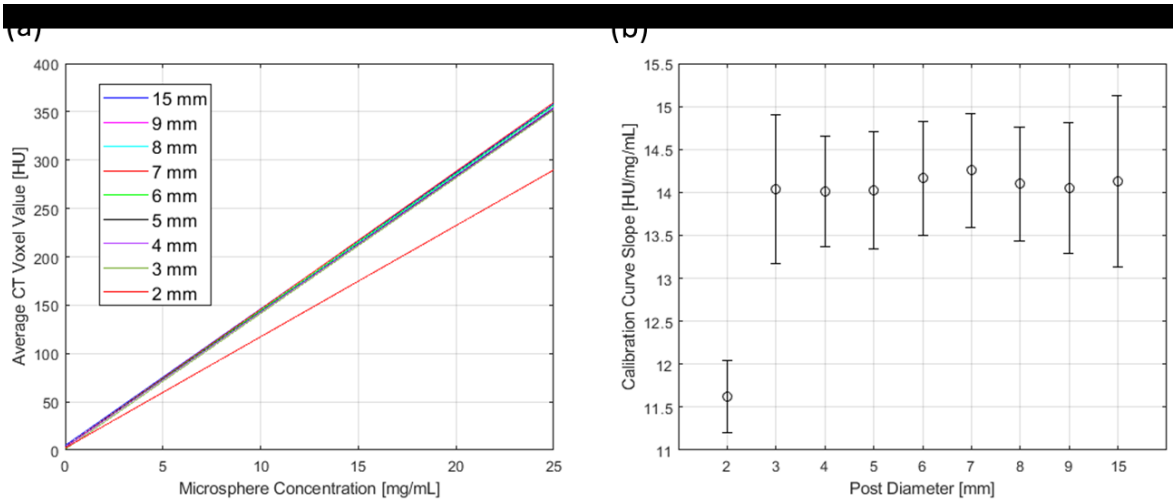

Figure 5.11: (a) Calibration curves derived for all post sizes within the calibration phantom. (b) Calibration curve slope as a function of post diameter with error bars representing 95% CIs.

To justify the use of m_{cal} for vessels with diameters ≤ 2 mm, additional contours were drawn around the 2 mm-diameter post containing 25.0 mg/mL in an attempt to recover the nominal mass of Eye90 within the post. Figure 5.12(a) shows the recovered mass in the post as a function of an expanding radial shell thickness up to ~2 mm and Figure 5.12(b) shows the placement of the shells relative to the true post boundary. The data indicate that, despite the use of m_{cal} derived exclusively from the 15 mm-diameter posts, the nominal mass of Eye90 within the smallest post can still be recovered within 3%. This suggests that diffusion of HU enhancement to surrounding voxels, in part due to CT image acquisition and reconstruction parameters, may introduce additional blurring of the dose over small distance scales (100% of the microsphere mass is recovered within a 0.85 mm-thick shell), but the total microsphere quantification could be highly accurate.

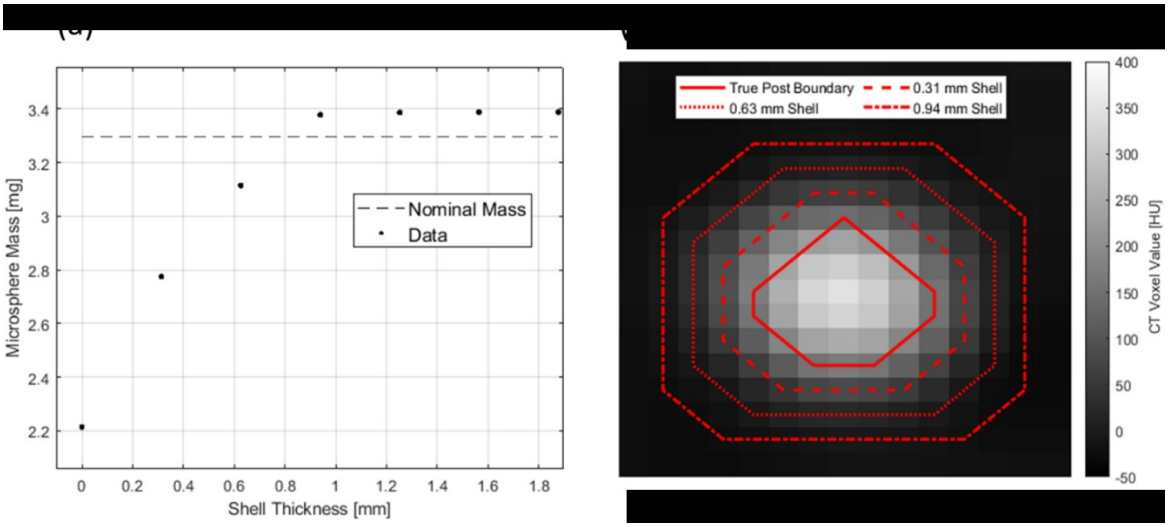

Figure 5.12: (a) The microsphere mass in the 2 mm-diameter post with a microsphere concentration of 25.0 mg/mL as a function of contour shell thickness. The nominal mass of Eye90 within the contour is represented by the dashed horizontal line. (b) Axial CT slice [HU: -50 to 400] of the 2 mm-diameter post with a microsphere concentration of 25.0 mg/mL. The red contours represent extended shell thicknesses.

In Figure 5.6 and Figure 5.7, many high intensity regions are clearly larger in cross sectional area than the equivalent area of the 2 mm-diameter post, further suggesting the impact of these partial volume effects may not be clinically consequential. This can be verified by the similar values for RC_{CT} and RC_{PET}^{shell} reported in Table 5.1. An experimental calibration phantom featuring conical inserts that taper to a point is under development to further explore the dependence of the calibration curve slope on diameters ≤ 2 mm.

5.6.2 Minimum Detectable Activity

An alternative approach in the development of CT calibration curves would require pre- and post-CT imaging of a liver tumour before and after microsphere administration to determine a relative HU enhancement, ΔHU. This approach was not taken in this work as respiratory motion artefacts produced undesirable results following image co-registration with the post-treatment CT. Human patients can perform breath holds during their pre- and post-treatment CT to reduce these image discrepancies. However, we can still apply the ΔHU calibration approach to the calibration phantom in an effort to determine a theoretical limit of detection (LOD_{HU}), as described by the Clinical and Laboratory Standards Institute [181] and previously implemented in determining the detectable iodine concentrations within anthropomorphic phantoms.[162]

If the population of voxels within the background is normally distributed with a mean voxel value $\mu_{bkg\_phant} = 0$ (following the ΔHU calibration approach) and a standard deviation σ_{bkg_phant}, the limit of blank (LOB_{HU}) is the voxel value found when replicates of μ_{bkg_phant} are repeatedly measured, and is defined in Equation 5.8.

$$LOB_{HU} = \mu_{bkg\_phant} + 1.645\sigma_{bkg\_phant} \quad 5.8$$

The LOD_{HU} is the lowest microsphere concentration to be reliably distinguished from the LOB_{HU}, and is determined measuring replicates of a sample known to contain a low microsphere concentration (0.5 mg/mL), as defined in Equation 5.9.

$$LOD_{HU} = LOB_{HU} + 1.645\sigma_{0.5} \quad 5.9$$

We apply the calibration curve parameters to find LOD_{HU} in terms of microsphere concentration, $LOD_{mg/mL}$ using Equation 5.10.

$$LOD_{mg/mL} = \frac{LOD_{HU} - b_{cal}}{m_{cal}} \quad 5.10$$

The minimum detectable ^{90}Y activity concentration from CT imaging MDA_{CT} can be determined from MS_{mg}, A_{MS}, and $LOD_{mg/mL}$, as shown in Equation 5.11.

$$MDA_{CT} = LOD_{mg/mL} \cdot MS_{mg} \cdot A_{MS} \quad 5.11$$

Given MS_{mg} = 24,526 MS/mg, the average specific activity of A_{MS} = 156 Bq, and $LOD_{mg/mL}$ = 0.22 mg/mL, Equation 5.11 yields $MDA_{CT} \approx$ 0.84 MBq/mL. The corresponding value in TOF ^{90}Y PET imaging has previously been estimated as MDA_{PET} = 1.0 MBq/mL for small lesions.[182] We can apply Equation 5.5 to determine the corresponding dose in a voxel volume given $A_0 = MDA_{CT} \cdot V_{CT}$, M = 1.03 g/mL$\cdot V_{CT}$, and R = 0. For a single PET voxel, the MIRD dose corresponding to MDA_{PET} is 49 Gy, while

the MIRD dose for a single CT voxel is 40 Gy. These threshold dose values justify the lower limit of the dose distribution color bar in Figure 5.6 and Figure 5.7 and are also well below the estimated dose threshold required to produce a therapeutic response. This implies that CT is not inferior to PET in terms of detectable activity and dose levels while still being capable of producing more realistic heterogeneous dose distributions. The value of MDA_{CT} also suggests that CT-based dosimetry will be sensitive enough to characterize regions of the target volume that may be at risk for disease progression. Accurately assessing the tumour coverage is essential as low dose regions correlate with reduced local control and an increased probability of local recurrence.[151]

5.6.3 Dose Discrepancies

As demonstrated in Figure 5.9, the median dose from D_{MIRD} is greater than D_{μ} extracted from DD_{CT} and DD_{PET}. This difference may be attributed to the inherent assumption in Equation 5.5, namely the uniform distribution of ^{90}Y activity within the liver. This assumption prevents dose from spilling out of the liver contour into adjacent structures. This is in direct contrast with convolutional dosimetry, where significant microsphere uptake in the liver periphery resulted in dose being deposited outside of the liver contour.

It has previously been shown that, following the administration of radiopaque microspheres into a porcine renal model, the mean dose within a VOI was to be within 5% of a ground truth mean dose as the voxel size increased from an isotropic 0.18 mm to 15 mm.[178] However, in this work, D_{μ} in DD_{CT} was greater by an average of 39.2 ± 17.0% [12.6, 70.8] relative to D_{μ} in DD_{PET}. This suggests the differences in D_{μ} are not entirely due to difference in spatial resolution. Furthermore, since CT and PET imaging were performed 30 minutes apart in this study, differences between DD_{CT} and DD_{PET} cannot be attributed to changes in hepatic vascularization, catheter positioning, or flow characteristics between macroaggregates and microspheres, as is the case when comparing dose distributions derived from ^{90}Y PET imaging and ^{99m}Tc-MAA SPECT imaging.[62,183] Instead, dose discrepancies can be attributed to imaging modality-specific characteristics.

5.6.3.1 PET

The chief limitations in ^{90}Y PET imaging result from the low positron fraction (~32 ppm). At very low counts, PET images are noisy, and the resulting scatter correction might lead to significant under or overestimation of the scatter contribution.[88] Moreover, bremsstrahlung photons and prompt gammas can result in a very high fraction of random coincidences when imaging ^{90}Y. Corrections for scatter and randoms generate noise in the true coincidence sinogram of count-deprived images, with the potential for a large fraction of negative counts. Reconstruction algorithm positivity constraints truncate negative values which can cause an overestimation of ^{90}Y activity due to a positive bias in low or zero activity regions in the reconstructed image.[88]

An additional limitation lies in the choice of scintillator material. Most modern TOF PET scanners utilize lutetium-based scintillators, such as cerium-doped lutetium oxyorthosilicate (LSO[Ce]) or cerium-doped lutetium-yttrium oxyorthosilicate (LYSO[Ce]). Although these have desirable characteristics in terms of temporal resolution, light output, and detection efficiency, the presence of naturally occurring radioisotope ^{176}Lu produces undesirable intrinsic background counts within the scintillator that can reduce quantitative accuracy in the case of low counts and a high randoms fraction.[184]

Furthermore, due to the low positron fraction in ^{90}Y PET imaging, scan times typically require between 15 and 30 minutes over which many respiratory cycles occur.[86] This effectively smears the measured ^{90}Y activity distribution over a larger volume, reducing the total activity within the CT-derived liver contour. To quantify the "loss" of activity in A_{PET}, the ratio of ^{90}Y activity outside of L_{shell} to the activity within B was calculated and is reported in Table 5.3. On average, 14% of administered ^{90}Y activity in A_{PET} lies outside L_{shell}. A rationale for the extreme activity loss in R04 (RC_{PET} = 40.1%) is the relatively high ratio (27%) of ^{90}Y activity beyond L_{shell}. The reduced spatial resolution of PET imaging relative to CT imaging may also contribute to this effect.

Rabbit Index	PET Activity Ratio [%]
R01	11
R02	12
R03	14
R04	27
R05	10
R06	12
R07	12
R08	16

Table 5.3: Ratio of ^{90}Y activity outside of L_{shell} to the activity within B to quantify extrahepatic ^{90}Y activity in A_{PET}.

In this study, given the range of liver motion observed during intra-procedural angiographic imaging (1.0 cm), there may be a degree of dosimetric uncertainty as a result of PET/CT co-registration. A study by Vogel *et al*. reported 40% of patients encounter an absolute PET/CT co-registration error exceeding 1 cm in the cranial-caudal dimension when employing an expiration breath hold technique during CT imaging.[185] Based on these results, deviations in D_{μ} can be expected between DD_{PET} and DD_{CT}, particularly for tumours proximal to the liver dome.

5.6.3.2 CT

An issue specific to post-treatment CT imaging in ^{90}Y TARE is the use of vascular contrast agents when guiding the catheter through the hepatic arterial vasculature. Although a rabbit-specific b_{cal} accounts for varying μ_{bkg}, contrast agent uptake within L was still observed. For example, the healthy liver background intensity appears larger in R05 compared to R03, as demonstrated in Figure 5.2. This artificial increase is attributed to contrast uptake in the healthy liver tissue and highlights the need for a rabbit-specific b_{cal}. It is unlikely that contrast uptake would be mistaken for radiopaque microsphere distributions as the contrast was uniformly distributed throughout the entire liver volume. The placement of L_{bkg} must therefore be chosen in a homogeneous region void of radiopaque microsphere uptake to accurately reflect the baseline HU value of the healthy liver tissue.

An additional drawback in implementing a CT-based approach to dosimetry in ^{90}Y TARE is that it requires an indirect method of ^{90}Y activity quantification that requires the intermediate step of imaging and analyzing a calibration phantom. This may introduce additional uncertainty in DD_{CT}. For example, the calibration curve slope m_{cal} was calculated with 95% CI. In R05, when using the upper 95% CI in m_{cal} to determine DD_{CT}, D_{μ} decreased by 2.5 Gy, from 38.6 Gy to 35.9 Gy. When using the lower 95% CI in m_{cal}, D_{μ} increased by 3.3 Gy, from 38.6 Gy to 41.7 Gy. The corresponding A_{CT} values for the upper and lower 95% CI are 123.8 MBq and 143.9 MBq, respectively, while A_0 was 133.7 MBq.

CT image artifacts may present additional complications. High-Z objects proximal to the intended treatment target, such as clips, coils, or calcifications, could produce image artifacts that may be mistaken for radiopaque microsphere uptake. In these cases, image artifacts could be mitigated by implementing the ΔHU calibration approach discussed previously. A qualitative review of the CT images in this study failed to identify significant artifacts (resulting from microspheres) similar to those that can be seen in CT images in the presence of high-Z objects.

5.6.4 Dose Heterogeneity

This study has demonstrated that a significant benefit of CT-based dosimetry is its ability to reveal the high dose heterogeneity known to exist from pathohistological studies on explanted livers following ^{90}Y TARE.[54,91] The COV values in Table 5.2 verify this heterogeneity as the COV within L in DD_{CT} is consistently greater than the corresponding values in DD_{PET} with an average of 1.99 ± 0.35 [1.63, 2.61] in DD_{CT} and 1.02 ± 0.15 [0.75, 1.31] in DD_{PET}. The high spatial resolution of CT also provides an opportunity to further investigate dose-volume metrics for predicting response in ^{90}Y TARE. One of the earliest studies reporting dose-volume metrics in ^{90}Y TARE was performed by a Kao *et al*. where D_{70} > 100 Gy was suggested as a threshold to predict treatment response in HCC.[105] A subsequent study by Fowler *et al*. indicated dose-volume metrics predict response better in hypovascular lesions than in hypervascular ones, and suggested one incorporate a measure of tumor dose heterogeneity, such as the COV, into the dose-response analysis to improve the positive predictive value.[173] Willowson *et al*. later found D_{70} resulted in a stronger

correlation with outcome than D_μ in metastatic colorectal cancer patients.[106] More recently, a study performed by Kappadath *et al*. found D_μ and D_{20} to D_{80}were correlated with mRECIST response criteria.[103] We have previously shown that D_{70} is dependent on the spatial resolution of the imaging modality[178], and in this study, the data show D_{70} in the liver volume L (and in L_{shell}) are consistently overestimated in DD_{PET} relative to their corresponding values in DD_{CT}. Although these results are not derived from a hypervascular tumour model, they suggest that existing dose-response data based on dose-volume metrics derived from PET and bremsstrahlung SPECT may be improved with CT-based dosimetry in ^{90}Y TARE.

5.7 Conclusion

The recovery of the radiopaque microsphere mass within the rabbits validates CT-based dosimetry in ^{90}Y TARE. Due to the high-resolution of CT imaging, the benefits of this novel approach include improved visualization of the dose distribution, reduced partial volume effects in dose reporting, and a better representation of dose heterogeneity allowing for the extraction of more accurate dose-volume metrics. Effects of respiratory motion are also mitigated when compared to post-treatment PET or bremsstrahlung SPECT imaging. Future work aims to validate these benefits in a hypervascular tumour model.

Ultimately, post-treatment CT imaging of radiopaque microspheres provides the means to perform precision dosimetry in ^{90}Y TARE and extract accurate dose metrics used to refine the understanding of the dose-response relationship in ^{90}Y TARE. Understanding the dose-response relationship could translate into improved patient outcomes.

Chapter 6 Clinical Calibration Phantom Analysis

6.1 Introduction

Based on the strong linearity of the calibration curves derived from the analysis of the agarose phantom CT image data described in Chapter 3, multiple iterations of a resin-based calibration phantom were designed. The purpose of this design was to allow for a single, transportable calibration phantom that could calibrate CT scanners from a range of manufacturers across multiple institutions, and to avoid the primary constraint of the agarose calibration phantoms – rapid dehydration which prevented long term usage. The resin-based phantom was first described in Section 4.6.1 with additional analysis provided in Chapter 5. Still, a more in-depth analysis of the calibration phantom image data is required to fully quantify the relationship between HU and radiopaque microsphere concentration over a range of clinical CT acquisition parameters. The CT-based dosimetry framework depends entirely on an accurate application CT calibration curve. To this end, a clinical calibration phantom was imaged across multiple CT platforms providing a wealth of CT image data. This work aims to study the impact of CT model, acquisition parameters, and phantom size on the magnitude of the calibration curve slope m_{cal}, and to compare the limit of microsphere concentration detectability $LOD_{mg/mL}$ across multiple CT models.

6.2 Methods and Materials

The CT calibration phantom geometry, structure segmentation, and mean HU extraction were previously described in Section 5.4.2.

6.2.1 CT Image Protocol

The three CT scanners in this study include a GE Optima CT580 (Optima CT580 RT, GE Healthcare, Chicago, IL, USA), a Siemens SOMATOM AS+ (SOMATOM Definition AS+, Siemens Healthcare Ltd, Erlangen, Germany), and a Canon Celesteion PET/CT (Celesteion PET/CT, Canon Medical Systems, Ōtawara, Japan). CT image data of the calibration phantom was collected over a range of X-ray tube potentials, tube currents, CT slice thicknesses, and reconstructed FOVs. Image data was also collected and with and without an external scattering module to simulate variations in patient size. CT image acquisition parameters for all 12 scans in this study are provided in Table 6.1.

CT Scan Index	Imaging Date	CT Scanner	Scattering Module	Tube Potential [kVp]	Tube Current [mA]	Slice Thickness [mm]	FOV [cm]
1	09/16/2020	Siemens/SOMATOM	Y	120	300	5.00	50
2	09/16/2020	Siemens/SOMATOM	Y	120	300	5.00	25
3	09/16/2020	Siemens/SOMATOM	Y	140	300	2.00	50
4	01/12/2021	Toshiba/Celesteion	N	100	400	0.50	16
5	01/12/2021	Toshiba/Celesteion	N	100	400	2.00	16
6	12/21/2020	Toshiba/Celesteion	N	100	270	2.00	16
7	01/21/2020	GE/Optima CT580	Y	80	600	1.25	39
8	05/11/2021	GE/Optima CT580	N	100	300	1.25	20
9	01/21/2020	GE/Optima CT580	Y	120	600	1.25	39
10	05/11/2021	GE/Optima CT580	N	120	600	1.25	39
11	05/11/2021	GE/Optima CT580	Y	120	600	1.25	39
12	01/21/2020	GE/Optima CT580	Y	140	600	1.25	39

Table 6.1: Calibration phantom CT scan acquisition parameters.

6.2.2 Image Co-Registration

Calibration curves were calculated based on the mean HU from the 15 mm-diameter posts only. To transfer the calibration phantom post structures (originally segmented in CT scan index 6) to other CT volumes, a rigid co-registration was performed using a three-point match. The calibration phantom was designed with a hemispherical notch on its circular periphery, as shown in Figure 5.1(b). Two match points were placed on the left and right corners of the hemisphere and the third was placed at the notch's deepest, most inferior point. These notch positions were ideal for a point-match as they were easily identifiable and structurally rigid. The target registration error TRE was calculated using Equation 6.1.

$$TRE = \sqrt{\frac{1}{3}\sum_{i=1}^{3}(d_{P,i} - d_{S,i})^2} \qquad 6.1$$

Here, $d_{P,i}$ and $d_{S,i}$ are matching points in the primary and secondary CT image volumes, respectively. The average and maximum TRE across the three points were tabulated for each rigid co-registration.

6.2.3 Image Analysis

The magnitude of the slope of the calibration curves m_{cal} was compared through a Student's t-test, except in the comparison of X-ray tube potentials where ANCOVA and a post-hoc Tukey's test were required due to the increased number of comparisons.[146] The results of statistical tests were considered significant when their p-values were less than 0.05. Calibration curve intercepts b_{cal} were not included in the analysis as they are calculated based on a patient-specific HU background value, as described by Equation 5.2.

The effects of altering the reconstructed FOV, slice thickness, and tube current on the magnitude of m_{cal} were determined through the analysis of CT indices 1 and 2, 4 and 5, and 5 and 6, respectively. Similarly, the effect of imaging with the scattering module was determined through the comparison of calibration curves derived from CT indices 10 and 11. X-ray tube potential comparisons were determined through the analysis of CT indices 7, 9, and 12. CT scanner manufacturer was compared through the analysis of CT indices 6 and 8, and 3 and 12. Temporal stability was determined through the analysis of CT indices 9 and 11. Radial and longitudinal line profiles were measured within the calibration post structures to investigate the uniformity of the microsphere concentration.

The LOD concept was first introduced in Section 3.4.5 and was applied in Section 5.6.2 to determine the minimum detectable ^{90}Y activity through CT imaging of a rabbit liver model. Here, the LOD concept was applied to extract the detect the minimum detectable microsphere concentration $LOD_{mg/mL}$ from the analysis of CT image data of the calibration phantom acquired from different CT scanners.

6.3 Results

6.3.1 Image Co-Registration

Average (across the three match points) and maxima TRE for all co-registrations are given in Table 6.2. Across all co-registrations, the average ± standard deviation of the TRE is 0.19 ± 0.09 mm. The corresponding values for the maximum TRE are 0.25 ± 0.11 mm. The average TRE is less than the axial CT pixel dimension, suggesting contour manipulation was unnecessary following image co-registration. A visual inspection verified the image co-registration did not result in the incorrect placement of post contours.

CT Scan Indices	Target Registration Errors [mm]	
	Average	Maximum
6 – 1,2,3	0.31	0.39
6 – 4,5	0.26	0.33
6 – 8	0.21	0.26
6 – 9,12	0.15	0.21
6 – 10	0.05	0.07
6 – 11	0.17	0.26
Average ± Standard Deviation	0.19 ± 0.09	0.25 ± 0.11

Table 6.2: CT volume target registration errors.

6.3.2 Calibration Curves

The magnitude of m_{cal} and its associated CI, derived from a linear least-squares fit of the calibration phantom CT image data, are reported in Table 6.3. The value of m_{cal} varies by 5.05 HU/mg/mL (9.08 to 14.13) across the CT scans reported in Table 6.1.

CT Scan Index	m_{cal} [HU/mg/mL]	m_{cal} (95% CI) [HU/mg/mL]
1	10.64	9.79, 11.48
2	10.70	9.85, 11.55
3	9.18	8.41, 9.94
4	14.11	13.13, 15.10
5	14.11	13.13, 15.08
6	14.13	13.14, 15.12
7	11.81	10.57, 13.04
8	13.25	12.50, 14.01
9	10.65	9.57, 11.74
10	12.25	11.50, 12.99
11	10.71	9.71, 11.70
12	9.08	8.07, 10.10

Table 6.3: Calibration curve slopes and associated CIs.

Calibration curves calculated from CT acquisitions with varying tube current, slice thickness and FOV are displayed in Figure 6.1(a-c). Results from the Student's t-test illustrate that a change in these acquisition parameters (within the given range) has no

significant effect on the value of the slope, where $p = 0.949$ for the tube current comparison, $p = 0.981$ for the slice thickness comparison, and $p = 0.825$ for the FOV comparison. Figure 6.1(d) shows calibration curves calculated with identical CT acquisition parameters where the imaging was performed 479 days apart. The values of m_{cal} were not statistically different ($p = 0.644$), indicating this phantom has temporal stability over the time scale in question.

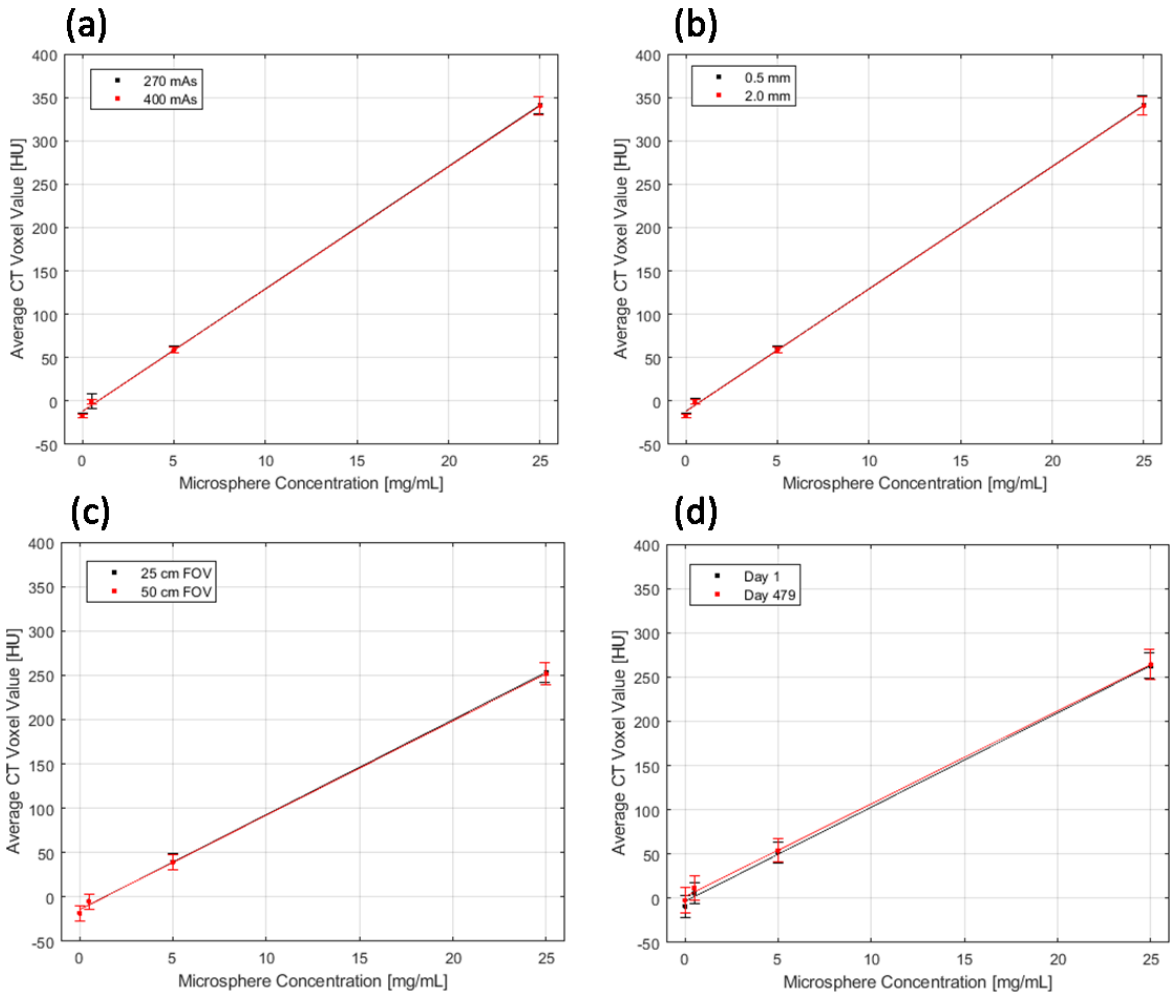

Figure 6.1: (a) Calibration curves derived from CT indices 5 and 6 comparing the slope magnitude due to changes in tube current. (b) Calibration curves derived from CT indices 4 and 5 comparing the slope magnitude due to changes in slice thickness. (c) Calibration curves derived from CT indices 9 and 11 comparing the slope magnitude due to changes in the time of imaging.

The calibration curves derived from imaging with and without the scatter module are shown in Figure 6.2(a) while curves derived over multiple X-ray tube potentials (80,

120, 140 kVp) are shown in Figure 6.2(b). The data indicate the presence of the scatter module significantly reduces m_{cal} (p = 0.006) from 12.25 HU/mg/mL to 10.71 HU/mg/mL. Similarly, the magnitude of m_{cal} decreases as tube potential is increased ($F(2,6) = 27.75$, $p = 0.009$). The post hoc Tukey test reveals a p-value of 0.012 for the 80-120 kVp comparison, $p = 7.52 \times 10^{-4}$ for 80-140 kVp comparison, and $p = 0.045$ for the 120-140 kVp comparison.

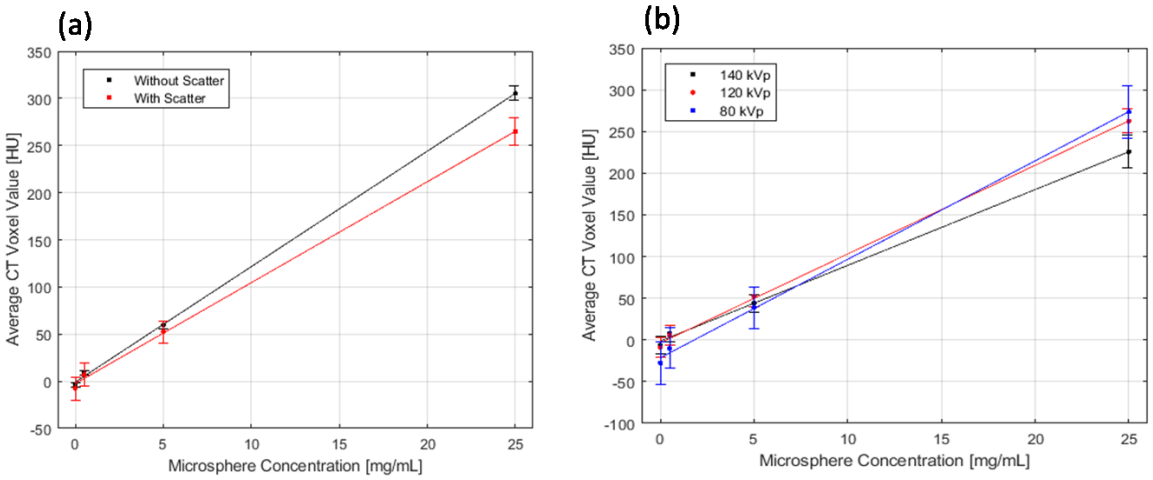

Figure 6.2: (a) Calibration curves derived from CT indices 10 and 11 comparing the slope magnitude due to the presence of the calibration phantom scatter module. (b) Calibration curves derived from CT indices 7, 9, and 12 comparing the slope magnitude due to changes in tube potential.

In Figure 6.3(a), calibration curves from a Toshiba Celesteion and a GE Optima CT580 are shown. The calibration curve slopes were found to be significantly different (p = 0.039), while in Figure 6.3(b), calibration curves derived from a Siemens SIOMATOM AS+ and a GE Optima CT580 show there is no significant difference in m_{cal} (p = 0.770).

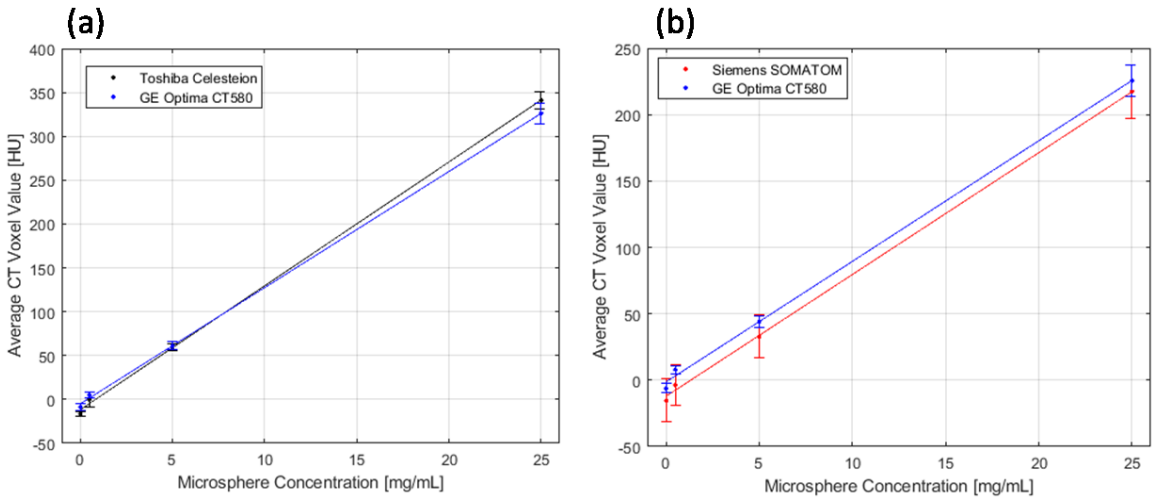

Figure 6.3: (a) Calibration curves derived from CT indices 6 and 8 comparing the slope magnitude due a change in CT scanner. (b) Calibration curves derived from CT indices 3 and 12 comparing the slope magnitude due a change in CT scanner.

6.3.3 Limit of Detection

The LOD in terms of microsphere concentration was previously reported to be $LOD_{mg/mL}$ = 0.22 mg/mL for the Toshiba Celesteion PET/CT following repeat scans of the calibration phantom with the acquisition parameters for CT scan index 6, as reported in Table 6.1. The calibration curve for this scan is displayed in Figure 6.4(a), in addition to the values $LOD_{mg/mL}$ = 0.22 mg/mL and corresponding LOD_{HU} = 3.1 HU values related by Equation 5.10. This calculation was also performed from repeated calibration phantom imaging using the GE Optima CT580 with acquisition parameters from CT scan index 8, resulting in a LOD_{HU} = 2.4 HU and $LOD_{mg/mL}$ = 0.18 mg/mL, as shown in Figure 6.4(b).

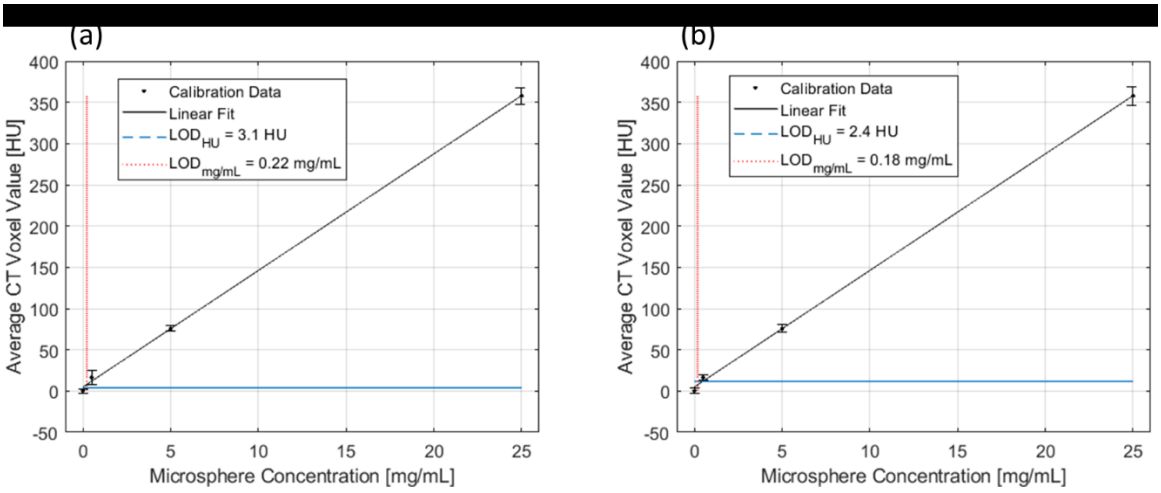

Figure 6.4: Calibration curves overlaid with horizontal (dashed) and vertical (dotted) lines indicating the microsphere detectability values in terms of voxel intensity [HU] and microsphere concentration [mg/mL]. (a) Calibration curve derived from CT scan index 6. (b) Calibration curve derived from CT scan index 8.

6.3.4 Uniformity

Figure 6.5(a,b) show an average HU and standard deviation measured from each slice containing the structure of the 15 mm-diameter post for CT scan index 6, across all three microsphere concentrations. The data show that the HU values are stable along the length of the post structure indicating strong uniformity of the microsphere concentration. The standard deviations of the HU values along the posts are also relatively constant with variations on the order of 2 HU. The average COV values across the profiles are -4.10, 0.13, and 0.05 for the posts having microsphere concentrations of 0.5 mg/mL, 5.0 mg/mL, and 25.0 mg/mL, respectively. The negative COV value for the post with a microsphere concentration of 0.5 mg/mL simply results from the negative mean intensity value (-0.28 HU). Similar longitudinal uniformity was observed in the remaining posts with diameters less than 15 mm.

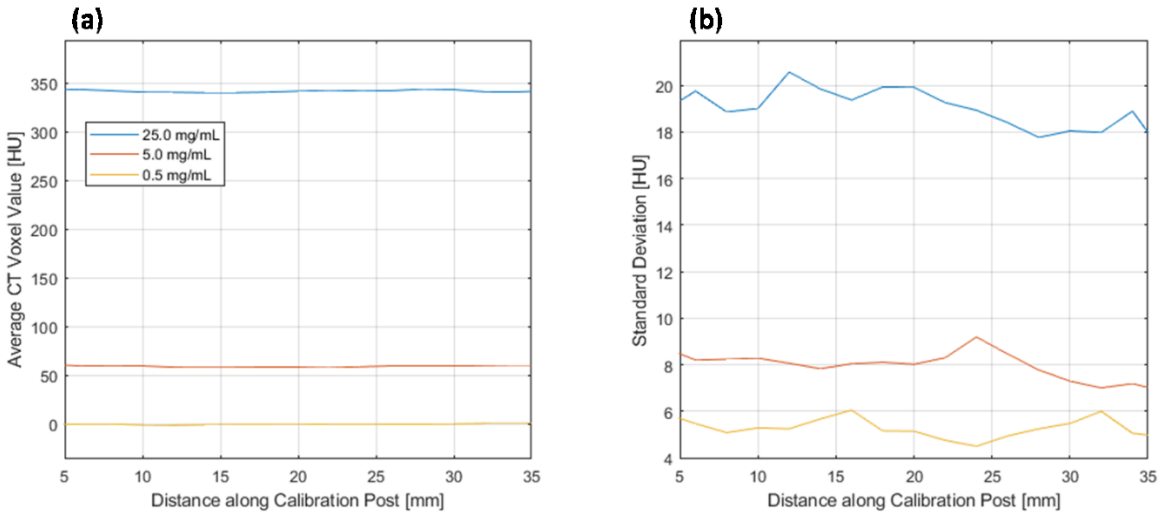

Figure 6.5: (a) Average HU in post structures as a function of post length. (b) HU standard deviation in post structures as a function of post length.

In Figure 6.6(a-c), radial profiles through the central CT slice of all nine post structures containing microsphere concentrations of 25.0 mg/mL, 5.0 mg/mL, and 0.5 mg/mL, respectively. The mean HU of the background region is also given as a baseline reference value. In the profile shown in Figure 6.6(a,b), HU values appear relatively constant for post structures having diameters greater than 2 mm. Average COV values within the post structure range from 0.02 to 0.06. Although still relatively uniform, the profiles through posts containing 5.0 mg/mL shown in Figure 6.6(b) begin to demonstrate the impact of CT image noise as the range of COV values increases from 0.04 to 0.11. The profiles through posts containing 0.5 mg/mL shown in Figure 6.6(c) are nearly indistinguishable from the CT image noise with COV values spanning more than two orders of magnitude (0.12 to 25.62). However, when averaging radial profiles over the entire length of a post, as shown in Figure 6.6(d), the profiles become distinctly recognizable relative to the background, although COV values still span two orders of magnitude (0.13 to 19.40). All COV values from the radial profiles are reported in Table 6.4.

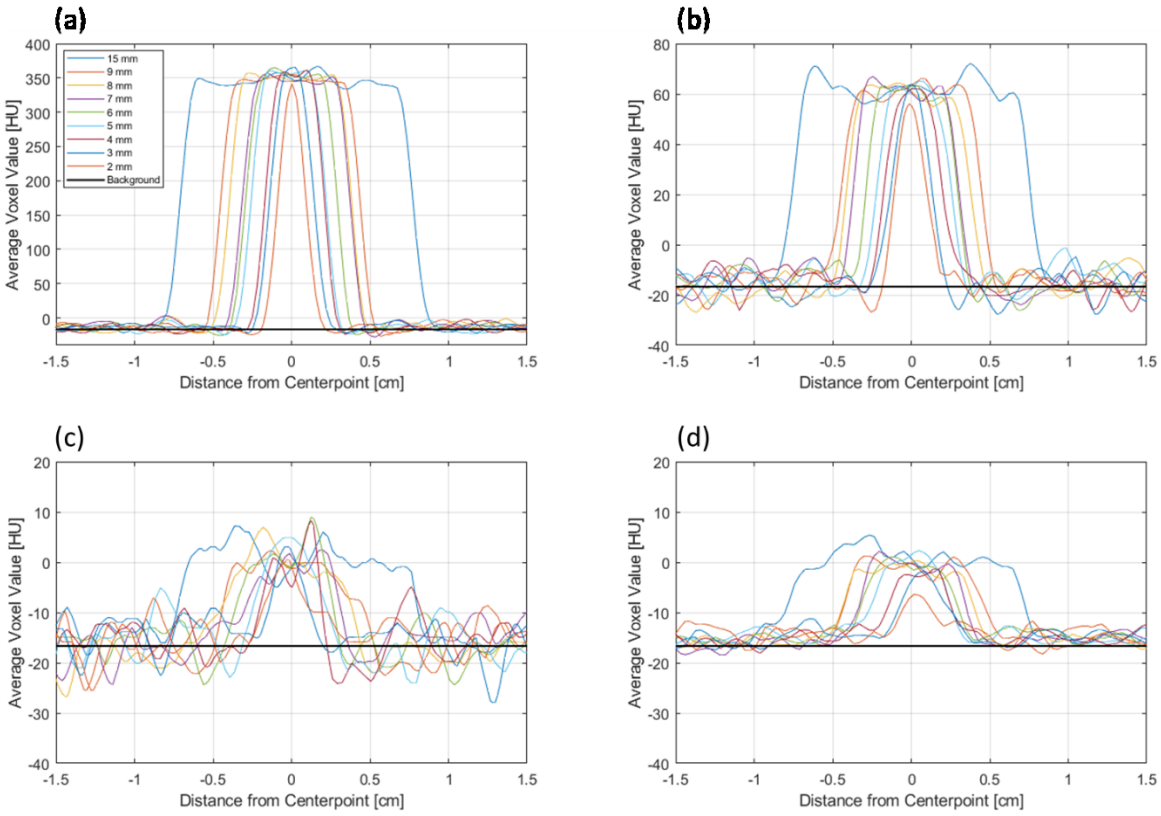

Figure 6.6: Radial profiles across the nine posts in the calibration phantom. (a) Profiles through posts having a microsphere concentration of 25.0 mg/mL. (b) Profiles through posts having a microsphere concentration of 5.0 mg/mL. (c) Profiles through posts having a microsphere concentration of 0.5 mg/mL. (d) Average over entire post length of radial profiles through posts having a microsphere concentration of 0.5 mg/mL.

Post Diameter [mm]	25.0 mg/mL COV	5.0 mg/mL COV	0.5 mg/mL COV	0.5 mg/mL (averaged) COV
15	0.03	0.08	7.58	19.40
9	0.03	0.09	12.07	0.81
8	0.03	0.09	25.62	0.58
7	0.03	0.08	3.21	0.81
6	0.02	0.11	3.01	1.18
5	0.02	0.07	2.05	2.31
4	0.03	0.04	0.37	0.42
3	0.06	0.09	1.52	0.59
2	0.06	0.06	0.12	0.13

Table 6.4: COV measurements for radial profiles within the post structures having microsphere concentrations of 25.0 mg/mL, 5.0 mg/mL, and 0.5 mg/mL.

6.4 Discussion

6.4.1 Image Co-Registration

The uncertainty associated with the image co-registration, as defined by the TRE, was on the order of a CT pixel dimension (~0.5 mm). The magnitude of this error suggests a negligible impact from image co-registration on the determination of m_{cal}.

6.4.2 Calibration Curves

Figure 6.1 suggest that varying tube current, slice thickness and FOV have no significant effects on the magnitude of m_{cal}. These results validate those from agarose phantom imaging where halving the FOV and slice thickness had no significant effect on m_{cal}. However, altering these parameters does influence the noise characteristics within the image (as well as the spatial resolution), and will consequently affect the LOD values as defined in Equations 5.9 and 5.10.

The calibration curves in Figure 6.2(b) indicate the lower the X-ray tube potential, the greater the magnitude of m_{cal}, suggesting that scans with lower tube potentials will improve microsphere concentration resolution, potentially enabling more accurate dosimetry estimates. As these scans were acquired with the scattering module to simulate a realistic patient size, the increase in image noise (particularly at the low tube potential of 80 kVp) produces additional uncertainty. Furthermore, the calibration curves in Figure 6.2(a) imply a family of curves should be generated to for large and small patients to account for the impact of scatter on the magnitude of m_{cal}.

As Figure 6.3 demonstrates, calibration curves derived from different CT models may have the same magnitude of m_{cal} for one tube potential, but different slope magnitudes at another (e.g., 100 kVp in Figure 6.3(b) and 140 kVp in Figure 6.3(a)). It is therefore essential to image the calibration phantom for each CT model, and not simply scale a calibration curve derived from another CT model by a HU offset. The cause of the slope deviation between tube potentials may be attributed to X-ray tube filtration. Differences between CT scanner filtration will produce differences in the X-ray energy spectra. This will result in changes in the microsphere attenuation properties, and hence the reconstructed voxel value. The temporal stability of the calibration phantom indicates it is

feasible to ship to a single calibration phantom to CT scanners at other institutions for imaging without any degradation to the phantom over time.

6.4.3 Limit of Detection

Despite the analysis being performed on image data acquired from different CT models and different tube potentials, Figure 6.4 suggests microsphere concentration detectability is approximately equal and the relationship between HU and microsphere concentration is stable across CT platforms. The difference of 0.04 mg/mL in $LOD_{mg/mL}$ is not clinically relevant. As in Section 5.6.2, we can apply Equation 5.11 to determine the corresponding ^{90}Y activity concentration given a microsphere concentration of 0.04 mg/mL, the number of microspheres per milligram MS_{mg} = 24,526 MS/mg, an average microsphere specific activity A_{MS} = 156 Bq. The calculation produces a ^{90}Y activity concentration equivalent to 0.15 MBq/mL, well below the detectability limits of both PET and CT (~1.0 MBq/mL).

6.4.4 Uniformity

The longitudinal HU profiles in Figure 6.5(a) indicate the microsphere uniformity is stable along the length of the calibration phantom posts. Although the standard deviation of HU values along the post increases with greater microsphere concentration, as demonstrated in Figure 6.5(b), the low COV values further suggest longitudinal homogeneity. Although there is a notable reduction of HU intensity in the radial profile of the 2 mm-diameter posts in Figure 6.6(a, b), the total microsphere mass (hence ^{90}Y activity) within the post structure can be recovered, as described in Section 5.6.1. The radial profiles of the posts (0.5 mg/mL) in Figure 6.6(c) are almost indistinguishable from the background, illustrating the challenge of quantification in low ^{90}Y activity regions. However, when averaged over multiple slices, the profiles are readily visible. This indicates that dose estimates in low activity regions are more likely to be accurate for larger features (i.e. the low microsphere uptake that produces a signature macroscopic “blush” region in CT images.).

The COV values in Table 6.4 for the calibration phantom posts having a microsphere concentration of 0.5 mg/mL span a wide range when compared to the posts

with larger microsphere concentrations. There are issues with this metric when applied to low microsphere concentration posts, particularly those with the smallest diameters. As the mean value approaches zero, the COV approaches infinity, hence the COV for these posts is sensitive to small changes in the mean. Furthermore, for posts with diameters not much greater than the axial voxel size, there is a lack of profile plateau due to partial volume effects. This produces a poor estimate of the mean HU value.

6.4.5 Future Work

Despite the results provided in this study, there is room for further analysis. For example, additional calibration phantoms based on the same schematic need to be analyzed to quantify the fabrication reproducibility. If multiple phantoms are to be used for CT calibration, it is essential to validate these phantoms are identical within a specified tolerance. Additionally, a longitudinal imaging study should be performed to ensure constancy in HU values over longer time scales.

The calibrations curves are generated based nominal microsphere concentration values of 0.5 mg/mL, 5.0 mg/mL, and 25.0 mg/mL. The high spatial resolution of μCT imaging can provide the means to quantify the true microsphere concentration of future calibration posts. This task is particularly important since the uncertainty of the glass concentrations within the calibration posts will be a major determinant of the confidence limits of the CT calibration method.

Finally, the impact of image reconstruction filters on the magnitude of m_{cal} has yet to be investigated. Preliminary work described in Section 3.6.3 revealed the smooth and sharp kernels (B10f and B80f, respectively) either overly accentuated image noise or unintentionally induced non-uniformities within the agarose hydrogel. The consequence of filter shape has on the magnitude of m_{cal} should be explored, particularly for calibration post structures with small diameters.

6.5 Conclusion

The resin-based calibration phantom has several properties that are well-suited to the needs of CT-based dosimetry in ^{90}Y TARE. The microsphere-loaded calibration posts appear to be uniform over a range of microsphere concentrations, they are physically robust

and unlikely to suffer from material decomposition over substantial periods of time, and the calibration curve slopes are immune to changes in slice thickness, tube current, and FOV, although altering these parameters will influence CT image noise and consequently impact the LOD. Calibration curves should be generated specific to a single CT scanner, and also for multiple effective patient thickness and range of X-ray tube potentials. The uncertainty associated with the measurement of the calibration curve slopes are minimal as indicated by the small range of slope confidence intervals.

Chapter 7 Discussion

7.1 Summary

The purpose of this thesis was to develop, implement, and validate a CT-based framework for post-treatment dosimetry in ^{90}Y TARE. The proposed framework provides the means to perform precision dosimetry and extract accurate dose metrics that may be used to refine the understanding of the dose-response relationship in ^{90}Y TARE.

The first manuscript developed a methodology to quantify the inherent radiopacity of radiopaque microspheres through CT imaging. This methodology produced a calibration curve that relates microsphere concentration within a CT voxel to the corresponding of HU for that voxel. Tissue-equivalent phantoms were designed to determine CT voxel enhancement from microspheres uniformly distributed within the phantoms. Phantoms were imaged with CT to determine the average HU and with brightfield microscopy to accurately quantify the microsphere concentration. The mean HU and microsphere concentration were found to be positively correlated (r^2 = 0.949) over a range of CT acquisition parameters. This findings in this manuscript provide a means to quantify the radiation dose from the infusion of radiopaque microspheres for more accurate dosimetry in ^{90}Y TARE, which may improve our understanding of the relationship between absorbed dose and tumour response. Furthermore, the results presented in the first manuscript motivated the construction of a clinical calibration phantom. The analysis of data provided by CT imaging of this clinical calibration phantom validated the work summarized by the first manuscript, while also demonstrating that the phantom is well-suited to the needs of CT-based dosimetry in ^{90}Y TARE.

The second manuscript described the implementation of a calibration curve to perform post-administration dosimetry in ^{90}Y TARE through μCT imaging of non-radioactive, radiopaque microsphere distributions in a porcine renal model, and also explored the impact of spatial resolution of an imaging system on the extraction of specific dose metrics. To produce an activity distribution, 400 MBq of ^{90}Y activity was distributed throughout segmented voxels of the embolized vasculature based on an established linear relationship between microsphere concentration and CT voxel value. This distribution was

downsampled to coarser isotropic grids ranging in voxel size from 2.5 mm to 15 mm to emulate nominal resolutions comparable to those found in ^{90}Y PET and bremsstrahlung SPECT imaging. Dose distributions were calculated through the convolution of activity distributions with DVKs generated using the GATE Monte Carlo toolkit. Contours were computed to represent normal tissue and target volumes. Dose-volume histograms, dose metrics, and dose profiles were compared to a ground truth dose distribution computed with GATE. The mean dose to the target for all studied voxel sizes was found to be within ~5% of the ground truth mean dose. D_{70} was shown to be strongly correlated with image voxel size of the dose distribution (r^2 = 0.897). As D_{70} is cited in the literature as an important dose metric, its dependence on voxel size suggests higher resolution dose distributions may provide new perspectives on dose-response relationships in ^{90}Y TARE. The work in this manuscript demonstrates that dose distributions with large voxels incorrectly homogenize the dose by attributing escalated doses to normal tissues and reduced doses in high dose target regions, and that CT imaging of radiopaque microsphere distributions can provide increased confidence in characterizing the absorbed dose heterogeneity in ^{90}Y TARE.

The third manuscript described the validation of a CT-based approach to dosimetry in ^{90}Y TARE through CT imaging of radiopaque microspheres in a rabbit liver model, and also compared extracted dose metrics to those produced from conventional PET-based dosimetry. A CT calibration phantom was designed to contain posts having nominal microsphere concentrations of 0.5 mg/mL, 5.0 mg/mL, and 25.0 mg/mL. The mean HU was extracted from the post volumes to generate a calibration curve to relate HU to microsphere concentration. A nominal bolus of 40 mg of microspheres was administered to the livers of eight rabbits followed by PET/CT imaging. A CT-based activity distribution was calculated through the application of the calibration curve to the CT liver volume. Post-treatment dosimetry was performed through the convolution of ^{90}Y DVKs and the PET- and CT-based cumulated activity distributions. The mean dose to the liver in PET- and CT-based dose distributions was compared through linear regression, ANOVA, and Bland-Altman analysis. A linear least-squares fit to the average HU and microsphere concentration data in the calibration phantom confirmed a strong correlation ($r^2 > 0.999$) with a slope of 14.13 HU/mg/mL. A poor correlation was found between the mean dose

derived from CT and PET ($r^2 = 0.374$) while the ANOVA analysis revealed statistically significant differences between the MIRD-derived mean dose and the PET- and CT-derived mean dose. Bland-Altman analysis predicted an offset of 15.0 Gy between the mean dose in CT and PET. The dose within the liver was shown to be more heterogeneous in CT than in PET with an average COV equal to 1.99 and 1.02, respectively. This manuscript revealed the benefits of a CT-based approach to post-treatment dosimetry in ^{90}Y TARE. These include improved visualization of the dose distribution, reduced partial volume effects, a better representation of dose heterogeneity, and the mitigation of respiratory motion effects. Post-treatment CT imaging of radiopaque microspheres in ^{90}Y TARE provides the means to perform precision dosimetry and extract accurate dose metrics used to refine the understanding of the dose-response relationship, which could ultimately improve future patient outcomes.

7.2 Future Work

The framework developed in this thesis has the potential to transform the current practice in post-treatment dosimetry in ^{90}Y TARE. Still, there are multiple research avenues that could be further explored.

As mentioned in Section 6.4.5, the clinical calibration phantom requires additional validation in terms of construction reproducibility, the measurement of the true microsphere concentration within the posts, and the impact of CT image reconstruction filters on HU quantification. A limitation of the calibration phantom that we developed previously is that the smallest post size is 2 mm in diameter, representing only the fourth or fifth branching generation of the hepatic artery.[186] An examination of posts with diameters < 2 mm would validate application of the calibration curve across all microsphere concentrations, including those observed in the most distal arterioles.

Additionally, a more complex and potentially more accurate calibration methodology could be explored using dual-energy CT imaging.[187] In this approach, two post-treatment CT scans following ^{90}Y TARE could be acquired, one with a high tube potential and one with a low tube potential. This would allow for dual-energy subtraction to extract a CT signal derived exclusively from radiopaque microspheres, but also presents additional challenges. Since most clinical CT scanners are not capable of simultaneous

dual-energy image acquisition, imaging would need to be performed twice with the implementation of a breath hold technique during each acquisition. This could pose significant CT image co-registration challenges which may render this technique impractical and highly inaccurate.

Improvements can also be made in the implementation of convolutional dosimetry. The composition of Eye90 microspheres includes high effective atomic number elements, and following neutron activation, other radioisotopes are also present in the microspheres. Due to the variable half-lives and relative abundances of these radioisotopes, the dose profile around a microsphere will evolve over time. The presence of the high density ($\rho \cong$ 3.3 g/cm^3) glass will also cause some degree of self-shielding. These combined effects suggest ^{90}Y DVKs should be calculated to account for radiopaque microsphere composition. Recently, MC simulations have been performed for derived DPKs using early radiopaque microsphere formulations.[188] The same methods could be used to study any future variations in radiopaque microsphere size and composition with respect to DVK generation, as well as the effect of clustering and self-shielding.

Although there doesn't seem to be any clinical consequence of performing convolutional dosimetry using DVKs calculated in water and soft tissue, inaccuracies will arise when the surrounding material differs significantly in its composition relative to water.[163] Inhomogeneities in the form of microsphere-loaded vessels may perturb the dose distribution in the vicinity of the vessel. The Fourier transform methods used in convolutional dosimetry are limited in the sense that they require a spatially invariant kernel, which is technically violated with the surrounding medium differs from water. In this case, DVK scaling methods may be sufficient to overcome this limitation in convolutional dosimetry, but the impact of tissue inhomogeneities on the absorbed dose calculation (due to radiopaque microspheres) warrants further exploration.[189–191]

A worthy avenue for future research is the pursuit of intra-procedural dosimetry in ^{90}Y TARE during the administration of radiopaque microspheres, as alluded to in Section 1.3.3. The lack of visibility of commercially available microspheres through fluoroscopic imaging means that clinicians cannot determine (during treatment) if the quantity and location of microsphere deposition within the target matches their intended treatment plan.

The ability to visualize the microsphere during their administration would be an invaluable tool for clinicians as it would provide the necessary feedback to guide the intervention, a prospect that is currently nonexistent in the current clinical paradigm. Specifically, a direct visualization of the microspheres during administration would have significant impact on TARE in multiple ways. First, confirmation of tumour targeting and adequacy of tumour coverage would permit an informed termination of administration. This would also reduce excess dose to healthy liver tissue that would result from further administration. Furthermore, the detection of sub-optimal targeting or coverage would prompt the interventional radiologist to reposition the microcatheter or identify and catheterize alternate arterial supply. In cases where adequate target coverage cannot be obtained, it would allow for the prioritization of these patients for additional therapy (additional ^{90}Y TARE or other treatment modalities, such as ablation or SBRT). In addition, microsphere visualization would permit quantitative evaluation of the 3D microsphere distribution during the procedure using CBCT. Together, intra-procedural fluoroscopy and CBCT imaging could provide a real-time estimate of the microsphere distribution. This, in turn, would facilitate a visualization of an estimate of the dose distribution and provide intra-procedural feedback to the interventional radiologist. The possibility of performing intra-procedural dosimetry in ^{90}Y TARE is not possible with commercially available microspheres due to their lack of inherent radiopacity. The implementation of microsphere tracking intra-procedural dosimetry in ^{90}Y TARE represents a massive leap forward in treatment delivery that would permit adaptive response to improve the quality and standardization of treatment and will lead to safer, more efficacious treatments.

7.3 Conclusions

In the modern practice of radiation oncology, accurate knowledge of the 3D dose distribution is essential for maximizing the safety and efficacy of treatment. Unfortunately, the current practices in post-treatment dosimetry in ^{90}Y TARE are lacking in predictive utility. The research presented in this thesis demonstrates the many advantages of implementing a CT-based approach to post-treatment dosimetry in ^{90}Y TARE. Specifically, we have shown that post-treatment CT imaging of radiopaque microsphere distributions is feasible, can provide the means to perform precision dosimetry in ^{90}Y

TARE, and allows for the extraction more accurate dose metrics relative to the conventional PET-based dosimetry. The presented framework has the potential to transform post-treatment dosimetry in ^{90}Y TARE by providing the means to fill the existing clinical knowledge gap that results from the lack of high quality, patient-specific dosimetric data. Furthermore, it will inspire future clinical studies that will reshape our understanding of the dose-response relationship in ^{90}Y TARE and potentially improve future patient outcomes.

Bibliography

1. Delaney G, Jacob S, Featherstone C, Barton M. The role of radiotherapy in cancer treatment: Estimating optimal utilization from a review of evidence-based clinical guidelines. *Cancer*. 2005;104(6):1129-1137. doi:10.1002/cncr.21324

2. Bernier J, Hall EJ, Giaccia A. Radiation oncology: A century of achievements. *Nat Rev Cancer*. 2004;4(9):737-747. doi:10.1038/nrc1451

3. Aird EGA, Conway J. CT simulation for radiotherapy treatment planning. *Br J Radiol*. 2002;75(900):937-949. doi:10.1259/bjr.75.900.750937

4. Kim DW, Park K, Kim H, Kim J. History of the Photon Beam Dose Calculation Algorithm in Radiation Treatment Planning System. *Prog Med Phys*. 2020;31(3):54-62. doi:10.14316/pmp.2020.31.3.54

5. Marks LB, Yorke ED, Jackson A, et al. Use of Normal Tissue Complication Probability Models in the Clinic. *Int J Radiat Oncol Biol Phys*. 2010;76(3 SUPPL.). doi:10.1016/j.ijrobp.2009.07.1754

6. Grimm J, Marks LB, Jackson A, Kavanagh BD, Xue J, Yorke E. High Dose per Fraction, Hypofractionated Treatment Effects in the Clinic (HyTEC): An Overview. *Int J Radiat Oncol Biol Phys*. 2021;110(1):1-10. doi:10.1016/j.ijrobp.2020.10.039

7. Emami B, Lyman J, Brown A, et al. Tolerance of normal tissue to therapeutic irradiation. *Int J Radiat Oncol Biol Phys*. 1991;21(1):109-122. doi:10.1016/0360-3016(91)90171-Y

8. Chargari C, Deutsch E, Blanchard P, et al. Brachytherapy: An overview for clinicians. *CA Cancer J Clin*. 2019;69(5):386-401. doi:10.3322/caac.21578

9. Gates VL, Esmail AAH, Marshall K, Spies S, Salem R. Internal pair production of 90Y permits hepatic localization of microspheres using routine PET: proof of concept. *J Nucl Med*. 2011;52(1):72-76. doi:10.2967/jnumed.110.080986

10. Elschot M, Nijsen JFW, Dam AJ, de Jong HWAM. Quantitative evaluation of scintillation camera imaging characteristics of isotopes used in liver radioembolization. *PLoS One*. 2011;6(11):e26174. doi:10.1371/journal.pone.0026174

11. Pasciak AS, Bourgeois AC, Bradley YC. A Comparison of Techniques for (90)Y PET/CT Image-Based Dosimetry Following Radioembolization with Resin Microspheres. *Front Oncol*. 2014;4:121. doi:10.3389/fonc.2014.00121 [doi]

12. Sung H, Ferlay J, Siegel RL, et al. Global Cancer Statistics 2020: GLOBOCAN Estimates of Incidence and Mortality Worldwide for 36 Cancers in 185 Countries. *CA Cancer J Clin*. 2021;71(3):209-249. doi:10.3322/caac.21660

13. Llovet JM, Fuster J, Bruix J. The Barcelona approach: Diagnosis, staging, and treatment of hepatocellular carcinoma. *Liver Transplant*. 2004;10(S2):S115-S120. doi:10.1002/LT.20034

14. Bruix J, Sherman M. Management of hepatocellular carcinoma: An update. *Hepatology*. 2011;53(3):1020-1022. doi:10.1002/hep.24199

15. Cabrera R, Nelson DR. Review article: The management of hepatocellular carcinoma. *Aliment Pharmacol Ther*. 2010;31(4):461-476. doi:10.1111/j.1365-2036.2009.04200.x

16. Statistics - MOTP Atlantic Canada. https://www.motpatlantic.ca/Quality/Statistics. Published 2019. Accessed October 3, 2021.

17. *Canadian Institute for Health Information. Annual Statistics on Organ Replacement in Canada: Dialysis, Transplantation and Donation, 2010 to 2019.*; 2019.

18. Groeschl RT, Clark Gamblin T, Turaga KK. Surgical Resection in Hepatocellular Carcinoma Patients with Minimal Background Fibrosis: A Strategy in the Era of Organ Shortage. *Ann Surg Oncol 2013 206*. 2013;20(6):2043-2048. doi:10.1245/S10434-012-2857-6

19. Eghtesad B, Aucejo F. Liver transplantation for malignancies. *J Gastrointest Cancer*. 2014;45(3):353-362. doi:10.1007/s12029-014-9590-2

20. Kim WR, Gores GJ, Benson JT, Therneau TM, Melton LJ. Mortality and hospital utilization for hepatocellular carcinoma in the United States. *Gastroenterology*. 2005;129(2):486-493. doi:10.1016/j.gastro.2005.05.001

21. Ahmed M. Image-guided tumor ablation: Standardization of terminology and reporting Criteria-A 10-year update. *Radiology*. 2014;273(1):241-260. doi:10.1148/radiol.14132958

22. Clark TWI. Chemical Ablation of Liver Cancer. *Tech Vasc Interv Radiol*. 2007;10(1):58-63. doi:10.1053/j.tvir.2007.08.004

23. Scheffer HJ, Nielsen K, de Jong MC, et al. Irreversible Electroporation for Nonthermal Tumor Ablation in the Clinical Setting: A Systematic Review of Safety and Efficacy. *J Vasc Interv Radiol*. 2014:1-15. doi:10.1016/j.jvir.2014.01.028

24. Kim S, Abou-Alfa GK. The role of tyrosine kinase inhibitors in hepatocellular carcinoma. *Clin Adv Hematol Oncol*. 2014;12(1):36-41.

25. Jianrui S, Zengqiang Q, Xianling G, et al. Hypoxia-induced autophagy contributes to the chemoresistance of hepatocellular carcinoma cells. *Autophagy*. 2009;5(8):1131-1144. doi:10.4161/auto.5.8.9996

26. Llovet JM, Ricci S, Mazzaferro V, et al. Sorafenib in Advanced Hepatocellular Carcinoma. *N Engl J Med*. 2008;359(4):378-390. doi:10.1056/nejmoa0708857

27. Kim J, Jung Y. Radiation-induced liver disease: current understanding and future perspectives. *Exp Mol Med 2017 497*. 2017;49(7):e359-e359. doi:10.1038/emm.2017.85

28. Benson R, Madan R, Kilambi R, Chander S. Radiation induced liver disease: A clinical update. *J Egypt Natl Canc Inst*. 2016;28(1):7-11. doi:10.1016/j.jnci.2015.08.001

29. Michel R, Françoise I, Laure P, Anouchka M, Guillaume P, Sylvain K. Dose to organ at risk and dose prescription in liver SBRT. *Reports Pract Oncol Radiother*. 2017;22(2):96-102. doi:10.1016/j.rpor.2017.03.001

30. Bujold A, Massey CA, Kim JJ, et al. Sequential phase I and II trials of stereotactic body radiotherapy for locally advanced hepatocellular carcinoma. *J Clin Oncol*. 2013;31(13):1631-1639. doi:10.1200/JCO.2012.44.1659

31. BREEDIS C, Young G. The blood supply of neoplasms in the liver. *Am J Pathol*. 1954;30(5):969.

32. Maluccio M, Covey A. Recent progress in understanding, diagnosing, and treating hepatocellular carcinoma. *CA Cancer J Clin*. 2012;62(6):394-399.

33. Maluccio MA, Covey AM, Porat L Ben, et al. Transcatheter Arterial Embolization with Only Particles for the Treatment of Unresectable Hepatocellular Carcinoma. *J Vasc Interv Radiol*. 2008;19(6):862-869. doi:10.1016/j.jvir.2008.02.013

34. Llovet JM, Real MI, Montaña X, et al. Arterial embolisation or chemoembolisation versus symptomatic treatment in patients with unresectable hepatocellular carcinoma: A randomised controlled trial. *Lancet*. 2002;359(9319):1734-1739. doi:10.1016/S0140-6736(02)08649-X

35. Zou JH, Zhang L, Ren ZG, Ye SL. Efficacy and safety of cTACE versus DEB-TACE in patients with hepatocellular carcinoma: a meta-analysis. *J Dig Dis*. 2016;17(8):510-517. doi:10.1111/1751-2980.12380

36. Rognoni C, Ciani O, Sommariva S, et al. Trans-arterial radioembolization in intermediate-advanced hepatocellular carcinoma: systematic review and meta-analyses. *Oncotarget*. 2016;7(44):72343.

37. Salem R, Mazzaferro V, Sangro B. Yttrium 90 radioembolization for the treatment of hepatocellular carcinoma: Biological lessons, current challenges, and clinical perspectives. *Hepatology*. 2013;58(6):2188-2197. doi:10.1002/hep.26382

38. Sato K, Lewandowski RJ, Bui JT, et al. Treatment of unresectable primary and metastatic liver cancer with yttrium-90 microspheres (TheraSphere®): Assessment of hepatic arterial embolization. *Cardiovasc Intervent Radiol*. 2006;29(4):522-529. doi:10.1007/s00270-005-0171-4

39. Oladeru OT, Miccio JA, Yang J, Xue Y, Ryu S, Stessin AM. Conformal external beam radiation or selective internal radiation therapy—a comparison of treatment outcomes for hepatocellular carcinoma. *J Gastrointest Oncol*. 2016;7(3):433. doi:10.21037/JGO.2015.10.04

40. Mohamed M, Katz AW, Tejani MA, et al. Comparison of outcomes between SBRT, yttrium-90 radioembolization, transarterial chemoembolization, and radiofrequency ablation as bridge to transplant for hepatocellular carcinoma. *Adv Radiat Oncol*. 2016;1(1):35-42. doi:10.1016/J.ADRO.2015.12.003

41. Musunruu HB, Keller A, Celebrezze J, et al. Bridge-to-Transplant External-Beam Radiation Therapy in Patients With Hepatocellular Carcinoma: A Utilization Analysis of the United Network for Organ Sharing (UNOS) Database. *Int J Radiat Oncol Biol Phys*. 2021;111(3):e62-e63. doi:10.1016/J.IJROBP.2021.07.411

42. Salem R, Lewandowski RJ, Mulcahy MF, et al. Radioembolization for Hepatocellular Carcinoma Using Yttrium-90 Microspheres: A Comprehensive Report of Long-term Outcomes. *Gastroenterology*. 2010;138(1):52-64. doi:10.1053/J.GASTRO.2009.09.006

43. Salem R, Lewandowski RJ, Kulik L, et al. Radioembolization Results in Longer Time-to-Progression and Reduced Toxicity Compared With Chemoembolization in Patients With Hepatocellular Carcinoma. *Gastroenterology*. 2011;140(2):497-507.e2. doi:10.1053/J.GASTRO.2010.10.049

44. Sangro B, Carpanese L, Cianni R, et al. Survival after yttrium-90 resin microsphere radioembolization of hepatocellular carcinoma across Barcelona clinic liver cancer stages: A European evaluation. *Hepatology*. 2011;54(3):868-878. doi:10.1002/HEP.24451

45. Mazzaferro V, Sposito C, Bhoori S, et al. Yttrium-90 radioembolization for intermediate-advanced hepatocellular carcinoma: A phase 2 study. *Hepatology*. 2013;57(5):1826-1837. doi:10.1002/hep.26014

46. Saini A, Wallace A, Alzubaidi S, et al. History and Evolution of Yttrium-90 Radioembolization for Hepatocellular Carcinoma. *J Clin Med*. 2019;8(1):55. doi:10.3390/jcm8010055

47. Sacco R, Mismas V, Marceglia S, et al. Transarterial radioembolization for hepatocellular carcinoma: An update and perspectives. *World J Gastroenterol*. 2015;21(21):6518. doi:10.3748/WJG.V21.I21.6518

48. Sasson AR, Sigurdson ER. Surgical treatment of liver metastases. *Semin Oncol*. 2002;29(2):107-118. doi:10.1053/sonc.2002.31676

49. Kennedy A, Nag S, Salem R, et al. Recommendations for radioembolization of hepatic malignancies using yttrium-90 microsphere brachytherapy: a consensus panel report from the radioembolization brachytherapy oncology consortium. *Int J Radiat Oncol Biol Phys*. 2007;68(1):13-23. doi:S0360-3016(07)00097-1 [pii]

50. Dezarn WA, Cessna JT, DeWerd LA, et al. Recommendations of the American Association of Physicists in Medicine on dosimetry, imaging, and quality assurance procedures for 90Y microsphere brachytherapy in the treatment of hepatic malignancies. *Med Phys*. 2011;38(8):4824-4845.

51. Levillain H, Bagni O, Deroose CM, et al. International recommendations for personalised selective internal radiation therapy of primary and metastatic liver diseases with yttrium-90 resin microspheres. *Eur J Nucl Med Mol Imaging*. 2021;48(5):1570-1584. doi:10.1007/s00259-020-05163-5

52. Medicine BTGI. *Package Insert - TheraSphere® Yttrium-90 Glass Microspheres*.

53. Limited SM. *Sirtex Medical Training Manual*.

54. Kennedy AS, Nutting C, Coldwell D, Gaiser J, Drachenberg C. Pathologic response and microdosimetry of 90Y microspheres in man: Review of four explanted whole livers. *Int J Radiat Oncol Biol Phys*. 2004;60(5):1552-1563. doi:10.1016/j.ijrobp.2004.09.004

55. Chiesa C, Mira M, Maccauro M, et al. Radioembolization of hepatocarcinoma with 90Y glass microspheres: development of an individualized treatment planning strategy based on dosimetry and radiobiology. *Eur J Nucl Med Mol Imaging*. 2015;42(11):1718-1738. doi:10.1007/s00259-015-3068-8

56. Strigari L, Sciuto R, Rea S, et al. Efficacy and toxicity related to treatment of hepatocellular carcinoma with 90Y-SIR spheres: Radiobiologic considerations. *J Nucl Med*. 2010;51(9):1377-1385. doi:10.2967/jnumed.110.075861

57. Walrand S, Hesse M, Chiesa C, Lhommel R, Jamar F. The low hepatic toxicity per Gray of 90Y glass microspheres is linked to their transport in the arterial tree favoring a nonuniform trapping as observed in posttherapy PET imaging. *J Nucl Med*. 2014;55(1):135-140. doi:10.2967/jnumed.113.126839 [doi]

58. Volchok HL, Kulp JL. Half-life of yttrium-90. *Phys Rev*. 1955;97(1):102. doi:10.1103/PhysRev.97.102

59. Cross WG, Soares CG, Vynckier S, Weaver K. Dosimetry of Beta Rays and Low-Energy Photons for Brachytherapy with Sealed Sources. *J ICRU*. 2004;4(2):5-8. doi:10.1093/jicru_ndh020

60. Bé MM, Chisté V, Dulieu C, et al. Table of Radionuclides (vol. 3–A= 3 to 244). *Monogr BIPM*. 2006;5.

61. Mainegra-Hing E, Rogers DWO, Kawrakow I. Calculation of photon energy deposition kernels and electron dose point kernels in water. *Med Phys*. 2005;32(3):685-699. doi:10.1118/1.1861412

62. Kim SP, Cohalan C, Kopek N, Enger SA. A guide to 90Y radioembolization and its dosimetry. *Phys Medica*. 2019;68:132-145. doi:10.1016/j.ejmp.2019.09.236

63. Deng M, Ng SWY, Cheung ST, Chong CCN. Clinical application of Albumin-Bilirubin (ALBI) score: The current status. *Surgeon*. 2020;18(3):178-186. doi:10.1016/j.surge.2019.09.002

64. Braat AJAT, Smits MLJ, Braat MNGJA, et al. 90Y hepatic radioembolization: An update on current practice and recent developments. *J Nucl Med*. 2015;56(7):1079-1087. doi:10.2967/jnumed.115.157446

65. Michels NA. Collateral arterial pathways to the liver after ligation of the hepatic artery and removal of the celiac axis. *Cancer*. 1953;6(4):708-724. doi:10.1002/1097-0142(195307)6:4<708::AID-CNCR2820060411>3.0.CO;2-A

66. Kappadath SC, Lopez BP, Salem R, Lam MGEH. Reassessment of the lung dose limits for radioembolization. *Nucl Med Commun*. 2021;42(10):1064-1075. doi:10.1097/mnm.0000000000001439

67. Haste P, Tann M, Persohn S, et al. Correlation of Technetium-99m Macroaggregated Albumin and Yttrium-90 Glass Microsphere Biodistribution in Hepatocellular Carcinoma: A Retrospective Review of Pretreatment Single Photon Emission CT and Posttreatment Positron Emission Tomography/CT. *J Vasc Interv Radiol*. 2017;28(5):722-730.e1. doi:10.1016/j.jvir.2016.12.1221

68. Flamen P, Vanderlinden B, Delatte P, et al. Multimodality imaging can predict the metabolic response of unresectable colorectal liver metastases to radioembolization therapy with Yttrium-90 labeled resin microspheres. *Phys Med Biol*. 2008;53(22):6591-6603. doi:10.1088/0031-9155/53/22/019 [doi]

69. Kao YH, Tan AEH, Burgmans MC, et al. Image-guided personalized predictive dosimetry by artery-specific SPECT/CT partition modeling for safe and effective 90Y radioembolization. *J Nucl Med*. 2012;53(4):559-566. doi:10.2967/jnumed.111.097469 [doi]

70. Garin E, Lenoir L, Rolland Y, et al. Dosimetry based on 99mTc-macroaggregated albumin SPECT/CT accurately predicts tumor response and survival in hepatocellular carcinoma patients treated with 90Y-loaded glass microspheres: Preliminary results. *J Nucl Med*. 2012;53(2):255-263. doi:10.2967/jnumed.111.094235

71. Gray B, Van Hazel G, Hope M, et al. Randomised trial of SIR-Spheres® plus chemotherapy vs. chemotherapy alone for treating patients with liver metastases from primary large bowel cancer. *Ann Oncol*. 2001;12(12):1711-1720. doi:10.1023/A:1013569329846

72. Vauthey JN, Abdalla EK, Doherty DA, et al. Body surface area and body weight predict total liver volume in western adults. *Liver Transplant*. 2002;8(3):233-240. doi:10.1053/jlts.2002.31654

73. Lam MGEH, Louie JD, Abdelmaksoud MHK, Fisher GA, Cho-Phan CD, Sze DY. Limitations of body surface area-based activity calculation for radioembolization of hepatic metastases in colorectal cancer. *J Vasc Interv Radiol*. 2014;25(7):1085-1093. doi:10.1016/j.jvir.2013.11.018

74. Kao YH, Tan EH, Ng CE, Goh SW. Clinical implications of the body surface area method versus partition model dosimetry for yttrium-90 radioembolization using resin microspheres: a technical review. *Ann Nucl Med*. 2011;25(7):455-461. doi:10.1007/s12149-011-0499-6 [doi]

75. Bernardini M, Smadja C, Faraggi M, et al. Liver Selective Internal Radiation Therapy with 90Y resin microspheres: Comparison between pre-treatment activity calculation methods. *Phys Medica*. 2014;30(7):752-764. doi:10.1016/j.ejmp.2014.05.004

76. Seppenwoolde JH, Bartels LW, Van Der Weide R, Nijsen JFW, Van Het Schip AD, Bakker CJG. Fully MR-guided hepatic artery catheterization for selective drug delivery: A feasibility study in pigs. *J Magn Reson Imaging*. 2006. doi:10.1002/jmri.20479

77. Walrand S, Hesse M, Demonceau G, Pauwels S, Jamar F. Yttrium-90-labeled microsphere tracking during liver selective internal radiotherapy by bremsstrahlung pinhole SPECT: Feasibility study and evaluation in an abdominal phantom. *EJNMMI Res*. 2011. doi:10.1186/2191-219X-1-32

78. Jiang J, Li K, Komarov S, O'Sullivan JA, Tai YC. Feasibility study of a point-of-care positron emission tomography system with interactive imaging capability. *Med Phys*. 2019. doi:10.1002/mp.13397

79. Beijst C, Elschot M, Viergever MA, de Jong HWAM. Toward simultaneous real-time fluoroscopic and nuclear imaging in the intervention room. *Radiology*. 2016;278(1):232-238.

80. Rault E, Staelens S, Van Holen R, De Beenhouwer J, Vandenberghe S. Fast simulation of yttrium-90 bremsstrahlung photons with GATE. *Med Phys*. 2010;37(6):2943-2950. doi:10.1118/1.3431998

81. Rong X, Du Y, Frey EC. A method for energy window optimization for quantitative tasks that includes the effects of model-mismatch on bias: Application to Y-90 bremsstrahlung SPECT imaging. *Phys Med Biol*. 2012;57(12):3711-3725. doi:10.1088/0031-9155/57/12/3711

82. Rong X, Du Y, Ljungberg M, Rault E, Vandenberghe S, Frey EC. Development and evaluation of an improved quantitative 90Y bremsstrahlung SPECT method. *Med Phys*. 2012;39(5):2346-2358. doi:10.1118/1.3700174

83. Nickles R, Baldock C, Selwyn RG, et al. A new internal pair production branching ratio of 90Y: The development of a non-destructive assay for 90Y and 90Sr A new internal pair production branching ratio of 90 Y: The development of a non-destructive assay for 90 Y and 90 Sr. *Appl Radiat Isot*. 2007;65:318-327. doi:10.1016/j.apradiso.2006.08.009

84. Ford KW. Predicted 0+ level in Zr9040 [6]. *Phys Rev*. 1955;98(5):1516-1517. doi:10.1103/PhysRev.98.1516

85. Lhommel R, Goffette P, Van Den Eynde M, et al. Yttrium-90 TOF PET scan demonstrates high-resolution biodistribution after liver SIRT. *Eur J Nucl Med Mol Imaging*. 2009;36(10):1696. doi:10.1007/s00259-009-1210-1

86. Kao YH, Steinberg JD, Tay YS, et al. Post-radioembolization yttrium-90 PET/CT-part 1: Diagnostic reporting. *EJNMMI Res*. 2013;3(1):1-28. doi:10.1186/2191-219X-3-56

87. Conti M. State of the art and challenges of time-of-flight PET. *Phys Medica*. 2009;25(1):1-11. doi:10.1016/j.ejmp.2008.10.001

88. Carlier T, Willowson KP, Fourkal E, Bailey DL, Doss M, Conti M. 90Y -PET imaging: Exploring limitations and accuracy under conditions of low counts and high random fraction. *Med Phys*. 2015;42(7):4295-4309. doi:10.1118/1.4922685

89. Fox RA, Klemp PFB, Egan G, Mina LL, Burton MA, Gray BN. Dose distribution following selective internal radiation therapy. *Int J Radiat Oncol Biol Phys*. 1991;21(2):463-467. doi:10.1016/0360-3016(91)90797-8

90. Roberson PL, Ten RKH, McShan DL, et al. Three-dimensional tumor dosimetry for hepatic yttrium-90-microsphere therapy. *J Nucl Med Off Publ Soc Nucl Med*. 1992;33(5):735-738.

91. Campbell AM, Bailey IH, Burton MA. Analysis of the distribution of intra-arterial microspheres in human liver following hepatic yttrium-90 microsphere therapy. *Phys Med Biol*. 2000;45(4):1023-1033. doi:10.1088/0031-9155/45/4/316

92. Campbell AM, Bailey IH, Burton MA. Tumour dosimetry in human liver following hepatic yttrium-90 microsphere therapy. *Phys Med Biol*. 2001;46(2):487-498. doi:10.1088/0031-9155/46/2/315

93. Lau WY, Leung WT, Ho S, et al. Treatment of inoperable hepatocellular carcinoma with intrahepatic arterial yttrium-90 microspheres: a phase I and II study. *Br J Cancer*. 1994;70(5):994.

94. Gulec SA, Mesoloras G, Dezarn WA, McNeillie P, Kennedy AS. Safety and efficacy of Y-90 microsphere treatment in patients with primary and metastatic liver cancer: The tumor selectivity of the treatment as a function of tumor to liver flow ratio. *J Transl Med 2007 51*. 2007;5(1):1-9. doi:10.1186/1479-5876-5-15

95. Pasciak AS, Bradley Y, McKinney JM. *Handbook of Radioembolization: Physics, Biology, Nuclear Medicine, and Imaging*. CRC Press; 2016.

96. Hunter RD. WHO handbook for reporting results of cancer treatment. *Int J Radiat Biol*. 1980;38(4):481-481. doi:10.1080/09553008014551861

97. Bruix J, Sherman M, Llovet JM, et al. Clinical management of hepatocellular carcinoma. Conclusions of the Barcelona-2000 EASL conference. *J Hepatol*. 2001;35(3):421-430. doi:10.1016/S0168-8278(01)00130-1

98. Therasse P, Arbuck SG, Eisenhauer EA, et al. New guidelines to evaluate the response to treatment in solid tumors. *J Natl Cancer Inst*. 2000;92(3):205-216. doi:10.1093/jnci/92.3.205

99. Lencioni R, Llovet JM. Modified recist (mRECIST) assessment for hepatocellular carcinoma. *Semin Liver Dis*. 2010;30(1):52-60. doi:10.1055/s-0030-1247132

100. O' Doherty J, O'Doherty J, O'Doherty J. A review of 3D image-based dosimetry, technical considerations and emerging perspectives in 90Y microsphere therapy. *J diagnostic imaging Ther*. 2015;2(2):1-34. doi:10.17229/jdit.2015-0428-016 [doi]

101. Roosen J, Klaassen NJM, Westlund Gotby LEL, et al. To 1000 Gy and back again: a systematic review on dose-response evaluation in selective internal radiation therapy for primary and secondary liver cancer. *Eur J Nucl Med Mol Imaging*. April 2021:1-15. doi:10.1007/s00259-021-05340-0

102. Kokabi N, Galt JR, Xing M, et al. A simple method for estimating dose delivered to hepatocellular carcinoma after yttrium-90 glass-based radioembolization therapy: preliminary results of a proof of concept study. *J Vasc Interv Radiol*. 2014;25(2):277-287. doi:10.1016/j.jvir.2013.11.007 [doi]

103. Kappadath SC, Mikell J, Balagopal A, Baladandayuthapani V, Kaseb A, Mahvash A. Hepatocellular Carcinoma Tumor Dose Response After 90Y-radioembolization With Glass Microspheres Using 90Y-SPECT/CT-Based Voxel Dosimetry. *Int J Radiat Oncol Biol Phys*. 2018;102(2):451-461. doi:10.1016/j.ijrobp.2018.05.062

104. Garin E, Tselikas L, Guiu B, et al. Personalised versus standard dosimetry approach of selective internal radiation therapy in patients with locally advanced hepatocellular carcinoma (DOSISPHERE-01): a randomised, multicentre, open-label phase 2 trial. *Lancet Gastroenterol Hepatol*. 2021;6(1):17-29. doi:10.1016/S2468-1253(20)30290-9

105. Kao YH, Steinberg JD, Tay YS, et al. Post-radioembolization yttrium-90 PET/CT - part 2: dose-response and tumor predictive dosimetry for resin microspheres. *EJNMMI Res*. 2013;3(1):5-57. doi:10.1186/2191-219X-3-57 [doi]

106. Willowson KP, Hayes AR, Chan DLH, et al. Clinical and imaging-based prognostic factors in radioembolisation of liver metastases from colorectal cancer: a retrospective exploratory analysis. *EJNMMI Res*. 2017;7(1). doi:10.1186/s13550-017-0292-1

107. Sgouros G, Hobbs RF. Dosimetry for radiopharmaceutical therapy. *Semin Nucl Med*. 2014;44(3):172-178. doi:10.1053/j.semnuclmed.2014.03.007 [doi]

108. Kim CR, Kim B, Ning MS, et al. Cost Analysis of PET/CT Versus CT as Surveillance for Stage III Non–Small-Cell Lung Cancer After Definitive Radiation Therapy. *Clin Lung Cancer*. 2018;19(4):e517-e528. doi:10.1016/j.cllc.2018.03.012

109. Orlacchio A, Ciarrapico AM, Schillaci O, et al. PET-CT in oncological patients: Analysis of informal care costs in cost-benefit assessment. *Radiol Medica*. 2014;119(4):283-289. doi:10.1007/s11547-013-0340-5

110. Attix FH. Introduction to Radiological Physics and Radiation Dosimetry. *Introd to Radiol Phys Radiat Dosim*. November 1986. doi:10.1002/9783527617135

111. Hubbell JH. Photon mass attenuation and mass energy absorption coefficients for H, C, N, O, Ar, and seven mixtures from 0.1 keV to 20 MeV. *Radiat Res*. 1977;70(1):58-81. doi:10.2307/3574732

112. Klein O, Nishina T. Über die Streuung von Strahlung durch freie Elektronen nach der neuen relativistischen Quantendynamik von Dirac. *Zeitschrift für Phys*. 1929;52(11-12):853-868. doi:10.1007/BF01366453

113. Robley D Evans. *The Atomic Nucleus*. Bombay - New Delhi: McGraw Hill; 1955.

114. Stabin MG, Eckerman KF, Ryman JC, Williams LE. Bremsstrahlung radiation dose in yttrium-90 therapy applications. *J Nucl Med*. 1994;35(8):1377-1380.

115. Loevinger R, Budinger TF, Watson EE. *MIRD Primer for Absorbed Dose Calculations*. Society of Nuclear Medicine; 1988.

116. Stabin MG, Siegel JA. Physical models and dose factors for use in internal dose assessment. *Health Phys*. 2003;85(3):294-310.

117. RADAR - Radiation Dose Assessment Resource. The Decay Data. https://www.doseinfo-radar.com/RADARDecay.html. Published 2005. Accessed September 3, 2021.

118. Sarrut D, Bardiès M, Boussion N, et al. A review of the use and potential of the GATE Monte Carlo simulation code for radiation therapy and dosimetry applications. *Med Phys*. 2014;41(6):64301-64302. doi:10.1118/1.4871617

119. Boone JM, McCollough CH. Computed tomography turns 50. *PhT*. 2021;74(9):34-40. doi:10.1063/PT.3.4834

120. Charles M. Effects of Ionizing Radiation: United Nations Scientific Committee on the Effects of Atomic Radiation: UNSCEAR 2006 Report, Volume 1--Report to the General Assembly, with Scientific Annexes A and B. *Radiat Prot Dosimetry*. 2010;138(2):187-189. doi:10.1093/rpd/ncp262

121. Bushberg JT, Seibert JA, Leidholdt EM, Boone JM, Goldschmidt EJ. The Essential Physics of Medical Imaging. *Med Phys*. 2003;30(7):1936-1936. doi:10.1118/1.1585033

122. Radon J. on the Determination of Functions From Their Integral Values Along Certain Manifolds. *IEEE Trans Med Imaging*. 1986;MI-5(4):170-176. doi:10.1109/tmi.1986.4307775

123. Shepp LA, Logan BF. Fourier Reconstruction of a Head Section. *IEEE Trans Nucl Sci*. 1974;NS-21(3):21-43. doi:10.1109/tns.1974.6499235

124. Cherry S, Sorenson J, Phelps M. Physics in Nuclear Medicine. *Phys Nucl Med*. 2012. doi:10.1016/C2009-0-51635-2

125. Willowson KP, Tapner M, Team QI, Bailey DL. A multicentre comparison of quantitative (90)Y PET/CT for dosimetric purposes after radioembolization with resin microspheres : The QUEST Phantom Study. *Eur J Nucl Med Mol Imaging*. 2015;42(8):1202-1222. doi:10.1007/s00259-015-3059-9 [doi]

126. Bailey DL, Karp JS, Surti S. Physics and Instrumentation in PET. *Positron Emiss Tomogr*. July 2006. doi:10.1007/1-84628-007-9_2

127. Ollinger JM. Model-based scatter correction for fully 3D PET. *Phys Med Biol*. 1996;41(1):153-176. doi:10.1088/0031-9155/41/1/012

128. Watson CC, Newport D, Casey ME. A Single Scatter Simulation Technique for Scatter Correction in 3D PET. 1996:255-268. doi:10.1007/978-94-015-8749-5_18

129. Accorsi R, Adam LE, Werner ME, Karp JS. Optimization of a fully 3D single scatter simulation algorithm for 3D PET. *Phys Med Biol*. 2004;49(12):2577-2598. doi:10.1088/0031-9155/49/12/008

130. Tong S, Alessio AM, Kinahan PE. Image reconstruction for PET/CT scanners: past achievements and future challenges. *Imaging Med*. 2010;2(5):529. doi:10.2217/IIM.10.49

131. Fourkal E, Veltchev I, Lin M, et al. 3D inpatient dose reconstruction from the PET-CT imaging of 90Y microspheres for metastatic cancer to the liver: feasibility study. *Med Phys*. 2013;40(8):081702. doi:10.1118/1.4810939 [doi]

132. Zimmerman E, Ratel G. Report of the CIPM key comparison CCRI(II)-K2.Y-90. *Metrologia*. 2005;42(SUPPL.):06001. doi:10.1088/0026-1394/42/1A/06001

133. Choti MA, Bulkley GB. Management of hepatic metastases. *Liver Transplant Surg*. 1999;5(1):65-80.

134. Russell AH, Clyde C, Wasserman TH, Turner SS, Rotman M. Accelerated hyperfractionated hepatic irradiation in the management of patients with liver metastases: results of the RTOG dose escalating protocol. *Int J Radiat Oncol Biol Phys*. 1993;27(1):117-123.

135. Srinivas SM, Natarajan N, Kuroiwa J, et al. Determination of radiation absorbed dose to primary liver tumors and normal liver tissue using post radioembolization 90Y PET. *Front Oncol*. 2014;4(SEP):255. doi:10.3389/fonc.2014.00255

136. Willowson K, Forwood N, Jakoby BW, Smith AM, Bailey DL. Quantitative 90Y image reconstruction in PET. *Med Phys*. 2012;39(11):7153-7159.

137. Siman W, Mikell JK, Kappadath SC. Practical reconstruction protocol for quantitative 90Y bremsstrahlung SPECT/CT. *Med Phys*. 2016;43(9):5093-5103.

138. Goldman LW. Principles of CT and CT technology. *J Nucl Med Technol*. 2007;35(3):115-128.

139. Zhang XF, Bligh M, Heelan F, et al. Towards personalized radioembolization with glass microspheres: an examination of new Yttrium-90 glasses with intrinsic radiopacity. *Cardiovasc Intervent Radiol*. 2016;39(3):S27-S280.

140. Narayanan J, Xiong J-Y, Liu X-Y. Determination of agarose gel pore size: Absorbance measurements vis a vis other techniques. *J Phys Conf Ser*. 2006;28(1):017. doi:10.1088/1742-6596/28/1/017

141. Lee PY, Costumbrado J, Hsu C-Y, Kim YH. Agarose Gel Electrophoresis for the Separation of DNA Fragments. *JoVE (Journal Vis Exp*. 2012;(62):e3923. doi:10.3791/3923

142. Furlan A, Marin D, Vanzulli A, et al. Hepatocellular carcinoma in cirrhotic patients at multidetector CT: hepatic venous phase versus delayed phase for the detection of tumour washout. *Br J Radiol*. 2011;84(1001):403-412.

143. Duda RO, Hart PE. Use of the Hough transformation to detect lines and curves in pictures. *Comm ACM*. 1971;15(1):11-15.

144. Organization IS. ISO 11843-1: Capability of detection-Part 1: Terms and definitions. 1997.

145. Jacobsen MC, Duan X, Cody DD, Cressman E, Schellingerhout D, Layman RR. Determination of the limit of detection for iodinated contrast agents with multi-energy computed tomography. In: *Medical Imaging 2018: Physics of Medical Imaging*. Vol 10573. International Society for Optics and Photonics; 2018:105734Q.

146. Andrade JM, Estévez-Pérez MG. Statistical comparison of the slopes of two regression lines: a tutorial. *Anal Chim Acta*. 2014;838:1-12.

147. Massey FJ. The Kolmogorov-Smirnov Test for Goodness of Fit. *J Am Stat Assoc*. 1951;46(253):68-78. doi:10.1080/01621459.1951.10500769

148. Boas FE, Fleischmann D. CT artifacts: causes and reduction techniques. *Imaging Med*. 2012;4(2):229-240.

149. Weg N, Scheer MR, Gabor MP. Liver lesions: improved detection with dual-detector-array CT and routine 2.5-mm thin collimation. *Radiology*. 1998;209(2):417-426.

150. Cropp RJ, Seslija P, Tso D, Thakur Y. Scanner and kVp dependence of measured CT numbers in the ACR CT phantom. *J Appl Clin Med Phys*. 2013;14(6):338-349. doi:10.1120/jacmp.v14i6.4417

151. Chang BK, Timmerman RD. Stereotactic body radiation therapy: A comprehensive review. *Am J Clin Oncol Cancer Clin Trials*. 2007;30(6):637-644. doi:10.1097/COC.0b013e3180ca7cb1

152. Bertuccio P, Turati F, Carioli G, et al. Global trends and predictions in hepatocellular carcinoma mortality. *J Hepatol*. 2017;67(2):302-309. doi:10.1016/j.jhep.2017.03.011

153. Espey DK, Wu XC, Swan J, et al. Annual report to the nation on the status of cancer, 1975-2004, featuring cancer in American Indians and Alaska Natives. *Cancer*. 2007;110(10):2119-2152. doi:10.1002/cncr.23044

154. Di Maio M, Daniele B, Gallo C, Perrone F. Re: Design and endpoints of clinical trials in hepatocellular carcinoma. *J Natl Cancer Inst*. 2008;100(21):1557. doi:10.1093/jnci/djn341

155. Chiesa C, Lambert B, Maccauro M, et al. Pretreatment Dosimetry in HCC Radioembolization with (90)Y Glass Microspheres Cannot Be Invalidated with a Bare Visual Evaluation of (99m)Tc-MAA Uptake of Colorectal Metastases Treated with Resin Microspheres. *J Nucl Med*. 2014;55(7):1216-1218. doi:10.2967/jnumed.113.129361 [doi]

156. Spina JC, Hume I, Pelaez A, Peralta O, Quadrelli M, Monaco RG. Expected and unexpected imaging findings after 90 Y transarterial radioembolization for liver tumors. *Radiographics*. 2019. doi:10.1148/rg.2019180095

157. Courtney Henry E, Mawko G, Tonkopi E, et al. Quantification of the inherent radiopacity of glass microspheres for precision dosimetry in yttrium-90 radioembolization. *Biomed Phys Eng Express*. 2019;5(5). doi:10.1088/2057-1976/ab36c2

158. Jan S, Santin G, Strul D, et al. GATE: A simulation toolkit for PET and SPECT. *Phys Med Biol*. 2004;49(19):4543-4561. doi:10.1088/0031-9155/49/19/007

159. Maigne L, Perrot Y, Schaart DR, Donnarieix D, Breton V. Comparison of GATE/GEANT4 with EGSnrc and MCNP for electron dose calculations at energies between 15 keV and 20 MeV. *Phys Med Biol*. 2011;56(3):811-827. doi:10.1088/0031-9155/56/3/017

160. Kallini JR, Gabr A, Thorlund K, et al. Comparison of the Adverse Event Profile of TheraSphere® with SIR-Spheres® for the Treatment of Unresectable Hepatocellular Carcinoma: A Systematic Review. *Cardiovasc Intervent Radiol*. 2017;40(7):1033-1043. doi:10.1007/s00270-017-1594-4

161. Pasciak AS, Abiola G, Liddell RP, et al. The number of microspheres in Y90 radioembolization directly affects normal tissue radiation exposure. *Eur J Nucl Med Mol Imaging*. 2020;47(4):816-827. doi:10.1007/s00259-019-04588-x

162. Jacobsen MC, Cressman ENK, Tamm EP, et al. Dual-energy CT: Lower limits of iodine detection and quantification. *Radiology*. 2019;292(2):414-419. doi:10.1148/radiol.2019182870

163. Khazaee Moghadam M, Kamali Asl A, Geramifar P, Zaidi H. Evaluating the application of tissue-specific dose kernels instead of water dose kernels in internal dosimetry: A monte carlo study. *Cancer Biother Radiopharm*. 2016;31(10):367-379. doi:10.1089/cbr.2016.2117

164. Mikell JK, Mahvash A, Siman W, Mourtada F, Kappadath SC. Comparing voxel-based absorbed dosimetry methods in tumors, liver, lung, and at the liver-lung interface for 90Y microsphere selective internal radiation therapy. *EJNMMI Phys*. 2015. doi:10.1186/s40658-015-0119-y

165. Bolch WE, Bouchet LG, Robertson JS, et al. MIRD pamphlet no. 17: The dosimetry of nonuniform activity distributions - Radionuclide S values at the voxel level. *J Nucl Med*. 1999;40(1).

166. Pasciak AS, Erwin WD. Effect of voxel size and computation method on Tc-99m MAA SPECT/CT-based dose estimation for Y-90 microsphere therapy. *IEEE Trans Med Imaging*. 2009. doi:10.1109/TMI.2009.2022753

167. Bastiaannet R, Kappadath SC, Kunnen B, Braat AJAT, Lam MGEH, de Jong HWAM. The physics of radioembolization. *EJNMMI Phys*. 2018;5(1). doi:10.1186/s40658-018-0221-z

168. Yue J, Mauxion T, Reyes DK, et al. Comparison of quantitative Y-90 SPECT and non-time-of-flight PET imaging in post-therapy radioembolization of liver cancer. *Med Phys*. 2016;43(10):5779-5790. doi:10.1118/1.4962472

169. Elschot M, Vermolen BJ, Lam MGEH, de Keizer B, van den Bosch MAAJ, de Jong HWAM. Quantitative Comparison of PET and Bremsstrahlung SPECT for Imaging the In Vivo Yttrium-90 Microsphere Distribution after Liver Radioembolization. *PLoS One*. 2013;8(2):e55742. doi:10.1371/journal.pone.0055742

170. Tapp KN, Lea WB, Johnson MS, Tann M, Fletcher JW, Hutchins GD. The impact of image reconstruction bias on PET/CT 90Y dosimetry after radioembolization. *J Nucl Med*. 2014;55(9):1452-1458. doi:10.2967/jnumed.113.133629 [doi]

171. Rong X, Frey EC. A collimator optimization method for quantitative imaging: Application to Y-90 bremsstrahlung SPECT. *Med Phys*. 2013;40(8). doi:10.1118/1.4813297

172. Chan KT, Alessio AM, Johnson GE, et al. Prospective Trial Using Internal Pair-Production Positron Emission Tomography to Establish the Yttrium-90 Radioembolization Dose Required for Response of Hepatocellular Carcinoma. *Int J Radiat Oncol Biol Phys*. 2018;101(2):358-365. doi:10.1016/j.ijrobp.2018.01.116

173. Fowler KJ, Maughan NM, Laforest R, et al. PET/MRI of Hepatic 90Y Microsphere Deposition Determines Individual Tumor Response. *Cardiovasc Intervent Radiol*. 2016;39(6):855-864. doi:10.1007/s00270-015-1285-y

174. Moreno-Luna LE, Yang JD, Sanchez W, et al. Efficacy and safety of transarterial radioembolization versus chemoembolization in patients with hepatocellular carcinoma. *Cardiovasc Intervent Radiol*. 2013;36(3):714-723.

175. Ae JIB, De A, Ae M, et al. Biocompatibility, Inflammatory Response, and Recannalization Characteristics of Nonradioactive Resin Microspheres: Histological Findings. doi:10.1007/s00270-009-9592-9

176. Gulec SA, Sztejnberg ML, Siegel JA, Jevremovic T, Stabin M. Hepatic Structural Dosimetry in 90 Y Microsphere Treatment: A Monte Carlo Modeling Approach Based on Lobular Microanatomy. *J Nucl Med*. 2010;51:301-310. doi:10.2967/jnumed.109.069278

177. Cremonesi M, Chiesa C, Strigari L, et al. Radioembolization of hepatic lesions from a radiobiology and dosimetric perspective. *Front Oncol*. 2014;4:210. doi:10.3389/fonc.2014.00210 [doi]

178. Henry EC, Strugari M, Mawko G, et al. Post-administration dosimetry in yttrium-90 radioembolization through micro-CT imaging of radiopaque microspheres in a porcine renal model. *Phys Med Biol*. 2021;66(9):095011. doi:10.1088/1361-6560/abf38a

179. Chen J, White SB, Harris KR, et al. Poly(lactide-co-glycolide) Microspheres for MRI-Monitored Delivery of Sorafenib in a Rabbit VX2 model HHS Public Access. *Biomaterials*. 2015;61:299-306. doi:10.1016/j.biomaterials.2015.05.010

180. Högberg J, Rizell M, Hultborn R, et al. Heterogeneity of microsphere distribution in resected liver and tumour tissue following selective intrahepatic radiotherapy. *EJNMMI Res*. 2014;4(1):48.

181. *Evaluation of Detection Capability for Clinical Laboratory Measurement Procedures; Approved Guideline-Second Edition*.; 2012.

182. Carlier T, Eugène T, Bodet-Milin C, et al. Assessment of acquisition protocols for routine imaging of Y-90 using PET/CT. *EJNMMI Res*. 2013. doi:10.1186/2191-219X-3-11

183. Alsultan AA, Braat AJAT, Smits MLJ, et al. Current Status and Future Direction of Hepatic Radioembolisation. *Clin Oncol*. 2021;33(2):106-116. doi:10.1016/j.clon.2020.12.003

184. Conti M, Eriksson L, Rothfuss H, et al. Characterization of 176Lu background in LSO-based PET scanners. *Phys Med Biol*. 2017;62(9):3700-3711. doi:10.1088/1361-6560/aa68ca

185. Vogel W V, Van Dalen JA, Wiering B, et al. Evaluation of Image Registration in PET/CT of the Liver and Recommendations for Optimized Imaging. *J Nucl Med*. 2007;48:910-919. doi:10.2967/jnumed.107.041517

186. Debbaut C, Segers P, Cornillie P, et al. Analyzing the human liver vascular architecture by combining vascular corrosion casting and micro-CT scanning: A feasibility study. *J Anat*. 2014. doi:10.1111/joa.12156

187. McCollough CH, Leng S, Yu L, Fletcher JG. Dual- and multi-energy CT: Principles, technical approaches, and clinical applications. *Radiology*. 2015;276(3):637-653. doi:10.1148/radiol.2015142631

188. Church C, Mawko G, Archambault JP, et al. Absorbed dose kernel and self-shielding calculations for a novel radiopaque glass microsphere for transarterial

radioembolization. *Med Phys*. 2018;45(2):934-942. doi:10.1002/mp.12717 [doi]

189. Cho SH, Reece WD, Kim C-HH. Validity of two simple rescaling methods for electron/beta dose point kernels in heterogeneous source–target geometry. *Radiat Phys Chem*. 2004;69(4):265-272. doi:10.1016/S0969-806X(03)00475-4

190. Götz T, Schmidkonz C, Lang EW, Maier A, Kuwert T, Ritt P. A comparison of methods for adapting 177Lu dose-voxel-kernels to tissue inhomogeneities. *Phys Med Biol*. 2019;64(24):245011. doi:10.1088/1361-6560/ab5b81

191. Tiwari A, Gravesa SA, Sunderland J. The Impact of Tissue Type and Density on Dose Point Kernels for Patient-Specific Voxel-Wise Dosimetry: A Monte Carlo Investigation. *Radiat Res*. 2020;193(6):531-542. doi:10.1667/RR15563.1

Appendix A – Copywrite Permission

Manuscripts 1 and 2 were published through *IOP Publishing*. The copywrite agreement allows for the "Author's Original" manuscript to be published in this thesis document. For additional information, see:

https://publishingsupport.iopscience.iop.org/author-rights-policies/

Manuscript 3 was published through *Springer* under a copywrite agreement that allows the authors to share and/or adapt the material in any medium or format, and therefore explicit permission to include this manuscript was not required. For additional information, see:

https://www.springeropen.com/get-published/copyright/copyright-and-license-agreement

Appendix B – List of Variables

Variable names introduced in Chapters 3 through 6 are provided below with units and descriptions. Variables are listed in order of appearance. If the variable was introduced in multiple chapters, it is only described in the chapter where it was first introduced.

Chapter 3

LOB_{HU}	The highest apparent signal expected to be found when replicates of the control agarose phantom are repeatedly measured [HU]
LOD_{HU}	The concentration of microspheres in agarose that leads to the conclusion that the microsphere concentration is greater than that of the agarose control phantom [HU]
σ_{low}	Standard deviation of CT voxel values in the agarose phantom containing 5.5 mg of microspheres [HU]
μ_{agar}	Average value of repeated measurements of the agarose control phantom [HU]
σ_{agar}	Standard deviation of repeated measurements of the agarose control phantom [HU]
$LOD_{MS/vox}$	The concentration of microspheres in agarose that leads to the conclusion that the microsphere concentration is greater than that of the agarose control phantom [MS/voxel]
$LOD_{MS/mL}$	The concentration of microspheres in agarose that leads to the conclusion that the microsphere concentration is greater than that of the agarose control phantom [MS/mL]

Chapter 4

WB	External, whole-body contour of pig kidney [Contour]
NT	A 1 cm-dimeter spherical volume located in a non-embolized, homogeneous background region of the pig kidney [Contour]
T	A 2 cm-dimeter spherical volume placed at the centroid of the pig kidney [Contour]
$A_{0.18}$	Simulated ^{90}Y activity distribution within the pig kidney with an isotropic voxel size of 0.18 mm [Bq]
$A_{2.50}$	Interpolated ^{90}Y activity distribution within the pig kidney with an isotropic voxel size of 2.50 mm [Bq]

$A_{5.00}$	Interpolated ^{90}Y activity distribution within the pig kidney with an isotropic voxel size of 5.00 mm [Bq]
$A_{7.50}$	Interpolated ^{90}Y activity distribution within the pig kidney with an isotropic voxel size of 7.50 mm [Bq]
$A_{10.00}$	Interpolated ^{90}Y activity distribution within the pig kidney with an isotropic voxel size of 10.00 mm [Bq]
$A_{12.50}$	Interpolated ^{90}Y activity distribution within the pig kidney with an isotropic voxel size of 12.50 mm [Bq]
$A_{15.00}$	Interpolated ^{90}Y activity distribution within the pig kidney with an isotropic voxel size of 15.00 mm [Bq]
$DVK_{0.18}$	^{90}Y dose-voxel kernel with an isotropic voxel size of 0.18 mm [Gy/History]
$DVK_{2.50}$	^{90}Y dose-voxel kernel with an isotropic voxel size of 2.50 mm [Gy/History]
$DVK_{5.00}$	^{90}Y dose-voxel kernel with an isotropic voxel size of 5.00 mm [Gy/History]
$DVK_{7.50}$	^{90}Y dose-voxel kernel with an isotropic voxel size of 7.50 mm [Gy/History]
$DVK_{10.00}$	^{90}Y dose-voxel kernel with an isotropic voxel size of 10.00 mm [Gy/History]
$DVK_{12.50}$	^{90}Y dose-voxel kernel with an isotropic voxel size of 12.50 mm [Gy/History]
$DVK_{15.00}$	^{90}Y dose-voxel kernel with an isotropic voxel size of 15.00 mm [Gy/History]
σ_{dose}	Dosimetric uncertainty in a dose-voxel kernel [%]
N	Number of cardinal axis
r	Radial distance from the origin of a dose-voxel kernel along each cardinal axis [Voxels]
D_i	Absorbed dose to a voxel in a dose-voxel kernel [Gy]
i	Dose-voxel kernel voxel index
$\overline{D}$	Average dose across voxels in dose-voxel kernel from all cardinal axes [Gy]
σ_{stat}	Relative statistical uncertainty in a dose-voxel kernel [%]
d_i	Energy deposited in a voxel in a dose-voxel kernel [J]
n	Number of interactions within a voxel in a dose-voxel kernel [#]
dd_{MC}	^{90}Y dose distribution determined from a Monte Carlo simulation of radiation transport in the pig kidney [Gy]

$dd_{0.18}$	^{90}Y dose distribution with an isotropic voxel size of 0.18 mm determined through convolution [Gy]
$dd_{2.50}$	^{90}Y dose distribution with an isotropic voxel size of 2.50 mm determined through convolution [Gy]
$dd_{5.00}$	^{90}Y dose distribution with an isotropic voxel size of 5.00 mm determined through convolution [Gy]
$dd_{7.50}$	^{90}Y dose distribution with an isotropic voxel size of 7.50 mm determined through convolution [Gy]
$dd_{10.00}$	^{90}Y dose distribution with an isotropic voxel size of 10.00 mm determined through convolution [Gy]
$dd_{12.50}$	^{90}Y dose distribution with an isotropic voxel size of 12.50 mm determined through convolution [Gy]
$dd_{15.00}$	^{90}Y dose distribution with an isotropic voxel size of 15.00 mm determined through convolution [Gy]
D_{μ}	Average dose to the kidney volume [Gy]
σ	Standard deviation of dose values in the kidney volume [Gy]
D_{min}	Minimum dose to the kidney volume [Gy]
D_{max}	Maximum dose to the kidney volume [Gy]
D_{med}	Median dose to the kidney volume [Gy]
D_{70}	Minimum dose received by at least 70% of the entire kidney volume [Gy]
D_1	Minimum dose received by at least 1% of the entire kidney volume [Gy]
D_{MIRD}	Average dose determined through the Medical Internal Radiation Dose formalism [Gy]
M	Mass of target in the Medical Internal Radiation Dose formalism [kg]
A_0	Administered ^{90}Y activity in the Medical Internal Radiation Dose formalism [GBq]

Chapter 5

A_{MS}	Microsphere specific activity [Bq/MS]
MS_{con}	Microsphere concentration [MS/mL]
m_{cal}	Calibration curve slope [HU/MS/mg]
b_{cal}	Calibration curve intercept [HU]

μ_{bkg}	Average value of CT voxels in a non-embolized, homogeneous background region of the liver [HU]
σ_{bkg}	Standard deviation of CT voxel values in a non-embolized, homogeneous background region of the liver [HU]
L_{bkg}	A non-embolized, homogeneous background region of a rabbit liver [Contour]
A_{CT}	^{90}Y activity distribution determined from CT imaging [Bq]
MS_{mg}	Number of microspheres contained within one milligram [MS/mg]
V_{CT}	CT voxel volume [mL]
A_0	^{90}Y activity administered to a rabbit [Bq]
RC_{CT}	CT recovery coefficient for the microsphere mass within the liver [%]
A_{PET}	^{90}Y activity distribution determined from PET imaging [Bq]
L	Rabbit liver [Contour]
L_{shell}	The rabbit liver contour plus a 1 cm isotropic margin [Contour]
RC_{PET}	PET recovery coefficient for the microsphere mass within the liver [%]
RC_{PET}^{shell}	PET recovery coefficient for the microsphere mass within the liver [%]
B	An external, whole-body rabbit contour [Contour]
R	Residual activity following microsphere administration [MBq]
DD_{PET}	Dose distribution in a rabbit determined from PET imaging [Gy]
DD_{CT}	Dose distribution in a rabbit determined from CT imaging [Gy]
DVK_{PET}	^{90}Y dose-voxel kernel with dimensions equal to a PET voxel [Gy/History]
DVK_{CT}	^{90}Y dose-voxel kernel with dimensions equal to a CT voxel [Gy/History]
μ_{bkg_phant}	Average value of CT voxels in the background region of the calibration phantom [HU]
σ_{bkg_phant}	Standard deviation of CT voxel values in the background region of the calibration phantom [HU]
$\sigma_{0.5}$	standard deviation of CT voxel values in the calibration post containing a microsphere concentration of 0.5 mg/mL of microspheres [HU]
$LOD_{mg/mL}$	The concentration of microspheres in the calibration phantom that leads to the conclusion that the microsphere concentration is greater than that of the background [mg/mL]

MDA_{CT} Minimum detectable ^{90}Y activity concentration determined from CT imaging [MBq/mL]

MDA_{PET} Minimum detectable ^{90}Y activity concentration determined from PET imaging [MBq/mL]

Chapter 6

TRE Target registration error for co-registration of CT images of the clinical calibration phantom [mm]

$d_{P,i}$ Spatial location for the co-registration points in the primary image [mm]

$d_{S,i}$ Spatial location for the co-registration points in the secondary image [mm]